Characterization of Single Emitters and Nano-Antennas

Cover: the title is composed of confocal fluorescence images of nitrogen-vacancy (NV) centers in 120 nm nanodiamonds. Individual characters are milled into a silver film as 80 nm grooves using focused-ion-beam (FIB). Nanodiamonds are subsequently dispersed on top of the silver mask and the fluorescence is collected through the glass substrate using a scanning confocal microscope. The height of the characters is about 4 μm.

Ph.D. thesis University of Amsterdam, February 2015
Characterization of Single Emitters and Nano-Antennas
Abbas Mohtashami

ISBN 978-90-77209-87-5

A digital version of this thesis can be downloaded from http://www.amolf.nl.

CHARACTERIZATION OF SINGLE EMITTERS AND NANO-ANTENNAS

ACADEMISCH PROEFSCHRIFT

ter verkrijging van de graad van doctor
aan de Universiteit van Amsterdam
op gezag van de Rector Magnificus
prof. dr. D. C. van den Boom
ten overstaan van een door het College voor Promoties ingestelde
commissie, in het openbaar te verdedigen in de Agnietenkapel
op donderdag 5 februari 2015, te 10:00 uur

door

Abbas Mohtashami

geboren te Arak, Iran

Promotiecommissie:

Promotor:	prof. dr. A. F. Koenderink	Universiteit van Amsterdam
Overige leden:	prof. dr. J.-J. Greffet	Université Paris-Sud, Frankrijk
	prof. dr. J. Gómez-Rivas	Technische Universiteit Eindhoven
	prof. dr. D. Bonn	Universiteit van Amsterdam
	prof. dr. A. M. Brouwer	Universiteit van Amsterdam
	prof. dr. T. Gregorkiewicz	Universiteit van Amsterdam

Faculteit der Natuurwetenschappen, Wiskunde en Informatica

The work described in this thesis is part of the research program of the
"Stichting voor Fundamenteel Onderzoek der Materie (FOM)"
which is financially supported by the
"Nederlandse Organisatie voor Wetenschappelijk Onderzoek (NWO)".

This work was carried out at the
Center for Nanophotonics,
FOM Institute for Atomic and Molecular Physics AMOLF,
Science Park 104, 1098 XG Amsterdam, The Netherlands,
where a limited number of copies of this dissertation is available.

Contents

1

Introduction

This thesis presents scientific research into the question *how can you manipulate the emission of light*. There is no doubt that throughout the ages controlling the emission of light has enabled great advances in science and society. The Nobel Prizes in Physics and Chemistry 2014 alone are sufficient to underline this point [1, 2]. The Nobel Prize in Physics 2014 was awarded to Nakamura, Akasaki, and Amano for the invention of the blue LED, which enables a huge savings in energy in lighting our world compared to the traditional incandescent light bulb, as well as enabling many devices such as displays for mobile phones, tablets and computers, that revolutionize the way our society operates in terms of communication and sharing of information. The Nobel Prize in Chemistry 2014 on the other hand, highlights the relevance of harnessing emission for science, as it recognized Moerner, Hell and Betzig for groundbreaking techniques in superresolved fluorescence microscopy that hinge on collecting light emitted by single molecules, and controlling how those molecules emit. Indeed, collecting the fluorescence of (single) molecules is now a key technique to understand the physics and chemistry of many physical and biophysical systems. The color of emission, the rate of emission, and the timescales on which emission properties fluctuate can all be used as fingerprints characterizing either the emitter or its environment in terms of energy levels, conformation, or fluctuations therein.

The research in this thesis is part of worldwide efforts to harness the emission of the ultimate smallest light sources. The ultimate smallest light source is a quantum mechanical system, such as an atom, molecule, or quantum dot [3]. In such a system spontaneous emission of light can occur when the system is somehow prepared in its excited state, and then spontaneously, and irreversibly relaxes to an energetically lower state (or ground state in a simple two-level scheme) upon the emission of a photon [4–6]. The emission of single quantum emitters in the solid state was first

observed by Moerner et al. [7] and by Orrit et al. [8] around 1989. Nowadays, with the advent of silicon photodetectors with near-unity quantum efficiency for detecting a photon, observing single molecule emission is a routine affair in any microscopy lab [3]. Yet, there are several important reasons why improving our control over the emission properties of single emitters is an important goal for many researchers in physics. First, when using the fluorescence of an emitter inside a system as a reporter for the state of the system, the rate at which information can be collected about the system is directly limited by the photon detection rate. For instance, suppose that one desires to measure the position of a protein in a physiological environment by tracing the motion of an attached fluorescent group on a CCD camera, or that one desires to monitor conformational changes in a polymer by measuring changes in emission spectrum of an embedded fluorophore. In both cases, a certain number of detected photons in an image is required to accurately fit the molecular position, and a minimum number of detected counts in a spectrum is required to fit its peak with a certain accuracy. That minimum number is directly given by the shot noise inherent in signals of low photon-number [9]. Thus any strategy to increase the number of photons directed onto the detector will improve the sampling rate of a fluorescence probe as reporter of a system.

Another important reason to harness the emission of single emitters lies in the fact that single photon sources are projected to enable secure communication, and quantum information processing [10]. While classical communication channels can be eavesdropped, communication via a quantum mechanical resource can be secure [10]. In particular, secure communication protocols have been proposed and demonstrated that require sources that provide single photons on demand, or in other protocols, photon pairs. While in the implementations closest to commercialization [11] spontaneous parametric down conversion of laser pulses in nonlinear crystals is used to create photon pairs [10], single quantum systems are still widely pursued for single photon sources. In principle a single quantum emitter would be an ideal single photon source, in the sense that it can only contain a single electronic excitation at a time, thereby guaranteeing that at most a single photon comes out after an excitation event [3]. If one could collect each single photon for each excitation event, one would truly obtain single-photons on demand. Even more far reaching demands are placed by the field of *quantum information processing* and *quantum simulation* [12, 13]. In these fields it is proposed that particular algorithms that are exponentially difficult for classical computers, could be performed by operating on quantum mechanical states or 'qubits'. One route to realizing this objective could be to connect localized quantum systems to each other by letting them exchange photons, as described by Kimble [14]. As in the case of improving emitters for microscopy, a minimal (and insufficient) prerequisite is that one can completely control how fast, and whereto a single emitter emits its single photon. Quantum information applications, however, place more stringent demands, for instance requiring subsequent photons to be indistinguishable, and/or requiring 'quantum strong coupling', i.e., reversible interaction between photon and emitter [15].

As a third motivation besides using single molecules as reporter, and besides using single emitters as single photon sources, we note that understanding how to

improve the ultimate smallest source can improve our understanding of how to improve macroscopic sources, such as LEDs, or sources integrated on chips for classical information processing. For instance, while Nakamura, Akasaki, and Amano have shown how to realize efficient blue LEDs [16], a problem of large current industrial interest is how to convert blue LED light into white light with the least use of fluorescent or phosphorescent conversion material [17].

Given that controlling the emission of single emitters is an important goal, the question is why it is actually a challenge, what can actually be improved, and what known strategies are. In a typical fluorescence microscopy experiment, one uses a laser focused to a diffraction limited spot ($\lambda/2$ in size) with a photon energy higher than that of the fluorescence to be generated to excite the molecule [5, 6]. Given the small excitation cross section of molecules, the typical excitation efficiency is around 10^{-5}. Next, the questions is how often an excitation cycle can be repeated on a given molecule per unit time, since this limits the ultimate photon flux. This timescale is set by the fluorescent lifetime, typically on order of tens of nanoseconds for quantum dots, and molecules, leading to theoretical maximum photon rates up to 10^8/s. Finally, not each excitation cycle may actually lead to a photon. On one hand, an emitter may suffer internal loss due to competing decay mechanisms, while on the other hand the fact that a single quantum emitter is essentially a point compared to the optical wavelength (1 nm size, versus 500 nm wavelength) means that emission is almost isotropically into all directions, resulting in poor collection efficiencies even with a high NA lens. Emission control hence revolves around (1) increasing excitation efficiency, (2) enhancing fluorescence decay rates, (3) limiting internal loss, i.e., improving emission quantum efficiency, and (4) improving light collection by either enhancing the NA of the collection optics, or redirecting emission.

1.1 Spontaneous emission and LDOS

Let us assume a single quantum mechanical system that we describe as a two-level system, which is a good approximation to the typical Jabłońksi diagram [6] of a fluorophore as sketched in figure 1.1 (a). We denote the transition energy as $\hbar\omega$ and the ground state and excited state wave function as $|g\rangle$ and $|e\rangle$. In a quantum mechanical system, spontaneous emission of light happens when the system in its excited state, spontaneously relaxes to an energetically lower state (or ground state in a simple two-level scheme) with the emission of a photon. The relaxation of the quantum mechanical system into the ground state is a stochastic process, and therefore, its timing can be only described statistically. The probability per unit time that the system relaxes into the ground state is called the decay rate γ. Fermi's Golden Rule [18] states that the rate at which an emitter decays upon emission of a photon results from summing over all possible energy-conserving transitions from the initial state $|i\rangle$ (excited state atom, no photon $|e,0\rangle$) to the final state $|f\rangle$ (ground state atom, one photon $|g,1\rangle$):

$$\gamma = \frac{2\pi}{\hbar}\sum_f |\langle f|\hat{H}|i\rangle|^2 \delta(E_i - E_f), \tag{1.1}$$

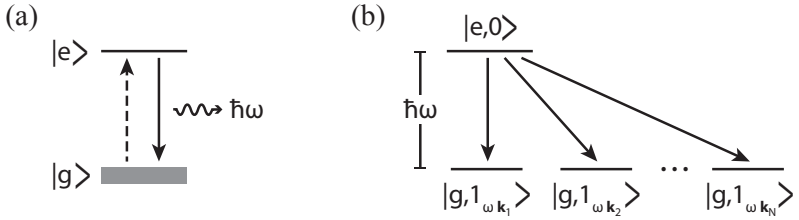

Figure 1.1: (a) Jabłoński diagram of a fluorophore abstracted as a two-level emitter (ground state $|g\rangle$, excited state $|e\rangle$) with energy levels separated by the photon energy $\hbar\omega$ (b) Accounting for all the possible final states for the spontaneous emission process, it is important to account for the fact that the final states is the combination of a ground state atom *plus* a single photon in some photonic mode.

where $\hat{H} = -\hat{\boldsymbol{\mu}} \cdot \hat{\boldsymbol{E}}$ is the interaction Hamiltonian which describes the electric dipole interaction. As illustrated in figure 1.1 (b), the final state involves different modes of the radiation field ($\boldsymbol{k}_i$) (all with the same transition frequency ω) to which the system can decay [5]. The decay rate is therefore, determined by the total number of available states as specified by the summation in equation 1.1. For a continuum set of final states, the equation 1.1 can be written as

$$\gamma = \frac{\pi\omega}{3\hbar\epsilon_0}|\boldsymbol{\mu}|^2\rho(\omega,\boldsymbol{r}), \tag{1.2}$$

where $\boldsymbol{\mu} = \langle g|\hat{\boldsymbol{\mu}}|e\rangle$ is the transition-dipole matrix element, and $\rho(\omega,\boldsymbol{r})$ is the local density of optical states (LDOS) which involves all available photon states at frequency ω [19]. From equation 1.2, we can separate the decay rate of a quantum emitter in two parts. First, the electronic energy scheme appears through the photon energy, by virtue of the fact that energy must be conserved in the transition. Moreover, the wave functions of the emitter itself appear through the transition-dipole matrix element $\boldsymbol{\mu}$. Thus the wave function overlap, or more precisely the matrix element with the dipole operator $\hat{\boldsymbol{\mu}} = q\mathbf{r}$, directly determine how fast spontaneous emission occurs. This element moreover may contain spin and orbital angular momentum rules, as is well known for atomic transitions. The second term that appears quantifies the property of the photonic environment into which the photon is emitted through the local density of optical states $\rho(\omega,\boldsymbol{r})$, which describes the number of available modes at the position of the source ($\boldsymbol{r}$) to which the system can decay. In this work we are not concerned with modifying spontaneous emission through modifying the emitter wave functions, but rather solely concentrate on modifying emission through changing the photonic environment. Modifying the photonic environment of an emitter such that it provides a high LDOS at the position of the source, results in an enhancement in the spontaneous emission of the emitter [19].

That it is possible to modify emission probabilities without modifying the emitter wave functions is a notion often ascribed to a very brief and cryptic conference abstract

by E. M. Purcell that appeared in Physical Review in 1946 [20]. However, it was first convincingly shown in seminal experiments in the late 1960's by Drexhage. Drexhage showed that the decay rate of a fluorescent molecule can be modified by placing it in the near-field of a mirror [21]. Depending on the distance between the molecule and the mirror, the decay rate can be enhanced or suppressed. He explained the effect via constructive or destructive interference between the emitted light and the reflected light from the mirror. The effect can also be explained through the "local density of optical states" terminology introduced by Sprik et al. [19], i.e., through enumerating all photonic modes of the system explicitly [22, 23].

The fact that the LDOS of a nanoscale structure is a key parameter to determine how strongly the structure affects emission is of importance for this thesis in two distinct ways. First, from the perspective of engineering spontaneous emission improvements, it is clear that taking an emitter of exactly known properties, LDOS will precisely describe the acceleration of its dynamics in the photonic system. Conversely, if one wants to select an emitter as starting point for creating a single photon source, the concept of LDOS provides a handle on how to characterize the suitability of the emitter. Generally a fluorophore is subject not just to radiative decay, but also nonradiative decay where the electronic excitation is for instance lost as phonons or molecular vibrations, and not as a radiated photon. A fluorescence intensity decay rate measurement simply measures the summed radiative and nonradiative contributions to the decay rate, making it impossible to back out the ratio between the two from a single measurement. Since the LDOS only influences the radiative decay rate, the total decay rate γ_{tot} for a fluorophore in a photonic system is given by

$$\gamma_{\mathrm{tot}} = \gamma_{\mathrm{nr}} + \gamma_{\mathrm{r}}\,\rho(\omega, \boldsymbol{r}) \tag{1.3}$$

where γ_{nr} and γ_{r} are nonradiative and radiative decay rates for the emitter in vacuum, and ρ is the LDOS at the position of the source, normalized to the LDOS in vacuum. Using a Drexhage type of experiment in which known LDOS variations are applied, one can differentiate the radiative and non-radiate part of the decay rate, from which the quantum efficiency (QE)

$$QE = \frac{\gamma_{\mathrm{r}}}{\gamma_{\mathrm{r}} + \gamma_{\mathrm{nr}}} \tag{1.4}$$

of the emitter can be extracted. Besides the original work of Drexhage in this spirit, variations of this method have been applied to ensembles of dyes, quantum dots, and rare earth ions [24–28], and even to a single molecule by Buchler et al [29].

Finally, we note that while here we have considered the rate of emission, photonic environments can also affect the distribution of emission over, e.g., far field angle. In a photonic system, the local density of states may be dominated by just a few terms, as is for instance the case when building a single mode resonant cavity around an emitter, or when placing an emitter in the near field of a strongly confined guided mode. Since the relative ratio at which emitted photons populate the available modes is directly given by their relative contribution to the summed local mode density at their position, redirecting emission is tantamount to engineering which modes dominate the LDOS.

1.2 Structures that control spontaneous emission

In this section we briefly discuss reported strategies to control the local density of optical states.

Microcavities:

It is useful to first estimate the number of states that vacuum offers, as is explained in the textbook by Loudon [18]. If one takes a volume (for instance, a cubic meter) of vacuum surrounded by perfectly conducting walls, one can simply enumerate the number of standing waves that fit inside the volume, and calculate their frequency. By counting how many states fit in a given frequency interval ω to $\omega + d\omega$, one finds that vacuum at visible wavelengths offers about 10^5 photon states per m^3, per Hz of spectral bandwidth $d\omega$. Suppose now that you create an optical cavity, for instance by confining a mode between two mirrors. Let us suppose that this optical resonator is placed exactly around the emitter, and that it supports just one photon mode confined to about 1 μm in all directions, and a quality factor Q=10^5 (0.1 THz bandwidth). Directly comparing Q/V (1 state per μm^3 and in a bandwidth $d\omega$ of 0.1 THz) to vacuum DOS (10^5 per m^3, per Hz) shows that this cavity will locally provide an extra contribution to Fermi's Golden Rule, exceeding the vacuum DOS. The exact ratio

$$F = \frac{3}{4\pi^2}\frac{Q}{V}\lambda^3 \tag{1.5}$$

is known as Purcell factor for local density of optical states (LDOS) enhancement, and was first proposed by Purcell in 1946 [20]. A cavity will accelerate emission of emitters by a factor F and redistribute the usually omnidirectional emission into the cavity with efficiency $F/(1+F)$. Obtaining high Purcell factors has thereby been a key objective for the field of quantum optics, since it simultaneously reduces the timing uncertainty between excitation and photon emission that is important for 'triggered single photon sources' and helps to decouple an emitter from the entire continuum of modes besides the cavity mode. Furthermore, the regime of quantum strong coupling typically requires as first step to reach a sufficiently high Purcell factor [15].

High Purcell factors require high quality factor cavities with small mode volumes [30]. High quality factors directly lead to the demand to use virtually lossless optical materials, i.e., dielectrics such as glass, or semiconductor materials. Cavities with very high quality factors have been realized using whispering gallery modes in ring-resonators, microspheres and microtoroid cavities [30–32]. Such cavities have $Q = 10^6 - 10^9$, with mode volumes of tens of microns across. High Purcell factors at lower Qs require optimization of cavities at the fundamental limit for the tightest confinement of light in dielectrics, i.e., $V = (\lambda/2n)^3$ in each dimension. Semiconductor microdisk, micropillar and so-called photonic crystal cavities at this limit, and with quality factors of 10^5 have indeed been shown to give sizeable Purcell enhancements [33–36] with reported measured values up to 5 to 10 times [37]. Moreover, due to high Purcell enhancement, strong light-matter interaction down to single photon level

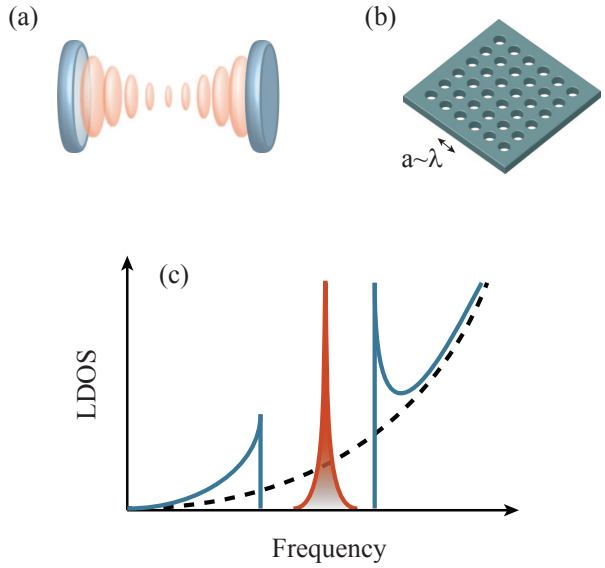

Figure 1.2: (a) Cartoon of a photonic microcavity that fits a standing optical wave (b) Sketch of a photonic crystal, with periodicity a comparable to the optical wavelength λ (c) The local density of states in vacuum is quadratic in frequency (dashed line), amounting to about 10^5 states per second, per cubic meter of vacuum at visible frequencies. A cavity adds one mode in a bandwidth Q and in a volume V equal to the cavity mode volume (red curve). A 3D periodic photonic crystal can provide a photonic band gap, i.e., an interval of zero LDOS, surrounded by enhanced LDOS at the band edges (blue curve).

can be achieved in photonic cavities which makes them suitable for quantum optics applications [34, 37]. This is deemed a very exciting platform for quantum information processing, owing to the integration with III-V emitters with excellent properties. However, since this is a narrowband platform (high Q) operating at 1-2 K temperatures, its utility for other applications is limited.

Photonic crystals

Photonic crystals are periodic dielectric structures with periodicity on order of the wavelength. Due to interference from the periodic lattice, photonic crystals can form band gaps for light in a defined range of frequencies, corresponding to the Bragg conditions of the lattice [38]. The simplest form of the photonic crystals are multilayer periodic dielectric stacks known as Bragg mirrors [39]. The term *photonic crystal* was introduced for the first time for higher dimensional structures in 1987 by Yablonovitch and John who proposed using photonic crystals for controlling the spontaneous emission of light by virtue of a so-called 'photonic band gap', a

frequency window in which the local density of optical states is identically zero [40, 41]. Formation of photonic band gaps due to interference is in close analogy to the formation of electronic band gaps in ionic lattices, however with the distinction that the limited range of dielectric constants available to build photonic crystals from is limited, effectively limiting the depth of the periodic potential for light that can be reached. Together with the vectorial nature of the wave equation for light, it turns out that full photonic band gaps are difficult to reach in practice [38]. Busch and John evaluated the LDOS in photonic crystals for the first time [42]. The photonic band gap means that the decay rate of an emitter placed within a photonic crystal structure whose emission frequency falls within the bandgap of the photonic crystal, can be completely suppressed. Conversely, at the band edges enhancement is expected owing to van Hove singularities in the local density of states. In practice, Kaniber et al and Wang et al. showed suppression of the spontaneous emission in 2D photonic crystals made in GaAs and probed by quantum dots by a factor of 5 to 10 [43, 44]. As regards 3D photonic crystals, the largest suppressions of emission were reported by Lodahl et al. [45] in an inverse opal without full band gap, and by Leistikow et al. [46] in a crystal with full photonic band gap. The primary current use of photonic crystals is as platform to embed high Purcell-factor cavities in.

Plasmonic structures

The third strategy to control spontaneous emission that has emerged is through so-called 'plasmons', or 'surface plasmon polaritons' [48]. Surface plasmon polaritons (SPPs) are evanescent electromagnetic waves that are strongly coupled to the collective oscillations of the free electrons at the interface between a metal and a dielectric (See figure 1.3(a)). On a planar metal interface, SPPs are in the form of transverse magnetic (TM) waves that propagate along the interface and rapidly decay perpendicular to the interface, i.e., both into the metal and into the vacuum [49]. This rapid decay results in a strong confinement of SPPs at the interface, with decay lengths into dielectric of the order of 100 nm in the visible. The dispersion relation of the propagating SPPs along the interface is given by the Maxwell's equation as

$$k_{SPP} = k_0 \sqrt{\frac{\varepsilon_d \varepsilon_m}{\varepsilon_d + \varepsilon_m}}, \tag{1.6}$$

where ε_d and ε_m are the frequency (ω) dependent permittivity of the dielectric and the metal, and k_0 is the free-space wavevector. The frequency dependence of the metal permittivity is often expressed using the Drude model for a free electron gas as

$$\varepsilon_m^{Drude} = 1 - \frac{\omega_p^2}{\omega^2 + i\Gamma\omega} \tag{1.7}$$

where ω_p is the plasma frequency of the electron gas and Γ is the damping rate due to losses inherent to the metals [50]. At visible frequencies, the dielectric constant of metals approaches minus one, resulting in a strongly confined mode with in-plane wavenumber well beyond the free-space wavenumber. The complex nature of the

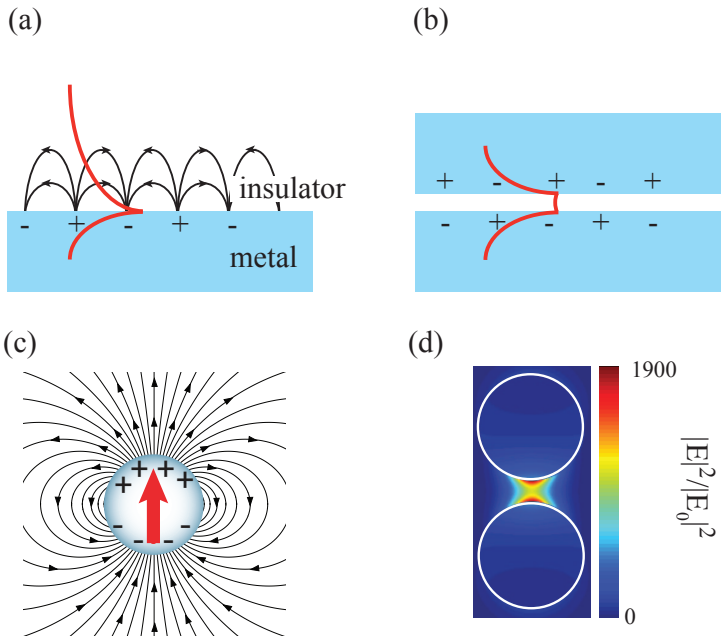

Figure 1.3: (a) A metal-dielectric interface can support a 'surface plasmon polariton': a surface charge density oscillation accompanied by a transverse magnetic field, as well as a strong electric field with a component perpendicular to the interface, and a component along both interface and the wave vector of the mode. (b) A metal-insulator-metal system, i.e., a gap between two metal plates of order a few tens of nanometers filled with air, or a dielectric, can support a surface plasmon polariton very strongly localized in the gap, formed by coupling of the two single-interface surface plasmon polaritons. (c) A metal nanoparticle of subwavelength size can act as a very strong dipolar scatterer due to a resonance of the free electron plasma. (d) Calculated field enhancement for a dimer of two silver spheres (25 nm diameter) spaced by a 10 nm gap, embedded in glass ($n = 1.5$), showing larger plasmonic field enhancement. Diagram taken from [47].

permittivity in metals gives rise to a complex, i.e., lossy dispersion for the SPPs. The propagation length of the SPPs is given by the imaginary part of the dispersion ($L_{SPP} = 1/2\,\mathrm{Im}(k_{SPP})$) and decreases significantly for higher frequencies near the plasmon resonance. For noble metals like gold and silver the propagation length can be in the order of 100 μm at frequencies away from the plasmon resonance. While silver plasmonic structures show typically long propagation lengths in the entire visible spectrum, application of gold plasmonic structures are normally limited to red and infrared parts of the spectrum. The propagation length of the SPPs, their confinement, and the associated field-enhancement per photon can be increased by using other types of plasmonic structures. For instance, planar stacks of metal-insulator-metal (MIM,

figure 1.3(b)) and insulator-metal-insulator (IMI) structures are two extensively studied plasmonic structures. In particular the thin gap in an MIM structure gives rise to a highly confined electromagnetic field in a region of about only a few 10 nm [49]. This high confinement enhances the light-matter interaction and very high spontaneous emission enhancements are expected for emitters placed in the dielectric gap of these plasmonic structures. In fact, very high Purcell enhancements have been proposed for MIM structures, with values in excess of 80 reconstructed from measurements by Belacel et al. [51].

Besides planar metal structures, lower dimensional structures like wires and particles also support plasmon resonances (Fig. 1.3(c)) . Plasmonic particles for emission control are often coined *antennas for light* for their ability to accelerate and redirect spontaneous emission [52]. Coupling of the emitters to the near-field of plasmonic structures not only helps to increase the spontaneous emission rate of emitters, but can also be exploited to reshape the far-field angular distribution of emitted light. In terms of achieving highest Purcell factors and brightness enhancements, the most successful antennas to date are dimer antennas (Fig. 1.3(d)), in particular the so-called bowtie antenna, composed of a narrow gap between the tips of two gold triangles. Single molecule studies have shown up to thousand-fold brightness enhancement, in large part due to enhancement of the laser pump field, and in part due to Purcell enhancements that go up to 20-fold [53–55]. In terms of plasmon antennas that redirect light, the most successful antennas to date are arrays of metal particles that mimick radio-antenna arrays [56–58], and antennas that consist of a small aperture in a metal film to contain the emitter, surrounded by a concentric circular outcoupler or outcoupling grating [51, 59–61]. Such antennas, and arrays thereof, have been pursued to improve single molecule microscopy [62], to improve solid state lighting [63–65] and to realize plasmonic implementations of quantum information processing that use II-VI nanocrystals [66, 67], or NV-center defects in diamond [68–70], as emitter.

1.3 This thesis

From the discussions in previous sections, it is evident that all spontaneous-emission-control experiments on single-emitters are concerned with three fundamental challenges. First, one needs to decide on how to choose the right emitter in terms of efficiency, brightness, stability, lifetime and spectral properties. Second, one needs to determine what nanophotonic structure should be placed around the emitter to completely control the rate, efficiency, emission angle, and polarization state of the emitter. Third, one needs to actually prove in experiment to what degree the control is obtained. To this end, one needs to map the local density of optical states, quantify the full angular distribution, and determine the polarization state of the emitted light.

In this thesis we address all these three challenges to some degree. In chapters 2, and 3, we are motivated by the first challenge, i.e., answering the question how one should pick the ideal emitter for an LDOS mapping experiment, or for inclusion as an ultimate single-photon source. For many applications, the ideal emitter should

simultaneously have high quantum efficiency, a fast emission rate (together giving high brightness), narrow spectral emission and a very good photostability. In practice no emitter is found to satisfy all these requirements, mainly because all emitters with desirable efficiency and brightness are unstable, and photobleach after a few minutes of experiments. The nitrogen-vacancy (NV) center in diamond has been proposed as the one exception to this rule, thereby realizing an ultimately stable single photon source [69, 70]. A disadvantage of NV centers is their broad spectral emission at room temperature [71]. NV centers are widely used in spintronics and magnetometry [72–76] thanks to their long spin coherence time, as single-photon sources in quantum-optics experiments [77–80], and as biological markers and sensors [81]. Specifically, NV centers in diamond nanocrystals are commonly considered ideal emitters over quantum-dots or fluorescent molecules for nanophotonics experiments, due to their photostability, mechanical stability and their nanoscale sizes. Recently, in our group, we initiated experiments in particular in framework of a scanning probe microscope realized by Frimmer et al. [82], in which we were able to map LDOS by measuring lifetime as function of position of a fluorescent bead above a sample, where the bead was attached to a sharp near-field scanning tip. The main disadvantage of this method is the fragility of the source as it bleaches after emission of approximately 10^8 photons (within one minute). NV centers in nanodiamonds would hence be an excellent replacement, considering their photostability [83–86]. However, this requires that NV centers in nanodiamond are robust near-unit quantum efficiency probes. While several groups have shown variations of the mean decay rate of ensembles of nanodiamond NV centers coupled to systems in which LDOS is modified [68, 87, 88], at the time that this work was started there was no evidence that single NV centers actually are efficient emitters, or controlled LDOS probes.

Motivated by this, in chapter 2, we present the results of our experimental characterization of single NV centers in many individual diamond nanocrystals of different diameters. We investigate the brightness and decay rate of the NV centers which both show broad distributions consistent with previous reports [87, 88]. However, we argue that the origin of this distribution is inconsistent with the common explanation of LDOS variations due to depolarization effects inside the small high-index crystals that affect the lifetimes of otherwise near-unit quantum efficiency nanodiamond NV centers. Instead, we argue that there is likely a broad distribution in radiative and nonradiative decay rates.

Having concluded from chapter 2 that single NV centers in nanodiamond are exceptionally heterogeneous in brightness and decay rate, in chapter 3, we turn to a calibration of their quantum efficiency in a Drexhage type of experiment [21]. We use two methods to apply known LDOS variations to single NV centers in individual nanodiamonds. In the first method, LDOS variations are effectuated using liquids of different refractive indices [24, 26]. Our findings show that NV centers in small diamond nanocrystals (with diameter about 25 nm) are insensitive to variations of LDOS. In conjunction with their brightness and decay rate measurements presented in chapter 2, we conclude that the quantum efficiency of these NV centers are widely distributed between 0% and 20%. In the second method, we use a nanomechanically

scanning micromirror with which the LDOS is varied [29]. This technique provides a reversible and nondestructive way of calibrating the quantum efficiency of individual emitters. Using this technique, we report, for the first time, calibrated quantum efficiencies of single NV centers in nominally identical diamond nanocrystals. We show that the quantum efficiencies of NV centers in 100 nm nanodiamonds is widely distributed between 10% and 90%, in contrast to the common assumption of near unity quantum efficiency of nanodiamond NV centers.

In chapter 4, we leave the topic of how to choose the best emitter, and instead turn to addressing parts of the second and the third challenges described earlier in this section. In this chapter, we report on simultaneous mapping of LDOS and directivity for a particularly promising new type of antenna known as plasmonic patch antenna which was first proposed by Steban et al. [89] and Belacel et al. [51]. The antenna consists of a circular metallic patch which is separated from an optically thick metallic mirror via a thin dielectric layer of about several 10 nm. Electromagnetic field is confined in the dielectric region, similar to confinement in a metal-insulator-metal geometry described earlier in section 1.2. Belacel et al. already demonstrated enhanced spontaneous emission of quantum dot emitters placed at the center of the gap of the patch antenna, claiming that the data imply Purcell factors up to 80 [51]. They showed that the patch antenna redirect the emission of the emitters into a narrow cone of about 30° full width at half maximum. Due to practical limitations they neither could map the LDOS of the patch antenna nor the angular emission of the antenna as a function of different position of the emitters. In chapter 4, we use angle-resolved cathodoluminescence imaging spectroscopy [90] to study the resonant modes of plasmonic patch antennas. In this method, a scanning beam of electrons excites the plasmonic modes of the patch antenna and provides high resolution maps of spectral and spatial modes of the patch antenna. We use a semi-analytical model to explain the observed modes which are essentially related to variations of the LDOS inside the antenna. We also show the results of experimentally measured angular emission patterns and directivity of the patch antenna. Using a distributed dipole model to account for the scattering of the SPPs at the edge of the antenna, we find good agreements with experiment for the high directionality of the patch antenna emission.

Finally, in chapter 5 we turn to quantifying the full angular distribution and polarization state of emitted light to address the third challenge. In the context of plasmonic antennas and metamaterials, understanding polarization degrees of freedom is deemed of increasing importance. In particular, strong coupling of the electric and magnetic dipoles in metamaterial structures has resulted in chiral scattering of the light from these structures [91–95]. Also, several groups study helicity of light scattered by nanostructures of various symmetry to elucidate optical scattering mechanisms in language of transfer of orbital- and spin angular momentum borrowed from the physics of electrons [96–98]. We have developed a microscopy method with which we can map the full polarization state of light scattered or emitted by a nanostructure, for many different emission directions simultaneously. To this end, we combine so-called ‘conoscopic’ or ‘back focal plane’ imaging in a high-NA microscope [5] with a polarimeter [99]. We present such k-space polarimetry results for plasmon-enhanced

fluorescence obtained in a system composed of ensembles of fluorophores residing in a central nanoaperture in a metal film that is surrounded by concentric, diffractive, grooves forming a bull's eye nanoantenna [59]. Our method allows to determine the degree of polarization, the degree of circular and linear polarization, as well as the orientation and eccentricity of the polarization ellipse for the polarized component of the emitted light.

References

[1] *Efficient blue light-emitting diodes leading to bright and energy-saving white light sources - scientific background on the nobel prize in physics 2014*, The Royal Swedish Academy of Sciences, 2014.

[2] *Super-resolved fluorescence microscopy - scientific background on the nobel prize in chemistry 2014*, The Royal Swedish Academy of Sciences, 2014.

[3] B. Lounis and M. Orrit, *Single-photon sources*, Rep. Prog. Phys. **68**, 1129 (2005).

[4] R. Rigler, M. Orrit, and T. Basché, editors, *Single Molecule Spectroscopy*, Springer Berlin / Heidelberg, 2002.

[5] L. Novotny and B. Hecht, *Principles of Nano-Optics*, Cambridge University Press, Cambridge, 2006.

[6] J. R. Lakowicz, *Principles of Fluorescence Spectroscopy*, Springer Berlin / Heidelberg, 2006.

[7] W. E. Moerner and L. Kador, *Optical detection and spectroscopy of single molecules in a solid*, Phys. Rev. Lett. **62**, 2535 (1989).

[8] M. Orrit and J. Bernard, *Single pentacene molecules detected by fluorescence excitation in a p-terphenyl crystal*, Phys. Rev. Lett. **65**, 2716 (1990).

[9] A. Small and S. Stahlheber, *Fluorophore localization algorithms for super-resolution microscopy*, Nature Meth. **11**, 267 (2014).

[10] D. Bouwmeester, A. Ekert, and A. Zeilinger, *The Physics of Quantum Information: Quantum Cryptography, Quantum Teleportation, Quantum Computation*, Springer, 2000.

[11] J. Qiu, *Quantum communications leap out of the lab*, Nature (News) **508**, 441 (2014).

[12] R. P. Feynman, *Simulating physics with computers*, Int. J. Theor. Phys. **21**, 467 (1982).

[13] I. M. Georgescu, S. Ashhab, and F. Nori, *Quantum simulation*, Rev. Mod. Phys. **86**, 153 (2014).

[14] H. J. Kimble, *The quantum internet*, Nature **453**, 1023 (2008).

[15] S. Haroche and J. M. Raimond, *Exploring the Quantum: Atoms, Cavities, And Photons*, Oxford University Press, 2006.

[16] S. Nakamura, S. Pearton, and G. Fasol, *The blue laser diode: the complete story*, Springer, 2000.

[17] J. Y. Tsao, M. H. Crawford, M. E. Coltrin, A. J. Fischer, D. D. Koleske, G. S. Subramania, G. T. Wang, J. J. Wierer, and R. F. Karlicek, *Toward smart and ultra-efficient solid-state lighting*, Adv. Opt. Mater. **2**, 809 (2014).

[18] R. Loudon, *The Quantum Theory of Light*, Oxford Science Publications, 1983.

[19] R. Sprik, B. A. van Tiggelen, and A. Lagendijk, *Optical emission in periodic dielectrics*, Europhys. Lett. **35**, 265 (1996).

[20] E. M. Purcell, *Spontaneous emission probabilities at radio frequencies*, Phys. Rev. **69**, 681 (1946).

[21] K. H. Drexhage, *Influence of a dielectric interface on fluorescence decay time*, J. Lumin. **1-2**, 693 (1970).

[22] H. Khosravi and R. Loudon, *Vacuum field fluctuations and spontaneous emission in a dielectric slab*, Proc. R. Soc. A **436**, 373 (1992).

[23] H. P. Urbach and G. L. J. A. Rikken, *Spontaneous emission from a dielectric slab*, Phys. Rev. A **57**, 3913 (1998).

[24] E. Snoeks, A. Lagendijk, and A. Polman, *Measuring and modifying the spontaneous emission rate of erbium near an interface*, Phys. Rev. Lett. **74**, 2459 (1995).

[25] R. M. Amos and W. L. Barnes, *Modification of the spontaneous emission rate of* Eu^{3+} *ions close to a thin metal mirror*, Phys. Rev. B **55**, 7249 (1997).

[26] M. J. A. de Dood, L. H. Slooff, A. Polman, A. Moroz, and A. van Blaaderen, *Modified spontaneous emission in erbium-doped* SiO_2 *spherical colloids*, Appl. Phys. Lett. **79**, 3585 (2001).

[27] M. D. Leistikow, J. Johansen, A. J. Kettelarij, P. Lodahl, and W. L. Vos, *Size-dependent oscillator strength and quantum efficiency of CdSe quantum dots controlled via the local density of states*, Phys. Rev. B **79**, 045301 (2009).

[28] P. Lunnemann, F. T. Rabouw, R. J. A. van Dijk-Moes, F. Pietra, D. Vanmaekelbergh, and A. F. Koenderink, *Calibrating and controlling the quantum efficiency distribution of inhomogeneously broadened quantum rods using a mirror ball*, ACS Nano **7**, 5984 (2013).

[29] B. C. Buchler, T. Kalkbrenner, C. Hettich, and V. Sandoghdar, *Measuring the quantum efficiency of the optical emission of single radiating dipoles using a scanning mirror*, Phys. Rev. Lett. **95**, 063003 (2005).

[30] K. J. Vahala, *Optical microcavities*, Nature **424**, 839 (2003).

[31] J. C. Knight, N. Dubreuil, V. Sandoghdar, J. Hare, V. LefevreSeguin, J. M. Raimond, and S. Haroche, *Characterizing whispering-gallery modes in microspheres by direct observation of the optical standing-wave pattern in the near field*, Opt. Lett. **21**, 698 (1996).

[32] D. K. Armani, T. J. Kippenberg, S. M. Spillane, and K. J. Vahala, *Ultra-high-q toroid microcavity on a chip*, Nature **421**, 925 (2003).

[33] A. Kiraz, P. Michler, C. Becher, B. Gayral, A. Imamoglu, L. Zhang, E. Hu, W. V. Schoenfeld, and P. M. Petroff, *Cavity-quantum electrodynamics using a single InAs quantum dot in a microdisk structure*, Appl. Phys. Lett. **78**, 3932 (2001).

[34] J. Reithmaier, G. Sek, A. Löffler, C. Hofmann, S. Kuhn, S. Reitzenstein, L. Keldysh, V. Kulakovskii, T. Reinecke, and A. Forchel, *Strong coupling in a single quantum dot-semiconductor microcavity system*, Nature **432**, 197 (2004).

[35] D. Englund, D. Fattal, E. Waks, G. Solomon, B. Zhang, T. Nakaoka, Y. Arakawa, Y. Yamamoto, and J. Vučković, *Controlling the spontaneous emission rate of single quantum dots in a two-dimensional photonic crystal*, Phys. Rev. Lett. **95**, 013904 (2005).

[36] L. Sapienza, H. Thyrrestrup, S. Stobbe, P. D. Garcia, S. Smolka, and P. Lodahl, *Cavity quantum electrodynamics with anderson-localized modes*, Science **327**, 1352 (2010).

[37] P. Lodahl, S. Mahmoodian, and S. Stobber, *Interfacing single photons and single quantum dots with photonic nanostructures*, Preprint arXiv:1312.1079 (2013).

[38] C. M. Soukoulis, editor, *Photonic Crystals and Light Localization in the* 21^{st} *Century*, Kluwer, Dordrecht, 2001.

[39] A. Yariv and P. Yeh, *Optical Waves in Crystals: Propagation and Control of Laser Radiation*, John Wiley & Sons, New York, 1983.

[40] E. Yablonovitch, *Inhibited spontaneous emission in solid-state physics and electronics*, Phys. Rev. Lett. **58**, 2059 (1987).

[41] S. John, *Strong localization of photons in certain disordered dielectric superlattices*, Phys. Rev. Lett. **58**, 2486 (1987).

[42] K. Busch and S. John, *Photonic band gap formation in certain self-organizing systems*, Phys. Rev. E **58**, 3896 (1998).

[43] M. Kaniber, A. Kress, A. Laucht, M. Bichler, R. Meyer, M.-C. Amann, and J. J. Finley, *Efficient spatial redistribution of quantum dot spontaneous emission from two-dimensional photonic crystals*, Appl. Phys. Lett. **91**, 061106 (2007).

[44] Q. Wang, S. Stobbe, and P. Lodahl, *Mapping the local density of optical states of a photonic crystal with single quantum dots*, Phys. Rev. Lett. **107**, 167404 (2011).

[45] P. Lodahl, A. F. van Driel, I. S. Nikolaev, A. Irman, K. Overgaag., D. Vanmaekelbergh, and W. L. Vos, *Controlling the dynamics of spontaneous emission from quantum dots by photonic crystals*, Nature **430**, 654 (2004).

[46] M. D. Leistikow, A. P. Mosk, E. Yeganegi, S. R. Huisman, A. Lagendijk, and W. L. Vos, *Inhibited spontaneous emission of quantum dots observed in a 3d photonic band gap*, Phys. Rev. Lett. **107**, 193903 (2011).

[47] A. F. Koenderink, *On the use of Purcell factors for plasmon antennas*, Opt. Lett. **35**, 4208 (2010).

[48] W. L. Barnes, A. Dereux, and T. W. Ebbesen, *Surface plasmon subwavelength optics*, Nature **424**, 824 (2003).

[49] S. A. Maier, *Plasmonics: Fundamentals and Applications*, Springer, 2007.

[50] C. Kittel, *Introduction to Solid State Physics*, John Wiley & Sons, 2005.

[51] C. Belacel, B. Habert, F. Bigourdan, F. Marquier, J.-P. Hugonin, S. Michaelis de Vasconcellos, X. Lafosse, L. Coolen, C. Schwob, C. Javaux, B. Dubertret, J.-J. Greffet, P. Senellart, and A. Maitre, *Controlling spontaneous emission with plasmonic optical patch antennas*, Nano Lett. **13**, 1516 (2013).

[52] M. Agio and A. Alú, editors, *Optical Antennas*, Cambridge University Press, 2013.

[53] A. Kinkhabwala, Z. Yu, S. Fan, Y. Avlasevich, K. Müllen, and W. E. Moerner, *Large single-molecule fluorescence enhancements produced by a bowtie nanoantenna*, Nature Photon. **3**, 654 (2009).

[54] H. Yuan, S. Khatua, P. Zijlstra, M. Yorulmaz, and M. Orrit, *Thousand-fold enhancement of single-molecule fluorescence near a single gold nanorod*, Angew. Chem. Int. Ed. **52**, 1217 (2013).

[55] D. Punj, M. Mivelle, S. B. Moparthi, T. S. van Zanten, H. Rigneault, N. F. van Hulst, M. F. Garcia-Parajo, and J. Wenger, *A plasmonic 'antenna-in-box' platform for enhanced single-molecule analysis at micromolar concentrations*, Nature Nanotechn. **8**, 512 (2013).

[56] A. F. Koenderink, *Plasmon nanoparticle array waveguides for single photon and single plasmon sources*, Nano Lett. **9**, 4228 (2009).

[57] A. G. Curto, G. Volpe, T. H. Taminiau, M. P. Kreuzer, R. Quidant, and N. F. van Hulst, *Unidirectional emission of a quantum dot coupled to a nanoantenna*, Science **329**, 930 (2010).

[58] T. Coenen, E. J. R. Vesseur, A. Polman, and A. F. Koenderink, *Directional emission from plasmonic yagi-uda antennas probed by angle-resolved cathodoluminescence spectroscopy*, Nano Lett. **11**, 3779 (2011).

[59] H. J. Lezec, A. Degiron, E. Devaux, R. A. Linke, L. Martin-Moreno, F. J. Garcia-Vidal, and

T. W. Ebbesen, *Beaming light from a subwavelength aperture*, Science **297**, 5582 (2002).

[60] H. Aouani, O. Mahboub, N. Bonod, E. Devaux, E. Popov, H. Rigneault, T. W. Ebbesen, and J. Wenger, *Bright unidirectional fluorescence emission of molecules in a nanoaperture with plasmonic corrugations*, Nano Lett. **11**, 637 (2011).

[61] H. Aouani, O. Mahboub, E. Devaux, H. Rigneault, T. W. Ebbesen, and J. Wenger, *Plasmonic antennas for directional sorting of fluorescence emission*, Nano Lett. **11**, 2400 (2011).

[62] J. Wenger and H. Rigneault, *Photonic methods to enhance fluorescence correlation spectroscopy and single molecule fluorescence detection*, Int. J. Mol. Sci. **11**, 206 (2010).

[63] G. Vecchi, V. Giannini, and J. Gómez Rivas, *Shaping the fluorescent emission by lattice resonances in plasmonic crystals of nanoantennas*, Phys. Rev. Lett. **102**, 146807 (2009).

[64] S. R. K. Rodriguez, S. Murai, M. A. Verschuuren, and J. Gòmez Rivas, *Light-emitting waveguide-plasmon polaritons*, Phys. Rev. Lett. **109**, 166803 (2012).

[65] G. Lozano, D. J. Louwers, S. R. Rodriguez, S. Murai, O. T. Jansen, M. A. Verschuuren, and J. Gomez Rivas, *Plasmonics for solid-state lighting: enhanced excitation and directional emission of highly efficient light sources*, Light Sci. Appl. **2**, e66 (2013).

[66] D. E. Chang, A. S. Sørensen, P. R. Hemmer, and M. D. Lukin, *Quantum optics with surface plasmons*, Phys. Rev. Lett. **97**, 053002 (2006).

[67] A. V. Akimov, A. Mukherjee, C. L. Yu, D. E. Chang, A. S. Zibrov, P. R. Hemmer, H. Park, and M. D. Lukin, *Generation of single optical plasmons in metal nanowires coupled to quantum dots*, Nature **450**, 402 (2007).

[68] R. Kolesov, B. Grotz, G. Balasubramanian, R. J. Stöhr, A. A. L. Nicolet, P. R. Hemmer, F. Jelezko, and J. Wrachtrup, *Wave–particle duality of single surface plasmon polaritons*, Nature Phys. **5**, 470 (2009).

[69] C. Kurtsiefer, S. Mayer, P. Zarda, and H. Weinfurter, *Stable solid-state source of single photons*, Phys. Rev. Lett. **85**, 290 (2000).

[70] A. Beveratos, R. Brouri, T. Gacoin, J.-P. Poizat, and P. Grangier, *Nonclassical radiation from diamond nanocrystals*, Phys. Rev. A **64**, 061802 (2001).

[71] F. Jelezko and J. Wrachtrup, *Single defect centres in diamond: A review*, Phys. Status Solidi A **203**, 3207 (2006).

[72] A. Gruber, A. Dräbenstedt, C. Tietz, L. Fleury, J. Wrachtrup, and C. v. Borczyskowski, *Scanning confocal optical microscopy and magnetic resonance on single defect centers*, Science **276**, 2012 (1997).

[73] M. Loretz, T. Rosskopf, J. M. Boss, S. Pezzagna, J. Meijer, and C. L. Degen, *Single-proton spin detection by diamond magnetometry*, Science , 10.1126/science.1259464 (2014).

[74] C. L. Degen, *Scanning magnetic field microscope with a diamond single-spin sensor*, Appl. Phys. Lett. **92**, 243111 (2008).

[75] J. M. Taylor, P. Cappellaro, L. Childress, L. Jiang, D. Budker, P. R. Hemmer, A. Yacoby, R. Walsworth, and M. D. Lukin, *High-sensitivity diamond magnetometer with nanoscale resolution*, Nature Phys. **4**, 810 (2008).

[76] G. Balasubramanian, I. Y. Chan, R. Kolesov, M. Al-Hmoud, J. Tisler, C. Shin, C. Kim, A. Wojcik, P. R. Hemmer, A. Krueger, T. Hanke, A. Leitenstorfer, R. Bratschitsch, F. Jelezko, and J. Wrachtrup, *Nanoscale imaging magnetometry with diamond spins under ambient conditions*, Nature **455**, 648 (2008).

[77] F. Jelezko, T. Gaebel, I. Popa, A. Gruber, and J. Wrachtrup, *Observation of coherent oscillations in a single electron spin*, Phys. Rev. Lett. **92**, 076401 (2004).

[78] T. van der Sar, Z. H. Wang, M. S. Blok, H. Bernien, T. H. Taminiau, D. M. Toyli, D. A. Lidar, D. D. Awschalom, R. Hanson, and V. V. Dobrovitski, *Decoherence-protected quantum gates for a hybrid solid-state spin register*, Nature **484**, 82 (2012).

[79] L. Childress, M. V. Gurudev Dutt, J. M. Taylor, A. S. Zibrov, F. Jelezko, J. Wrachtrup, P. R. Hemmer, and M. D. Lukin, *Coherent dynamics of coupled electron and nuclear spin qubits in diamond*, Science **314**, 281 (2006).

[80] P. Neumann, N. Mizuochi, F. Rempp, P. Hemmer, H. Watanabe, S. Yamasaki, V. Jacques, T. Gaebel, F. Jelezko, and J. Wrachtrup, *Multipartite entanglement among single spins in diamond*, Science **320**, 1326 (2008).

[81] C.-C. Fu, H.-Y. Lee, K. Chen, T.-S. Lim, H.-Y. Wu, P.-K. Lin, P.-K. Wei, P.-H. Tsao, H.-C. Chang, and W. Fann, *Characterization and application of single fluorescent nanodiamonds as cellular biomarkers*, Proc. Natl. Acad. Sci. U.S.A. **104**, 727 (2007).

[82] M. Frimmer, Y. Chen, and A. F. Koenderink, *Scanning emitter lifetime imaging microscopy for spontaneous emission control*, Phys. Rev. Lett. **107**, 123602 (2011).

[83] A. Cuche, A. Drezet, J.-F. Roch, F. Treussart, and S. Huant, *Grafting fluorescent nanodiamonds onto optical tips*, J. Nanophotonics **4**, 043506 (2010).

[84] P. Maletinsky, S. Hong, M. S. Grinolds, B. Hausmann, M. D. Lukin, R. L. Walsworth, M. Loncar, and A. Yacoby, *A robust scanning diamond sensor for nanoscale imaging with single nitrogen-vacancy centres*, Nat. Nanotechnol. **7**, 320 (2012).

[85] R. Beams, D. Smith, T. W. Johnson, S.-H. Oh, L. Novotny, and A. N. Vamivakas, *Nanoscale fluorescence lifetime imaging of an optical antenna with a single diamond nv center*, Nano Lett. **13**, 3807 (2013).

[86] A. W. Schell, P. Engel, J. F. M. Werra, C. Wolff, K. Busch, and O. Benson, *Scanning single quantum emitter fluorescence lifetime imaging: Quantitative analysis of the local density of photonic states*, Nano Lett. **14**, 2623 (2014).

[87] F. A. Inam, T. Gaebel, C. Bradac, L. Stewart, M. J. Withford, J. M. Dawes, J. R. Rabeau, and M. J. Steel, *Modification of spontaneous emission from nanodiamond colour centres on a structured surface*, New J. Phys. **13**, 073012 (2011).

[88] P. V. Ruijgrok, R. Wüest, A. A. Rebane, A. Renn, and V. Sandoghdar, *Spontaneous emission of a nanoscopic emitter in a strongly scattering disordered medium*, Opt. Express **18**, 6360 (2010).

[89] R. Esteban, T. V. Teperik, and J. J. Greffet, *Optical patch antennas for single photon emission using surface plasmon resonances*, Phys. Rev. Lett. **104**, 026802 (2010).

[90] T. Coenen, E. J. R. Vesseur, and A. Polman, *Angle-resolved cathodoluminescence spectroscopy*, Appl. Phys. Lett **99**, 143103 (2011).

[91] I. M. Hancu, A. G. Curto, M. Castro-López, M. Kuttge, and N. F. van Hulst, *Multipolar interference for directed light emission*, Nano Lett. **14**, 166 (2014).

[92] A. G. Curto, T. H. Taminiau, G. Volpe, M. P. Kreuzer, R. Quidant, and N. F. van Hulst, *Multipolar radiation of quantum emitters with nanowire optical antennas*, Nat. Commun. **4**, 1750 (2013).

[93] T. H. Taminiau, S. Karaveli, N. F. van Hulst, and R. Zia, *Quantifying the magnetic nature of light emission*, Nat. Commun. **3**, 979 (2012).

[94] F. Bernal Arango, T. Coenen, and A. F. Koenderink, *Underpinning hybridization intuition for complex nanoantennas by magnetoelectric quadrupolar polarizability retrieval*, ACS Photonics **1**, 444 (2014).

[95] M. Schäferling, X. Yin, and H. Giessen, *Formation of chiral fields in a symmetric environment*, Opt. Express **20**, 26326 (2012).

[96] F. J. Rodríguez-Fortuno, G. Marino, P. Ginzburg, D. O'Connor, A. Martínez, G. A. Wurtz, and A. V. Zayats, *Near-field interference for the unidirectional excitation of electromagnetic guided modes*, Science **340**, 328 (2013).

[97] P. Genevet, J. Lin, M. A. Kats, and F. Capasso, *Holographic detection of the orbital angular*

momentum of light with plasmonic photodiodes, Nat. Commun. **3**, 1278 (2012).

[98] L. Allen, M. W. Beijersbergen, R. J. C. Spreeuw, and J. P. Woerdman, *Orbital angular momentum of light and the transformation of laguerre-gaussian laser modes*, Phys. Rev. A **45**, 8185 (1992).

[99] C. Fallet, T. Novikova, M. Foldyna, S. Manhas, B. H. Ibrahim, A. De Martino, C. Vannuffel, and C. Constancias, *Overlay measurements by mueller polarimetry in back focal plane*, J. Micro-Nanolithogr. MEMS MOEMS **10**, 033017 (2011).

2

Statistical characterization of nitrogen-vacancy centers emission

Nitrogen-vacancy (NV) centers in diamond are generally recognized as highly promising as indefinitely stable highly efficient single-photon sources. We report an experimental quantification of the brightness, radiative decay rate, nonradiative decay rate and quantum efficiency of single NV centers in diamond nanocrystals. Our experiments show that the commonly observed large spread in fluorescence decay rates of NV centers in nanodiamond is inconsistent with the common explanation of large nanophotonic mode-density variations in the ultra-small high-index crystals at near-unity quantum efficiency.

2.1 Introduction

The large promise of quantum-optical technologies to enable secure communication and novel computation architectures sets stringent targets for the quality of photon sources and detectors. In order to meet these demands many efforts are currently devoted to realizing bright sources of single photons [1, 2]. These developments at the same time require novel nanophotonic engineering designs around emitters to enhance light-matter interaction strength as well as indefinitely stable two-level systems that neither bleach, blink, nor spectrally jump. On the nanophotonic engineering side, many different systems have been proposed to control whereto, how fast and with which polarization an emitter emits provided that one manages to locate it exactly

in the right location. These systems include whispering-gallery-mode cavities [2], micropillars and cylindrical wires [3–5], photonic crystal microcavities [6–8], photonic crystal waveguides near cut-off [9, 10], Anderson localizing systems [11], as well as ultrabroadband plasmonic waveguides and antennas [12–15]. Essentially, all these techniques modify the photonic environment of an emitter via the Local Density of Optical States (LDOS) [16, 17]. The LDOS quantifies the light-matter interaction strength that appears in Fermi's Golden Rule for spontaneous emission. Placing the emitter at a position where the LDOS is enhanced, first implies a much higher fluorescence decay rate. Second, if the LDOS enhancement is due to a select set of designed modes as in a cavity or waveguide, the enhanced rate is accompanied by extraction of photons preferentially via these enhanced modes. Thus, photonic engineering promises optimum brightness, dynamics, and collection efficiency. As regards the choice of emitter, a wide variety of systems have been used. Unfortunately, all choices appear to carry large disadvantages when going beyond pilot studies: most dye molecules photobleach [18], II-VI quantum dots [19, 20] blink as well as bleach, and many systems, such as III-V emitters, only have desirable properties when cooled to cryogenic temperatures [3–7, 10, 11]. A promising candidate to provide an indefinitely stable source [21–23] that furthermore allows room-temperature spin-control [24–28] is the nitrogen-vacancy (NV) color center in diamond. NV centers are point defects in diamond structure where a carbon atom is substituted by a nitrogen atom adjacent to a lattice vacancy (figure 2.1(a)). Offsetting their advantageous stability, a disadvantage of NV centers as single photon sources is their very broadband fluorescence emission compared to other quantum-emitters at room temperature, which makes frequency-selective photonic engineering challenging.

When one chooses diamond NV centers as emitters for quantum optics in nanophotonic devices, one can either aim to manipulate emission by fabricating photonic structures directly in diamond [29–31], or one can assemble diamond nanocrystals with photonic structures of a different material [32–39]. Recently, pick-and-place strategies [35–37] were reported in which a single nanoparticle from a diluted powder of diamond nanocrystals dispersed on a substrate is selected and pushed to a desired location by a scanning probe, such as an atomic-force-microscopy tip, or a manipulator in a scanning electron microscope. Reports of this technique span from the coupling of nanodiamonds to photonic-crystal cavities [36, 37] to coupling to plasmonic antennas and nanowires [38, 39]. As a variation of the pick-and-place strategy, a few groups recently developed so called 'scanning-emitter' near-field microscopes in which nanosources are not deposited irreversibly inside a nanostructure, but actually remain attached to a scanning- probe [40–43]. The advantage of such a scanning probe approach is that one can first construct a full map of the LDOS using near-field lifetime imaging to determine where one should ultimately place the nanosource [43]. Microscopy with a light-source as a near-field tip is interesting as a microscopy technique, but only viable if the nanosource is indefinitely stable and does not blink, for which nanodiamonds appear the sole candidate [41, 42, 44–47]. Moreover nanodiamond scanning probes offer the possibility to create nanometer sized local magnetometry probes read out optically by NV spectroscopy [48–51].

In view of the scanning probe microscopy and assembly efforts that seek to combine nanodiamonds and photonic structures, one question stands out as of key importance: given an ensemble of individual nanodiamonds, how does one recognize the ideal nanocrystal? This question is especially relevant given that both fabrication of the photonic structure *and* the intended scanning-probe procedure is highly laborious [35]. Naively, one might think that all nanocrystals of subwavelength size that contain a single NV center will be equally suited, since an NV center is a defect of uniquely defined composition and geometry in the diamond crystalline matrix. However, many workers on diamond nanocrystals have established that NV centers in diamond nanocrystals actually show a distribution of photophysical properties, such as brightness, stability, and decay rates [28, 36, 52–55]. This distribution is usually ascribed to the fact that even though all NV centers are expected to have unit quantum efficiency and the same oscillator strength, these identical unit-quantum-efficiency sources are each differently placed inside their nanoscopic high-index diamond grains [21–23, 53, 55]. This is anticipated to cause different decay rates, due to the fact that the LDOS even in an isolated nanoscopic object varies as a function of position and dipole orientation [56].

In this chapter we address the question how to recognize the ideal nanocrystal from an ensemble of nanocrystals on basis of the requirement that the ideal nanocrystal must contain a single NV center that fluoresces with a high quantum yield, so that it can be useful as a reporting probe of LDOS in nanophotonic systems. We report that the commonly made assumption that NV centers are unit-efficiency dipoles randomly distributed in high index nanoscopic objects is not reconcilable with measured brightness and decay rate histograms data for nanocrystals in the frequently used size ranges around 20–50 nm and 50–150 nm. On basis of the wide distribution of brightness and rate that can not be explained by LDOS variations between nanoparticles alone we conclude that both the radiative and nonradiative rates are broadly distributed.

2.2 Experiment and methods

2.2.1 Sample preparation

Since single NV centers in nanodiamonds are comparatively dim emitters that require high excitation powers, it is essential to avoid background fluorescence when performing fluorescence microscopy. Therefore, we use intrinsically low-fluorescent quartz coverslips (Esco Products) as sample substrates that were cleaned by 15 min sonication in water followed by a 15 min bath in base Piranha (NH_3(aq., 30 %) : H_2O_2(aq., 30 %) : H_2O mixed at ratio 1:1:5, at 75 °C). In our work it is essential that we can unambiguously pinpoint the position of nanodiamonds containing NV centers in the course of the measurement, so that we can revisit the same color center after, for instance, material-deposition steps. To this end we define an array of markers on top of the coverslips using electron-beam lithography. To remove any organic residues after the lift-off process, we treated the coverslips with a mild O_2-plasma descum (Oxford Instruments Plasmalab 80+, using a 5 mTorr,

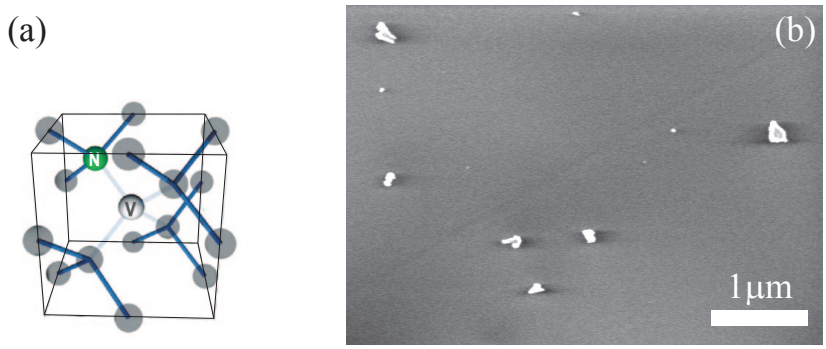

Figure 2.1: (a) Schematic of NV center structure (diagram taken from Ref. [57]). (b) Scanning electron micrograph of dispersed nanodiamonds (Microdiamant MSY 0–0.2) on glass coverslide.

25 sccm O_2 plasma). As sources for NV centers, we use solutions of monocrystalline synthetic nanodiamonds (Microdiamant MSY) with a narrow size tolerance obtained from Microdiamant AG, Lengwil, Switzerland. We note that these nanoparticles have been used recently by a large number of groups in experiments that rely on fluorescence [26, 27, 32, 36, 38, 39, 52–54]. We use these nanodiamonds exactly in the manner as described by Schietinger et al, i.e. without further washing or purification steps [36, 58]. We prepared samples from diamond slurries with two different size distributions by spin-coating aqueous solutions of nanodiamonds that are diluted to a concentration of 1% of the as-received stock solutions on the cleaned and patterned coverslips. The first type of sample, from here on referred to as '25 nm diamond sample' was made from Microdiamant MSY 0–0.05, which nominally has sizes from 0 to 50 nm. These diamonds have a median diameter of 26 nm, with fewer than 1% of the diamonds above 50 nm in size, according to particle sizing performed on this batch of diamonds by the manufacturer. The second type of sample ('100 nm diamond sample') was made from Microdiamant MSY 0–0.2, which nominally has crystal sizes ranging from 0 to 200 nm. This ensemble has crystals with median diameter 108 nm, and fewer than 1% of particles above 175 nm in size, again according to the size-distribution histogram supplied by the manufacturer. Scanning electron microscope (SEM) inspection indicated a size distribution of nanodiamonds consistent with these specifications. The average density of spin-coated nanodiamonds on the coverslips as checked through the SEM images was about 1 to 8 μm^{-2} depending on the sample, assuring that only a few nanodiamonds are illuminated at the diffraction-limited focus of the objective (figure 2.1(b)). Only a small fraction of the nanodiamonds are fluorescent, and an even smaller fraction fluoresces due to an NV center. We identify a diamond as containing at least one NV center, if we can clearly identify the characteristic zero phonon line (ZPL) [21–23, 59] in its emission spectrum according to the criterion we specify in

section 2.2.3. With this criterion, for 100 nm nanodiamonds at an average density of 1 μm^{-2}, we found on average one NV center in an area equal to $50 \times 50\,\mu m^2$, while for 25 nm nanodiamonds at an average density of 5 μm^{-2} we found on average 2 NV centers in a $100 \times 100 \mu\,m^2$ area. These numbers translate to identifying fewer than 0.05% of the 100 nm nanodiamonds, and fewer than 0.001% of the 25 nm diamonds as containing a (single) NV center beyond doubt. Schietinger et al [60] have reported a higher density of NV centers of about 1% for MSY 0–0.05 nanodiamonds. A difference in reported NV center densities could be either due to a different degree of strictness in labeling a fluorescent emitter as an NV center beyond doubt (see section 2.2.3 for our criteria), or alternatively to batch-to-batch variations in nanodiamond slurries.

2.2.2 Experimental setup

The optical setup, sketched in figure 2.2, consists of an inverted confocal fluorescence microscope equipped with a sample scanning piezo stage. NV centers are optically excited at 532 nm using either a frequency-doubled Nd:YAG pulsed laser (Time-Bandwidth, 10 MHz repetition rate) or a continuous-wave (CW) diode laser (CNI). The laser beam is focused through the coverslip to a diffraction-limited spot on top of the sample, using a 100× dry objective with a numerical aperture of 0.9 (Nikon CFI Plan Fluor). The same objective collects the luminescence and guides it through a long-pass filter (580 nm cut-off) before it is imaged on a CCD camera (Nikon DS-Qi1Mc) or confocally detected on one or two avalanche photodiodes (APD) with single-photon sensitivity (both APDs: id Quantique id100-20ULN). The APDs in combination with a sub-nanosecond-resolution 16 channel correlator (Becker & Hickl, DPC-230) allow for single-photon counting. The correlator can perform time-correlated single-photon-counting (TCSPC) lifetime measurements by correlation of detection events with laser pulse arrival times, or photon-photon correlations using multiple APDs. We use a second APD in a Hanbury-Brown and Twiss (HBT) configuration to measure photon correlation statistics (antibunching) at CW excitation. Single-nanocrystal spectra are collected using an imaging spectrometer (SpectraPro 2300i) equipped with a thermoelectrically cooled back-illuminated Si CCD array detector (Princeton Instruments PIXIS:100B).

2.2.3 Measurement procedure to characterize single nanodiamonds

In order to find nanodiamonds containing NV centers, the sample is first pumped with wide-field laser illumination and the fluorescence is imaged on the CCD camera. We use an illumination power of 20 mW, over an area of about 30 μm diameter. Under these conditions, any potential NV center will appear as a diffraction-limited fluorescent spot. Subsequently, we switch to diffraction-limited illumination and position the potential candidate at the laser focus using a piezostage (figure 2.3(a)), and using about 0.5 to 1 mW of power. The fluorescence intensity of the emitter is quantified by integration over a fixed CCD area which is indicated by the green line in figure 2.3(a). At this stage,

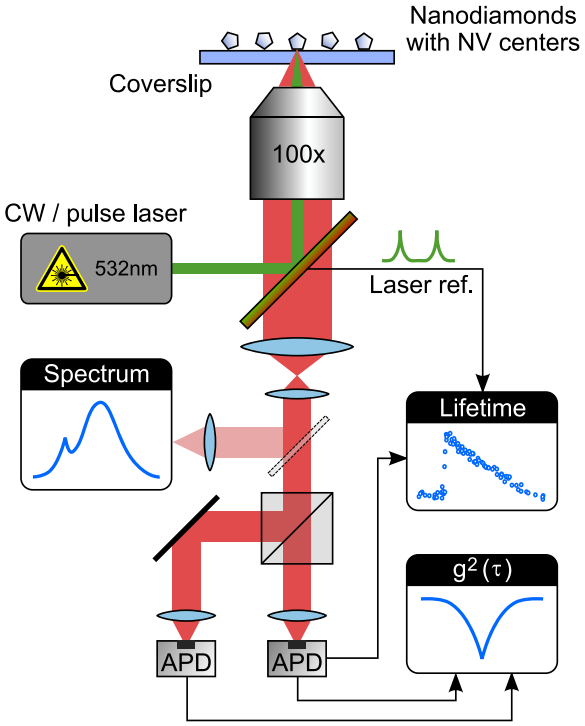

Figure 2.2: Schematic of the experimental setup. Spin-coated nanodiamonds on quartz coverslip are illuminated by 532 nm laser through a 100× dry objective. The emitted fluorescence can be guided to spectrometer or to APDs to measure the lifetime and second order correlation function $g^{(2)}$ of the emitted photons.

we spectrally resolve the fluorescence from the isolated emitter with the spectrometer to specifically find the characteristic zero phonon line of NV centers at a wavelength of about 638 nm (figure 2.3(b)) [21–23]. On basis of the ZPL, we either discard the emitter (absence of ZPL), or identify the nanodiamond as having one or more NV centers (ZPL well above the detector and photon-counting noise). In order to verify that the emission originates from a single center, for each identified NV center, we record a second-order correlation function $g^{(2)}(\tau)$ defined as

$$g^{(2)}(\tau) = \frac{\langle I_1(t) \cdot I_2(t+\tau) \rangle}{\langle I_1(t) \rangle \cdot \langle I_2(t+\tau) \rangle}$$

where $I_1(t)$ and $I_2(t)$ are time-resolved photon counts on each of the two APDs. To this end, we pump the center with the CW laser at a power of about 1 mW to achieve count rates on the order of about 5×10^4 counts per second on each APD and integrate for about 1000 s to obtain reasonable correlation statistics of around 30 coincidences

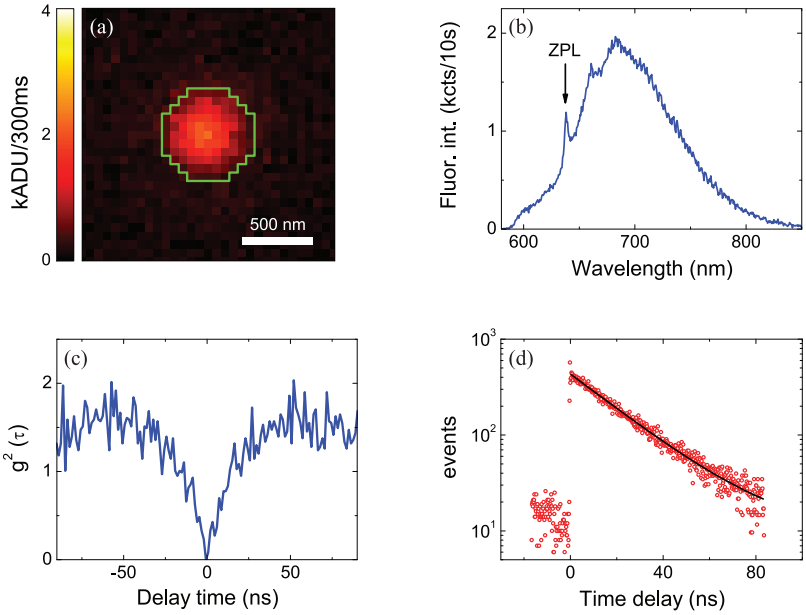

Figure 2.3: (a) CCD image of the fluorescence from a potential NV center positioned at the focus of the laser (1 ADU on our CCD camera corresponds to approximately 6 detected photons). Green line indicates an integration area over which the fluorescence intensity of the emitter is evaluated. (b) Typical spectrum of an NV center expressing the characteristic zero phonon line at 638 nm. (c) Second-order correlation function $g^{(2)}$ of an NV center obtained by CW excitation. The zero dip in $g^{(2)}$ curve confirms the single nature of the center. (d) Background-corrected decay traces of photons emitted from an NV center (red circles, total acquisition time 20 s) with a single-exponential fit (black curve) to extract the lifetime.

per 658 ps bin. Figure 2.3(c) shows a typical background-subtracted $g^{(2)}(\tau)$ curve, with a clearly resolved minimum at zero delay $\tau = 0$ that is well below 0.5, indicating that emission is from a single NV center. Here, the background is subtracted via the procedure reported in [21], based on a measurement directly next to the NV center where we expect identical fluorescence background from the substrate. The background measured only from the substrate shows a Poissonian emission statistics. The bunching in the $g^{(2)}(\tau)$ in figure 2.3(c) at longer delay times (visible at $\tau \approx \pm 50$ ns) is well known to be due to the presence of a shelving state as described by Beveratos et al. [23]. Once we have identified a nanodiamond as containing a single NV center based on its spectrum and antibunching signature, we measure its fluorescence lifetime by switching to pulsed laser excitation. The lifetime of each center is extracted by fitting a single-exponential decay incorporating a small constant background to the decay histogram of emitted photons as shown in figure 2.3(d). We note that the substrate itself has a weak background fluorescence that shows a time dependence. We correct for this artifact by

collecting decay traces from the sample pumped directly next to the NV center. We parameterize the background by a tri-exponential fit (with a dominant sub-nanosecond lifetime) which we subtract from the NV center decay histogram prior to fitting. The residual background is around 10 counts per bin for a total acquisition time of about 20 s.

2.3 Statistics on fluorescence parameters of large nanodiamonds

In this section we report on statistical distributions of the various fluorescence characteristics, i.e. brightness, $g^{(2)}$ and lifetime, that we collected on both nanodiamond size ranges. We first discuss the '100 nm diamond' sample, containing 0–200 nm size nanodiamonds with 108 nm median diameter, and subsequently we discuss the '25 nm diamond' sample with 0–50 nm size nanodiamonds and 26 nm median diameter. For each sample, our statistics is based on identifying 30 to 40 NV centers as described in section 2.2.3.

2.3.1 Distribution of brightness and relation to $g^{(2)}(0)$

As a first step in the characterization process, we have measured the brightness of nanodiamonds that show a clear ZPL line. Figure 2.4(a) shows a histogram of measured brightnesses as quantified by intensity on the CCD at fixed illumination intensity (solid bars). The intensity on the CCD is obtained by summing all pixels within the diffraction-limited image of each diamond (green line in figure 2.3(a)). We observe a wide distribution of intensities, spanning from 50×10^3 to 210×10^3 ADU's (Analog Digital Units) on the CCD per 300 ms exposure time. At an estimated photon-to-ADU conversion factor of 6 for our CCD camera, these brightnesses correspond to 1×10^6 to 4.2×10^6 collected photons per second, at a pump power of 1mW in a diffraction limited spot, supplied by the CW laser. First, these numbers show, at least assuming that NV centers are reasonably efficient emitters, the absorption cross sections of nanodiamond NV centers at 532 nm pump wavelength are an order of magnitude below those of dyes and II-VI quantum dot nanocrystals. Second, there is a wide distribution of brightnesses of over a factor 3 to 4 from nominally identical emitters. As described in section 2.2.3, some nanodiamonds may have multiple NV centers, especially in the case of big nanoparticles. To exclude that brightness variations are due to multiple NV centers, we screen the nanodiamonds on basis of $g^{(2)}$ minimum values. Figure 2.4(b) shows a correlation plot, plotting the fluorescence intensities of all identified NV centers on 100 nm nanodiamond sample versus the recorded value of $g^{(2)}$ at zero delay ($g^{(2)}(\tau = 0)$). We find that not just the brightness, but also the minimum in $g^{(2)}$ is distributed with minima in $g^{(2)}$ ranging from 0 to 0.75. The minimum in $g^{(2)}(0)$ is only weakly correlated with collected intensity, especially via an apparent stepwise increase in the fluorescence intensity as $g^{(2)}(0)$ reaches above ≈ 0.5. Such a stepwise increase would be expected since the minimum in $g^{(2)}$ scales with the number

of emitters n as $1-1/n$. For $g^{(2)}(0) \gtrsim 0.5$ more than a single fluorescent center is involved in the emission, resulting in higher fluorescence intensities on average.

In the remainder we concentrate our analyses on single NV centers, i.e. those nanocrystals for which $g^{(2)}(0) < 0.5$. In figure 2.4(a) , we overplot a histogram of fluorescence intensities of the subset of centers with $g^{(2)}(0) < 0.5$ as patterned bars. The histogram shows a wide fluorescence distribution, with a factor of three difference between brightest and dimmest NV centers, and with a relative distribution of about 30% around the most frequent value. Figure 2.4(b) shows that for the single NV centers the wide distribution in fluorescence intensities notably does not show any correlation to $g^{(2)}(0)$ values.

It should be noted that brightness differences between NV centers could originate from variations in the collection efficiency induced by the different emission dipole moment orientation of each NV center [61]. For the nominal NA of our microscope objective, the detection efficiency for emission of a dipole source is expected to vary as $0.17 + 0.28\sin^2\theta$, as a function of angle θ between dipole and sample surface normal. According to Ref. [62], however, an NV center is not a linear dipole but has two dipole moments of equal size in the plane perpendicular to the NV axis. Our calculations show that for a random distribution of NV orientations, the collection efficiency is centered at around 35%, with 80% of NV centers expected to have collection efficiency between 30% and 40%. Similarly, NV orientation is expected to contribute to a distribution in brightness through orientation-dependent overlap of the absorption dipole with the linear pump polarization. NV orientation hence explains part of, if not the full detected intensity distribution of the NV centers in figure 2.4(a). Further potential causes of brightness variations are variations in the quantum efficiency or the absorption cross-section as well as the dynamics of the metastable state in NV centers [63, 64] that can significantly affect the brightness of an NV center.

2.3.2 Correlation of emission rates and brightness

To examine whether quantum efficiency (QE) effects may be at play, we have measured fluorescence decay rates for each identified single NV center. We plot a histogram of the measured decay rates in figure 2.4(c). We observe a very wide distribution, with the slowest emitters decaying almost 4 times more slowly than the fastest ones. The most frequently occurring decay rate is around $\gamma_{\mathrm{tot}} = 0.03\,\mathrm{ns}^{-1}$ (corresponding to about 33 ns). The time constant of 33 ns is appreciably slower than the fluorescence lifetime of NV centers in bulk diamond, for which the accepted literature value is 11.6 ns [23]. This much slower decay as well as the occurrence of a distribution of rates is in agreement with previously reported values [53, 55]. If the hypothesis that quantum efficiency variations are responsible for the large variability in brightness in figure 2.4(a) is valid, one might expect a correlation between the brightness and decay rate of the emitters. We plot the measured brightness as a function of decay rate for each NV center in figure 2.4(d) which, however, displays no clear correlation. Importantly, we note that the measured quantity here is the total decay rate $\gamma_{\mathrm{tot}} = \gamma_{\mathrm{r}} + \gamma_{\mathrm{nr}}$ which reflects both variations of radiative decay rate γ_{r} and nonradiative decay rate γ_{nr}, whereas

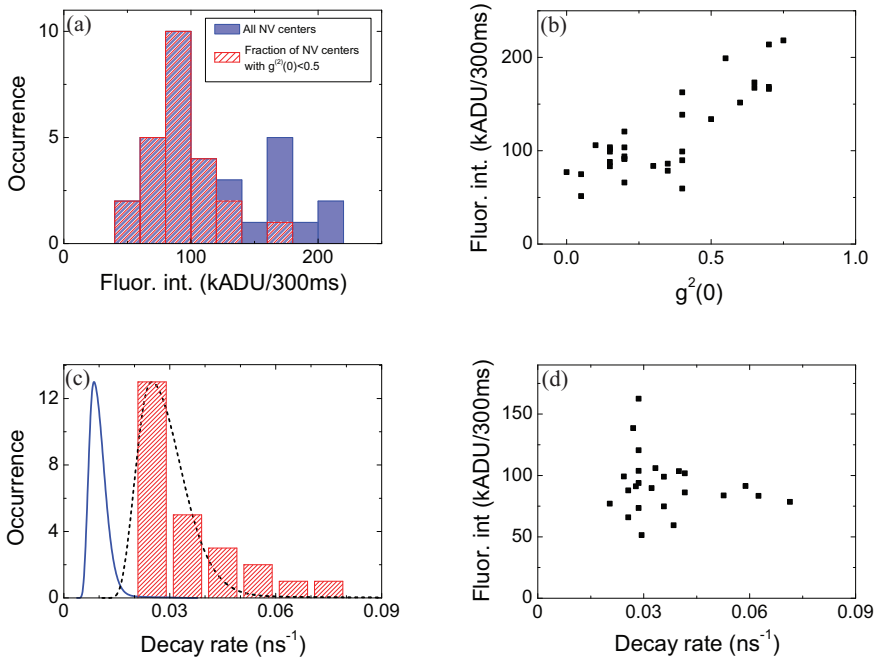

Figure 2.4: Statistics for 100 nm nanodiamonds. (a) Histogram of fluorescence intensity of NV centers (1 ADU on our CCD camera corresponds to approximately 6 detected photons). Solid bars indicate the fluorescence distribution of all identified NV centers whereas patterned bars are related to the fraction of single NV centers identified by $g^{(2)}(0) < 0.5$ in (b). (b) Fluorescence intensity as a function of $g^{(2)}(0)$. (c) Bars: histogram of decay rates of emitters with $g^{(2)}(0)$. Solid line: calculated distribution of LDOS/LDOS$_{vac}$ according to nanodiamond size distribution, normalized to the rate of NV centers in bulk diamond. Dotted line: free scaling of the calculated LDOS distribution (solid line) to match the experimental histogram (bars). (d) Fluorescence intensity as a function of decay rate for emitters with $g^{(2)}(0) < 0.5$ (decay rate error bars are within symbol size). Error bars are comparable to plot symbol size.

the quantum efficiency is given by γ_r/γ_{tot}. Based on the collection efficiency of our microscope (~ 10 %), the count rates in Figure 2.4 correspond to an intermediate (most data) to strong (data point at and above 150 kADU/300 ms))excitation regime, where the photon emission rate is approximately 0.2 to 0.9 times the total decay rate γ_{tot}. Both if one assumes to be in saturation, and below saturation, one expects the fastest decay to imply highest brightness if one assumes γ_{nr} to be approximately constant but γ_r to be distributed. This conclusion is not strongly supported by the data. If conversely we assume γ_r to be approximately constant across NV centers while γ_{nr} is distributed, one would expect highest brightness to correlate with the slowest decay rate (lowest γ_{nr}), a hypothesis also not strongly supported by the data. Specifically, we find that the subset of crystals around the most frequent brightness show the full spread of decay constants, while conversely also the subset of crystals that have decay

constant around the most frequent rate, contain the full range of brightnesses. The lack of strong correlation between decay rate and brightness suggests that the quantum efficiency of NV centers in nanodiamonds as we study here is distributed and not equal to unity for all NV centers. However, as discussed in the previous section, we note that due to variations in the collection efficiency and the unknown dipole orientation of NV centers, the interpretation of brightness in terms of quantum efficiency is convoluted. Therefore, it is essential to use a well-calibrated method in order to determine the quantum efficiency of the NV centers, as we discuss in section 3.3.1.

2.3.3 Common LDOS argument for rate variation in nanodiamond

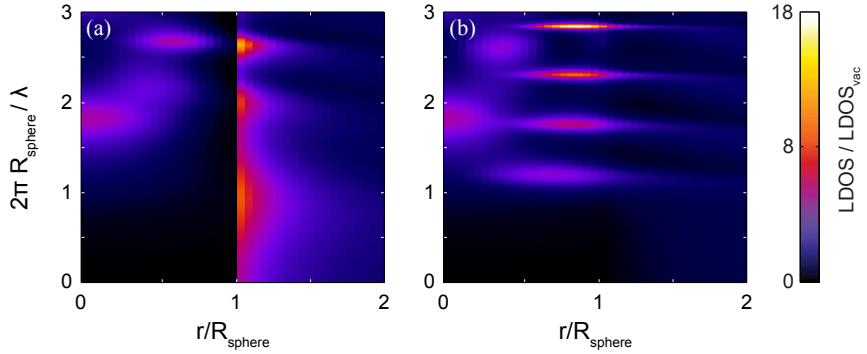

Figure 2.5: LDOS map of dielectric spheres ($\varepsilon_{\text{sphere}} = 5.85$) as function of normalized wavenumber ($2\pi R_{\text{sphere}}/\lambda$) and dipole position in ($r/R_{\text{sphere}} < 1$) and out of ($r/R_{sphere} > 1$) the sphere for (a) radially-oriented, and (b) tangentially-oriented dipole moments. LDOS values are normalized to the value in vacuum.

Many workers had already noticed that nanodiamond decay rates are widely distributed [28, 53, 55]. The variation is commonly attributed to variations solely in the radiative rate γ_{r} due to a local-density-of-photonic-states effect, assuming zero nonradiative decay (i.e. unit quantum efficiency). The hypothesis, explained in detail by Inam et al [53], is that variations are in large part due to the fact that the LDOS experienced by an NV center is influenced by the nanoscale geometry of its environment, i.e. the fact that the source is situated inside, and close to the surface of, a very high index nano-object that is embedded in a low index environment. A distribution in LDOS can arise from the size distribution of nanodiamonds and from the fact that different NV centers have different dipole-moment orientation and positions within the crystals [53, 56]. Here we assess if this LDOS hypothesis is quantitatively reasonable. Considering that the radiative decay rate $\gamma_{\text{r}}(\rho)$ is proportional to LDOS, we evaluate the $\gamma_{\text{r}}(\rho)$ distribution by calculating the LDOS distribution assuming spherical

nanoparticles, for which the LDOS is analytically known [65, 66]. Figure 2.5 shows the calculated LDOS map of diamond spheres as function of normalized wavenumber ($2\pi R_{sphere}/\lambda$) and dipole position in the sphere (r/R_{sphere}) for dipoles oriented normal (a) and tangential (b) to the surface of the sphere. We set the dielectric constant of the spheres equal to the bulk diamond value ($\varepsilon_{\text{sphere}} = 5.85$). For both dipole orientations, LDOS presents a set of resonances with a cut-off at around $2\pi R_{sphere}/\lambda = 1$ inside the sphere. For radially oriented dipoles (figure 2.5(a)), LDOS shows a discontinuity at the boundary of the sphere ($r/R_{sphere} = 1$) which is related to the discontinuity of the out-of-plane component of the electric field at the interface [67]. We modeled nanodiamond NV centers as point dipoles with randomly oriented dipole moments homogeneously distributed in position in the spheres. We furthermore take into account the distribution of particle size as specified according to the nanodiamond size-distribution histogram provided by the manufacturer. We make a histogram of the occurrence of LDOS values to find its probability distribution over all sphere sizes and dipole positions. We take into account the homogenous distribution of all dipole moment orientations by averaging over radial and tangential LDOS values as $\text{LDOS}_{\text{iso}} = \frac{1}{3}\text{LDOS}_{\perp} + \frac{2}{3}\text{LDOS}_{\parallel}$. We fix the wavelength at $\lambda = 680\,\text{nm}$ corresponding to the peak emission wavelength of our NV centers. The resulting LDOS distribution can be converted into a distribution directly comparable to experimentally measured decay rates by scaling the LDOS to the previously reported decay rate of $(11.6\ \text{ns})^{-1} \approx 0.086\,\text{ns}^{-1}$ of NV centers in bulk diamond [23]. We note that this entire procedure involves no adjustable parameter or any fit to data. The final result is plotted in figure 2.4(c) as the solid line. The calculated histogram correctly predicts that emission is significantly decelerated compared to decay in bulk diamond, consistent with the fact that decay in small dielectric spheres is decelerated both compared to vacuum, and bulk dielectric. However, we observe that the calculated histogram peak falls at much lower decay rate than the experimentally measured histogram peak, with a discrepancy amounting to a factor of 3. A similar discrepancy between the calculated and experimentally measured decay rates of nanodiamond NV centers was recently reported for samples with a much wider size distribution, centered at much larger median size, measured by Inam et al [53]. We note that this discrepancy cannot be attributed to the fact that we have taken particle shape to be simply spherical, and that we have neglected the presence of a substrate. These effects cause only small changes in the expected decay rate histogram, as verified in FDTD simulations by Inam et al [53]. One might further argue that the occurrence of a degenerate in-plane dipole moment [62] could skew the histogram of expected decay rates towards higher values, if one assumes the dipole moment is free to diffuse prior to de-excitation. However, if we just make a histogram of the fastest rate instead of the average rate at each possible NV center position, the resulting histogram also does not lead to a consistent explanation (not shown). We conclude that LDOS variations in nanodiamond under the hypothesis of unit quantum efficiency and a bulk decay rate of $(11.6\ \text{ns})^{-1}$ do not explain the variation in measured decay rates.

2.3.4 LDOS argument beyond unit quantum efficiency

Inam et al proposed that although calculated and experimental absolute decay values are inconsistent on basis of LDOS theory and the bulk rate in diamond, the calculated and experimental results can be scaled onto each other. Indeed, if we scale the reference rate that sets the rate axis for the calculated histogram peak not by 11.6 ns (rate constant in bulk diamond [23]), but by a factor of 3 shorter, calculated and measured histogram coincide reasonably (figure 2.4(c) dotted line). Such a scaling would imply as hypothesis a unit quantum efficiency, together with an as yet hidden explanation that introduces a multiplicative correction factor in the calculated rate distribution.

A second hypothesis could be that no adjustment should be made of the bulk rate that enters the comparison, but that the quantum efficiency of NV centers, while unity in bulk, is not unity in nanocrystals. Indeed, an additive offset to the calculated histogram is introduced by nonradiative decay channels that do not occur for bulk diamond, but could occur for nanocrystals due to defects and the presence of large surface area that could contain quenching sites. So far, significant nonradiative decay was evidenced only for very small nanocrystals (5 nm [59]). A distribution of nonradiative rates around $\gamma_{\mathrm{nr}} = 0.15\,\mathrm{ns}^{-1}$ would shift the calculated histogram to the measured rates. The magnitude of the required γ_{nr} implies that quantum efficiencies should be around 30% to 50% for the slowest nanocrystals in the measured ensemble (assuming unit efficiency in bulk).

A third hypothesis could be that the assumption that the bulk rate is entirely radiative to start with, is incorrect, i.e. that the quantum efficiency of NV centers in bulk is significantly below unity contrary to common assumption. Assuming a bulk quantum efficiency of 70% instead of 100% would overlap the calculated histogram peak with the measured most frequent rate. However, this explanation would severely underestimate the width of the decay rate distribution unless a distribution of γ_{nr} is at play.

We conclude that LDOS variations in nanodiamond alone do not explain the variation in measured decay rates, and that a distribution of radiative and nonradiative decay constants must be at play for NV centers in nanodiamond. Furthermore we conclude that an actual experimental calibration of quantum efficiency of individual NV centers is highly desired, which we will return to in sections 3.2 and 3.3.1.

2.4 Statistics on small nanodiamonds

2.4.1 Brightness and $g^{(2)}(0)$

For experiments in which nanodiamonds are intended as probes of, or sources to be embedded in, nanophotonic environments, a size smaller than that of the 100 nm nanodiamonds would be advantageous, as smaller size implies higher spatial resolution and a lower perturbative effect on the modes of the nanophotonic system [68, 69]. Therefore, we repeated the brightness and decay rate statistical measurements for the 25 nm sample, i.e. the batch of crystals with median diameter 26 nm. For 25 nm

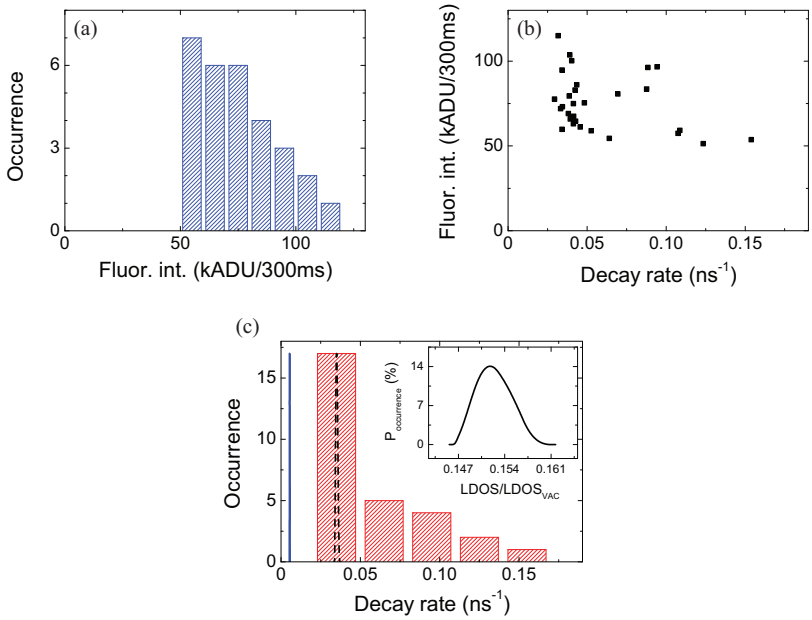

Figure 2.6: Statistics for 25 nm ND. (a) Histogram of fluorescence intensity (1 ADU on our CCD camera corresponds to approximately 6 detected photons). (b) Fluorescence intensity as a function of decay rate. (c) Bars: histogram of the measured decay rates of NV centers. Solid line: calculated distribution of $\mathrm{LDOS}/\mathrm{LDOS}_{vac}$ (shown in the inset) according to nanodiamonds size distribution, normalized to the rate of NV centers in bulk diamond. Dotted line: free scaling of the calculated LDOS distribution (solid line) so to match the experimental histogram (bars).

nanodiamonds, background-subtracted $g^{(2)}$ measurements show a zero dip for all identified NV centers (for a typical 25 nm nanodiamond $g^{(2)}$ see e.g. figure 2.3(c)). The fact that we found no nanodiamonds with multiple NV centers for this sample is commensurate with the smaller average crystal size. For these single NV centers, figure 2.6(a) shows a histogram of the fluorescence intensities measured on the CCD using CW illumination at 1 mW/μm^2. As in the case of the 100 nm sample, the histogram exhibits a wide fluorescence intensity distribution, in this case spanning a factor of about two. The most frequent brightness is approximately a factor two below that of the 100 nm sample.

2.4.2 Distribution of rates

As in the case of the 100 nm nanocrystals, we have also measured the decay rate for all 25 nm nanocrystals that we identified. The decay rate distribution, plotted as a histogram in figure 2.6(c), again shows a very wide distribution, with a factor of 4 contrast in decay rate. We find higher decay rates on average compared to 100 nm

nanodiamonds, with a most frequent decay rate around $\gamma_{tot} = 0.035\,ns^{-1}$ (corresponding to about 28 ns). The most frequent decay rate is approximately 25% faster than for the 100 nm nanodiamonds. Exactly as in the case of 100 nm nanodiamonds, the wide distribution of fluorescence brightness and decay rates does not imply a correlation between the two. As confirmation, in figure 2.6(b) we plot the fluorescence intensities and decay rates of 25 nm diamond NV centers, where we find no clear correlation.

2.4.3 Comparison to LDOS argument for distribution of rates

To assess whether the common hypothesis that the distribution in rate is due to a distribution in LDOS is valid for small nanodiamonds, we calculated the LDOS distribution (plotted in the inset of figure 2.6(c)) also for the 25 nm sample taking into account the size distribution histogram measured by the nanodiamond supplier. The rate distribution expected from the calculated LDOS scaled with the bulk rate (solid line in figure 2.6(c)) is, first, considerably narrower than the experimental decay rate distribution, and second, at considerably reduced rate compared to the measured decay rates. The magnitude of the discrepancy in decay rate is approximately a factor 6, i.e. twice larger than for the 100 nm nanodiamonds. A scaling of the calculated distribution by a multiplicative factor (here a factor of about 6) as proposed by Inam et al [53] does not lead to a good correspondence as in the 100 nm case, as the relative width of the measured histogram far exceeds that of the scaled calculation (dotted line in figure 2.6(c)). Taking our data on both 100 nm and 25 nm nanodiamonds together, we hence do not find support for the hypothesis by Inam et al that a hitherto hidden effect multiplies the radiative rate of NV centers in nanocrystals compared to bulk diamond. A more likely explanation that does not involve a scaling of γ_r due to an unknown origin is that NV centers are subject to a distribution of nonradiative rates on top of the LDOS-induced radiative rate distribution. The measured distribution of 25 nm nanodiamond decay rates points at a wide distribution of nonradiative rates. According to this hypothesis, those crystals with decay around the most-frequent decay rate of $0.035\,ns^{-1}$ must have a quantum efficiency below 15-20%, twice lower than for the 100 nm nanocrystals. The overall lower quantum efficiency estimate is commensurate with the reduction in average brightness, and is also consistent with the fact that a larger sensitivity to nonradiative decay channels is potentially associated with the increased nanocrystal surface-to-volume ratio.

2.5 Conclusions and outlook

In conclusion, we have investigated the brightness and decay rate of single NV centers in nanodiamonds of 25 nm, and of 100 nm median size and studied the brightness and rate distribution and their correlation. For both size ranges a wide distribution in brightnesses and rates is found, consistent with reports by earlier workers. Based on the absence of strong correlation between the measured fluorescence intensity and decay rate of NV centers, we conclude that the quantum efficiency of NV centers

in nanodiamonds is distributed and not equal to unity. In addition, we presented the results of our LDOS-based analytical model for rate distribution of NV centers in nanodiamonds with different sizes. Comparing the analytical results and the measured data, we conclude that the wide distribution of rates is due to a distribution in both radiative and nonradiative rates and therefore the quantum efficiencies of nanodiamond NV centers. This conclusion contradicts earlier work, that interpreted the wide distribution of decay rates as mainly due to a photonic effect that causes a distribution in radiative decay rates via the LDOS.

The fact that the quantum efficiency of nanodiamond NV centers does not correlate with at-hand properties like spectrum or brightness, stands out critically where nanodiamond NV centers are intended to be used as efficient fluorescent sources or LDOS probes in nanophotonic experiments. In other words, screening nanodiamonds to pick the best one to probe LDOS or for incorporation in a photonic device can not rely on a simple metric such as spectrum or brightness. Instead, we argue that future work in the hybrid assembly of nanodiamonds in plasmonics and photonic crystals to realize accelerated spontaneous emission decay always requires an experimental protocol in which nanodiamonds are first individually calibrated in terms of quantum efficiency. Such experimental protocols will be presented in the next chapter where we show, for the first time, the results of quantum efficiency measurements of individual nanodiamond NV centers.

References

[1] C. Santori, D. Fattal, and Y. Yamamoto, *Single-photon devices and applications*, John Wiley & Sons, 2010.

[2] K. Vahala, *Optical microcavities*, volume 5 of *Advanced series in applied physics*, World Scientific, 2004.

[3] J. Bleuse, J. Claudon, M. Creasey, N. S. Malik, J.-M. Gérard, I. Maksymov, J.-P. Hugonin, and P. Lalanne, *Inhibition, enhancement, and control of spontaneous emission in photonic nanowires*, Phys. Rev. Lett. **106**, 103601 (2011).

[4] J.-M. Gerard and B. Gayral, *Strong purcell effect for inas quantum boxes in three-dimensional solid-state microcavities*, J. Lightwave Technol. **17**, 2089 (1999).

[5] J. P. Reithmaier, G. Sek, A. Löffler, C. Hofmann, S. Kuhn, S. Reitzenstein, L. V. Keldysh, V. D. Kulakovskii, T. L. Reinecke, and A. Forchel, *Strong coupling in a single quantum dot-semiconductor microcavity system*, Nature **432**, 197 (2004).

[6] T. Yoshie, A. Scherer, J. Hendrickson, G. Khitrova, H. M. Gibbs, G. Rupper, C. Ell, O. B. Shchekin, and D. G. Deppe, *Vacuum Rabi splitting with a single quantum dot in a photonic crystal nanocavity*, Nature **432**, 200 (2004).

[7] D. Englund, D. Fattal, E. Waks, G. Solomon, B. Zhang, T. Nakaoka, Y. Arakawa, Y. Yamamoto, and J. Vučković, *Controlling the spontaneous emission rate of single quantum dots in a two-dimensional photonic crystal*, Phys. Rev. Lett. **95**, 013904 (2005).

[8] S. Noda, M. Fujita, and T. Asano, *Spontaneous-emission control by photonic crystals and nanocavities*, Nature Photon. **1**, 449 (2007).

[9] P. Yao, V. Manga Rao, and S. Hughes, *On-chip single photon sources using planar photonic crystals and single quantum dots*, Laser & Photon. Rev. **4**, 499 (2010).

[10] H. Thyrrestrup, L. Sapienza, and P. Lodahl, *Extraction of the β-factor for single quantum dots coupled to a photonic crystal waveguide*, Appl. Phys. Lett. **96**, 231106 (2010).

[11] L. Sapienza, H. Thyrrestrup, S. Stobbe, P. D. Garcia, S. Smolka, and P. Lodahl, *Cavity quantum electrodynamics with anderson-localized modes*, Science **327**, 1352 (2010).

[12] A. V. Akimov, A. Mukherjee, C. L. Yu, D. E. Chang, A. S. Zibrov, P. R. Hemmer, H. Park, and M. D. Lukin, *Generation of single optical plasmons in metallic nanowires coupled to quantum dots*, Nature **450**, 402 (2007).

[13] R.-M. Ma, R. F. Oulton, V. J. Sorger, G. Bartal, and X. Zhang, *Room-temperature sub-diffraction-limited plasmon laser by total internal reflection*, Nat. Mater. **10**, 110 (2011).

[14] A. F. Koenderink, *Plasmon nanoparticle array waveguides for single photon and single plasmon sources*, Nano Lett. **9**, 4228 (2009).

[15] A. G. Curto, G. Volpe, T. H. Taminiau, M. P. Kreuzer, R. Quidant, and van Hulst, Niek F, *Unidirectional emission of a quantum dot coupled to a nanoantenna*, Science **329**, 930 (2010).

[16] R. Sprik, B. A. van Tiggelen, and A. Lagendijk, *Optical emission in periodic dielectrics*, Europhys. Lett. **35**, 265 (1996).

[17] L. Novotny and B. Hecht, *Principles of nano-optics*, Cambridge University Press, 2006.

[18] B. Lounis and M. Orrit, *Single-photon sources*, Rep. Prog. Phys. **68**, 1129 (2005).

[19] C. A. Leatherdale, W.-K. Woo, F. V. Mikulec, and M. G. Bawendi, *On the absorption cross section of CdSe nanocrystal quantum dots*, J. Phys. Chem. B **106**, 7619 (2002).

[20] C. de Mello Donegá, S. G. Hickey, S. F. Wuister, D. Vanmaekelbergh, and A. Meijerink, *Single-step synthesis to control the photoluminescence quantum yield and size dispersion of CdSe nanocrystals*, J. Phys. Chem. B **107**, 489 (2003).

[21] R. Brouri, A. Beveratos, J.-P. Poizat, and P. Grangier, *Photon antibunching in the fluorescence of individual color centers in diamond*, Opt. Lett. **25**, 1294 (2000).

[22] C. Kurtsiefer, S. Mayer, P. Zarda, and H. Weinfurter, *Stable solid-state source of single photons*, Phys. Rev. Lett. **85**, 290 (2000).

[23] A. Beveratos, R. Brouri, T. Gacoin, J.-P. Poizat, and P. Grangier, *Nonclassical radiation from diamond nanocrystals*, Phys. Rev. A **64**, 061802 (2001).

[24] van der Sar, T, Z. H. Wang, M. S. Blok, H. Bernien, T. H. Taminiau, D. M. Toyli, D. A. Lidar, D. D. Awschalom, R. Hanson, and V. V. Dobrovitski, *Decoherence-protected quantum gates for a hybrid solid-state spin register*, Nature **484**, 82 (2012).

[25] L. Robledo, L. Childress, H. Bernien, B. Hensen, Alkemade, Paul F A, and R. Hanson, *High-fidelity projective read-out of a solid-state spin quantum register*, Nature **477**, 574 (2011).

[26] J. R. Maze, P. L. Stanwix, J. S. Hodges, S. Hong, J. M. Taylor, P. Cappellaro, L. Jiang, Dutt, M V Gurudev, E. Togan, A. S. Zibrov, A. Yacoby, R. L. Walsworth, and M. D. Lukin, *Nanoscale magnetic sensing with an individual electronic spin in diamond*, Nature **455**, 644 (2008).

[27] V. R. Horowitz, B. J. Alemán, D. J. Christle, A. N. Cleland, and D. D. Awschalom, *Electron spin resonance of nitrogen-vacancy centers in optically trapped nanodiamonds*, Proc. Natl. Acad. Sci. U.S.A. **109**, 13493 (2012).

[28] J. Tisler, G. Balasubramanian, B. Naydenov, R. Kolesov, B. Grotz, R. Reuter, J.-P. Boudou, P. A. Curmi, M. Sennour, A. Thorel, M. Börsch, K. Aulenbacher, R. Erdmann, P. R. Hemmer, F. Jelezko, and J. Wrachtrup, *Fluorescence and spin properties of defects in single digit nanodiamonds*, ACS Nano **3**, 1959 (2009).

[29] A. Faraon, C. Santori, Z. Huang, V. M. Acosta, and R. G. Beausoleil, *Coupling of nitrogen-vacancy centers to photonic crystal cavities in monocrystalline diamond*, Phys. Rev. Lett. **109**, 033604 (2012).

[30] C. Santori, P. E. Barclay, K.-M. C. Fu, R. G. Beausoleil, S. Spillane, and M. Fisch, *Nanophotonics for quantum optics using nitrogen-vacancy centers in diamond*, Nanotechnology **21**, 274008 (2010).

[31] T. M. Babinec, Hausmann, Birgit J M, M. Khan, Y. Zhang, J. R. Maze, P. R. Hemmer, and M. Loncar, *A diamond nanowire single-photon source*, Nat. Nanotechnol. **5**, 195 (2010).

[32] T. Schröder, F. Gädeke, M. J. Banholzer, and O. Benson, *Ultrabright and efficient single-photon generation based on nitrogen-vacancy centres in nanodiamonds on a solid immersion lens*, New J. Phys. **13**, 055017 (2011).

[33] K.-M. C. Fu, P. E. Barclay, C. Santori, A. Faraon, and R. G. Beausoleil, *Low-temperature tapered-fiber probing of diamond nitrogen-vacancy ensembles coupled to gap microcavities*,

New J. Phys. **13**, 055023 (2011).

[34] A. Faraon, P. E. Barclay, C. Santori, K.-M. C. Fu, and R. G. Beausoleil, *Resonant enhancement of the zero-phonon emission from a colour centre in a diamond cavity*, Nature Photon. **5**, 301 (2011).

[35] O. Benson, *Assembly of hybrid photonic architectures from nanophotonic constituents*, Nature **480**, 193 (2011).

[36] S. Schietinger, M. Barth, T. Aichele, and O. Benson, *Plasmon-enhanced single photon emission from a nanoassembled metal-diamond hybrid structure at room temperature*, Nano Lett. **9**, 1694 (2009).

[37] T. van der Sar, J. Hagemeier, W. Pfaff, E. C. Heeres, S. M. Thon, H. Kim, P. M. Petroff, T. H. Oosterkamp, D. Bouwmeester, and R. Hanson, *Deterministic nanoassembly of a coupled quantum emitter–photonic crystal cavity system*, Appl. Phys. Lett. **98**, 193103 (2011).

[38] R. Kolesov, B. Grotz, G. Balasubramanian, R. J. Stöhr, A. A. L. Nicolet, P. R. Hemmer, F. Jelezko, and J. Wrachtrup, *Wave–particle duality of single surface plasmon polaritons*, Nature Phys. **5**, 470 (2009).

[39] A. Huck, S. Kumar, A. Shakoor, and U. L. Andersen, *Controlled coupling of a single nitrogen-vacancy center to a silver nanowire*, Phys. Rev. Lett. **106**, 096801 (2011).

[40] Michaelis, Hettich, Mlynek, and Sandoghdar, *Optical microscopy using a single-molecule light source*, Nature **405**, 325 (2000).

[41] A. Cuche, A. Drezet, Y. Sonnefraud, O. Faklaris, F. Treussart, J.-F. Roch, and S. Huant, *Near-field optical microscopy with a nanodiamond-based single-photon tip*, Opt. Express **17**, 19969 (2009).

[42] A. Cuche, O. Mollet, A. Drezet, and S. Huant, *"deterministic" quantum plasmonics*, Nano Lett. **10**, 4566 (2010).

[43] M. Frimmer, Y. Chen, and A. F. Koenderink, *Scanning emitter lifetime imaging microscopy for spontaneous emission control*, Phys. Rev. Lett. **107**, 123602 (2011).

[44] J. Tisler, T. Oeckinghaus, R. J. Stoehr, R. Kolesov, R. Reuter, F. Reinhard, and J. Wrachtrup, *Single defect center scanning near-field optical microscopy on graphene*, Nano Lett. **13**, 3152 (2013).

[45] R. Beams, D. Smith, T. W. Johnson, S.-H. Oh, L. Novotny, and A. N. Vamivakas, *Nanoscale fluorescence lifetime imaging of an optical antenna with a single diamond NV center*, Nano Lett. **13**, 3807 (2013).

[46] A. W. Schell, P. Engel, J. F. M. Werra, C. Wolff, K. Busch, and O. Benson, *Scanning single quantum emitter fluorescence lifetime imaging: Quantitative analysis of the local density of photonic states*, Nano Lett. **14**, 2623 (2014).

[47] L. Rondin, J.-P. Tetienne, T. Hingant, J.-F. Roch, P. Maletinsky, and V. Jacques, *Magnetometry with nitrogen-vacancy defects in diamond*, Rep. Prog. Phys. **77**, 056503 (2014).

[48] C. L. Degen, *Scanning magnetic field microscope with a diamond single-spin sensor*, Appl. Phys. Lett. **92**, 243111 (2008).

[49] J. M. Taylor, P. Cappellaro, L. Childress, L. Jiang, D. Budker, P. R. Hemmer, A. Yacoby, R. Walsworth, and M. D. Lukin, *High-sensitivity diamond magnetometer with nanoscale resolution*, Nat. Phys. **4**, 810 (2008).

[50] G. Balasubramanian, I. Y. Chan, R. Kolesov, M. Al-Hmoud, J. Tisler, C. Shin, C. Kim, A. Wojcik, P. R. Hemmer, A. Krueger, T. Hanke, A. Leitenstorfer, R. Bratschitsch, F. Jelezko, and J. Wrachtrup, *Nanoscale imaging magnetometry with diamond spins under ambient conditions*, Nature **455**, 648 (2008).

[51] P. Maletinsky, S. Hong, M. S. Grinolds, B. Hausmann, M. D. Lukin, R. L. Walsworth, M. Loncar, and A. Yacoby, *A robust scanning diamond sensor for nanoscale imaging with single nitrogen-vacancy centres*, Nat. Nanotechnol. **7**, 320 (2012).

[52] C. Bradac, T. Gaebel, N. Naidoo, J. R. Rabeau, and A. S. Barnard, *Prediction and measurement of the size-dependent stability of fluorescence in diamond over the entire nanoscale*, Nano Lett. **9**, 3555 (2009).

[53] F. A. Inam, T. Gaebel, C. Bradac, L. Stewart, M. J. Withford, J. M. Dawes, J. R. Rabeau, and M. J. Steel, *Modification of spontaneous emission from nanodiamond colour centres on a structured surface*, New J. Phys. **13**, 073012 (2011).

[54] L. H. G. Tizei and M. Kociak, *Spectrally and spatially resolved cathodoluminescence of nanodiamonds: local variations of the NV^0 emission properties*, Nanotechnology **23**, 175702 (2012).

[55] P. V. Ruijgrok, R. Wüest, A. A. Rebane, A. Renn, and V. Sandoghdar, *Spontaneous emission of a nanoscopic emitter in a strongly scattering disordered medium*, Opt. Express **18**, 6360 (2010).

[56] H. Schniepp and V. Sandoghdar, *Spontaneous emission of europium ions embedded in dielectric nanospheres*, Phys. Rev. Lett. **89**, 257403 (2002).

[57] F. Jelezko and J. Wrachtrup, *Single defect centres in diamond: A review*, Phys. Stat. Sol. (a) **203**, 3207 (2006).

[58] S. Schietinger, *private communication*.

[59] C. Bradac, T. Gaebel, N. Naidoo, M. J. Sellars, J. Twamley, L. J. Brown, A. S. Barnard, T. Plakhotnik, A. V. Zvyagin, and J. R. Rabeau, *Observation and control of blinking nitrogen-vacancy centres in discrete nanodiamonds*, Nat. Nanotechnol. **5**, 345 (2010).

[60] S. Schietinger, T. Schröder, and O. Benson, *One-by-one coupling of single defect centers in nanodiamonds to high-q modes of an optical microresonator*, Nano Lett. **8**, 3911 (2008).

[61] R. Chapman and T. Plakhotnik, *Quantitative luminescence microscopy on nitrogen-vacancy centres in diamond: Saturation effects under pulsed excitation*, Chem. Phys. Lett. **507**, 190 (2011).

[62] Alegre, Thiago P. Mayer, C. Santori, G. Medeiros-Ribeiro, and R. G. Beausoleil, *Polarization-selective excitation of nitrogen vacancy centers in diamond*, Phys. Rev. B **76**, 165205 (2007).

[63] L. Robledo, H. Bernien, T. van der Sar, and R. Hanson, *Spin dynamics in the optical cycle of single nitrogen-vacancy centres in diamond*, New J. Phys. **13**, 025013 (2011).

[64] T. Plakhotnik, W. Moerner, V. Palm, and U. P. Wild, *Single molecule spectroscopy: maximum emission rate and saturation intensity*, Opt. Commun. **114**, 83 (1995).

[65] C.-T. Tai, *Dyadic Green functions in electromagnetic theory*, volume 272, IEEE press New York, 1994.

[66] H. Mertens, A. F. Koenderink, and A. Polman, *Plasmon-enhanced luminescence near noble-metal nanospheres: Comparison of exact theory and an improved Gersten and Nitzan model*, Phys. Rev. B **76**, 115123 (2007).

[67] H. Urbach and G. Rikken, *Spontaneous emission from a dielectric slab*, Phys. Rev. A **57**, 3913 (1998).

[68] A. F. Koenderink, M. Kafesaki, B. C. Buchler, and V. Sandoghdar, *Controlling the resonance of a photonic crystal microcavity by a near-field probe*, Phys. Rev. Lett. **95**, 153904 (2005).

[69] T. van der Sar, J. Hagemeier, W. Pfaff, E. Heeres, S. Thon, H. Kim, P. Petroff, O. Tjerk, D. Bouwmeester, and R. Hanson, *Effect of a nanoparticle on the optical properties of a photonic crystal cavity: theory and experiment*, J. Opt. Soc. Am. B **29**, 698 (2012).

3

Quantum efficiency measurement of single nanodiamond NV centers

We apply two techniques on single nanodiamond NV centers to calibrate their quantum efficiency by varying the local density of optical states at the position of the emitters. In the first technique, the local density of states (LDOS) variations are induced at a dielectric interface by using liquids to vary the refractive index. By applying this technique on nanodiamond NV centers we find that in 25 nm nanodiamonds, NV centers are essentially insensitive to the LDOS variations imposed by liquids with different refractive indices, and propose that quantum efficiencies in such nanocrystals are widely distributed between 0% and 20%. In the second technique, we nanomechanically vary the distance between a fluorescent source and a mirror, thereby varying the local density of optical states at the source position. Application of this technique to NV defects in diamond nanocrystals shows that their quantum yield can significantly differ from unity. For single NV centers in larger 100 nm nanocrystals, we show that decay rate changes can be reversibly induced by nanomechanically approaching a mirror to change the LDOS. Using this scanning mirror method, for the first time we report calibrated quantum efficiencies of NV centers, and show that different but nominally identical nanocrystals have widely distributed quantum efficiencies between 10% and 90%.

3.1 Introduction

Due to the photostability properties of nanodiamond NV centers, these emitters are generally regarded as efficient fluorescent sources that are suitable for use as LDOS probes for integration in nanophotonic devices. However, according to chapter 2, our data indicate that NV centers even in nanocrystals as large as 100 nm across do not have unit quantum efficiency, and that there is a distribution of nonradiative and radiative rates. The general opinion in literature that NV centers must be efficient emitters is evident from several reports that claim lifetime changes for NV centers that are induced by placing nanocrystals in photonic environments of varying index and topology [1–5]. However, to our knowledge all these measurements of lifetime changes for nanodiamonds were performed by comparing the *mean rate* from an ensemble of single-center measurements in one system, to measurement on a different ensemble of single-centers in a second system [2, 4, 5]. Ruijgrok *et al.* [4] in particular report changes for a system in which the induced LDOS change is exactly known, and report changes in the *mean* rate consistent with those expected for unit-quantum-efficiency emitters. However, we note that in these ensemble measurements, the change of the *mean* decay rate was far smaller than the width of the rate distribution. Therefore, those measurements do not allow to ascertain whether for *any given* single NV center the rate actually varies with varying LDOS in a manner that is consistent with the expectations for efficient emitters. Therefore, it is crucial to measure quantum efficiency, radiative and nonradiative decay rates independently on individual NV centers in order to decide if /which NV centers in nanodiamonds are suitable for use as LDOS probes for integration in nanophotonic devices.

Several methods have been proposed so far for measuring the quantum efficiency of emitters. These methods are based on exposing the emitters to a known LDOS variation while measuring the decay rate from which the quantum efficiency can be extracted [6–8] as explained earlier in chapter 1. A realization of this method using liquids with different refractive indices to induce LDOS variations was pioneered by Snoeks et al [9], and later adopted by e.g. Refs. [4, 10, 11]. As an alternative, Buchler *et al.* pioneered a micromechanical method to vary LDOS by approaching a mirror to a single molecule. Similarly, Chizhik *et al.* made use of a nanomechanically tunable cavity [8]. Here we use similar methods to systematically induce variations in the LDOS experienced by individual nanodiamond NV centers.

In this chapter, we first present the results of experiments in which we measure emission rate changes of individual nanodiamonds as we controllably vary the LDOS of their environment using liquids of different refractive indices. As discussed in chapter 2, for small nanocrystals there is a decay rate distribution indicative of low-quantum-efficiency emitters. Consistent with this low quantum efficiency, using the LDOS tuning method with liquids, we find no evidence that small single NV centers are responsive LDOS probes when applying moderate LDOS variations.

Next, using a variation of the nanomechanical technique of Buchler et al. [6] we effect a Drexhage experiment [7, 12–15] to calibrate decay constants of single NV centers [16]. As in Ref. [16] we use a spherical silver mirror of several 10 μm

in diameter attached to a scanning probe. The technique relies on the shear-force mechanism to keep the mirror in near-contact with the sample and a lateral scanning procedure. We calibrate our technique on colloidal beads infiltrated with high-quantum-yield dye and on thin emissive layers. Finally, we measure the quantum efficiency of single NV centers in diamond nanocrystals. For the larger nanocrystals (100 nm diameter), we for the first time manage to induce reversible changes of up to 25% in the total decay rate of single NV centers using a calibrated LDOS change induced by a nanomechanically moved mirror. On basis of these measurements we argue that the apparent quantum efficiency of nanodiamonds in the size range 50–150 nm ranges widely from about 10% to 90%. This wide range of quantum efficiencies implies that prior to constructing a photonic structure, it is necessary to screen the nanocrystals using a calibrated quantum efficiency measurement on the single NV center level, as shown in this chapter.

The chapter is structured as follows. In section 3.2 we present the results of LDOS tuning on small nanodiamond NV centers using liquids with different refractive indices. Next, in section 3.3 we apply the technique of nanomechanical tuning of LDOS on, first, fluorescing beads and dye layers (section 3.4), and then, on large nanodiamonds containing single NV centers (section 3.3.1). Finally, we conclude our findings in section 3.4 where we give an outlook for further possible studies.

3.2 Liquid tuning of LDOS on single NV centers in small nanodiamonds

For the small nanodiamonds only the liquid tuning method could be applied due to experimental constraints. Sources are placed in close proximity to a planar interface between a dielectric and a half-space that can be filled with liquids of different refractive index. The advantage of using liquid tuning of refractive index for sources near an interface is that the LDOS changes near an interface are nearly independent of emission frequency, and are known to be excellently described by the theory explained in full by Urbach and Rikken [17]. In view of the broad emission spectrum of NV centers in diamond, it is important to apply a broadband LDOS change when seeking to measure lifetime changes. A narrowband LDOS variation as obtained with a high-Q microcavity that would for instance be tuned to the zero phonon line, would not necessarily affect the rate, but rather only the branching ratio between the zero phonon line and the rest of the spectrum.

We prepared the sample by evaporating a 60 nm thick layer of SiO_2 on one of the 25 nm nanodiamond samples on which we had identified single NV centers as discussed in chapter 2. This step immobilizes the nanodiamonds, and ensures that liquid application to tune LDOS does not add new chemically induced nonradiative decay channels. Next, we defined a 3 mm deep liquid reservoir on top of the sample using a ring-shaped enclosure cut from Polydimethylsiloxane (PDMS) bonded to the substrate. Figure 3.1(a) depicts a schematic of the sample. In order to investigate the decay dynamics of the NV centers in response to the LDOS variations, we randomly

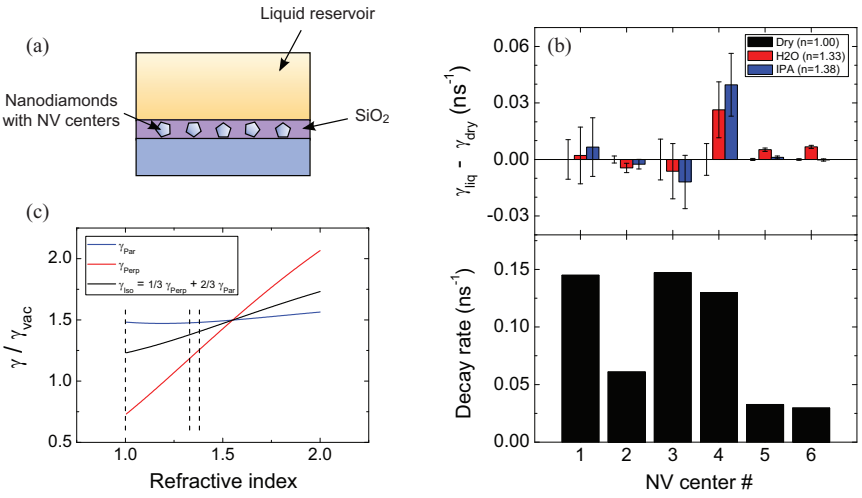

Figure 3.1: (a) Schematic of the sample used for liquid LDOS tuning experiment. (b) Lower panel: decay rates of six randomly chosen NV centers. Upper panel: decay rate changes of each NV center after addition of liquids. (c) Calculated decay rate variations of a dipole embedded at the center of a three layer system as a function of the refractive index of the top layer for different dipole-moment orientations. Dashed lines indicate the refractive indices of air, water and IPA used in the experiment.

selected six NV centers from the ensemble of figure 4.3 and measured their lifetimes in three conditions: before adding any liquids where the top half space of nanodiamonds consists of air ($n = 1.00$), after adding water with refractive index of $n = 1.33$, and after adding isopropyl alcohol (IPA) with refractive index of $n = 1.38$ to the liquid bath on top of the nanodiamonds. In the lower panel of figure 3.1(b) we plot the decay rate of each NV center as a black bar measured when the sample is dry. The color bars in the upper panel of figure 3.1(b) show the difference between decay rates of each NV center after and before introducing a liquid. We observe that for most centers, the decay rate either barely varies, or varies non-monotonically with applied index, although generally, one expects to observe an increase in the decay rate of a dipole emitter in a homogenous medium by increasing the refractive index of the environment due to an increase of the LDOS [17].

For comparison to the data we calculate the normalized decay rate of a dipole positioned in the middle of a 60 nm thick SiO_2 slab ($n = 1.52$) which is sandwiched between a semi-infinite slab of quartz with $n = 1.46$ at the bottom and a semi-infinite slab with varying refractive index at the top. Figure 3.1(c) shows the calculated decay rate of the dipole as a function of the refractive index of the top layer for different dipole-moment orientations. The calculation shows that as the refractive index increases the decay rate change is expected to be monotonic and increasing and is the largest for a dipole oriented perpendicular to the interface while the change is slight for a

dipole-moment parallel to the interface. Comparing the calculated rate changes to the measured decay rates (figure 3.1(b)), we find no systematic rate variation for the NV centers within the error bars of our experimental data. The error bar for measurements on individual NV centers is composed of two contributions. First, the error bar contains the uncertainty in the fit to the fluorescence decay trace. Second, the experiment is hampered by the fact that the decay rates of some of the single nanodiamonds was observed to jump slightly between observations, even if no change in environment was applied. These jumps amount to approximately 5%, and occur on time scales of hours to days. To exclude this effect, we have measured the rate for each liquid and a reference in air on the same day for each NV center to generate the plot of rate changes in figure 3.1(b).

We find that there is no evidence that the rate of *individual* NV centers in 25 nm diamond nanocrystals actually varies in accordance with the known applied LDOS changes. This observation appears to be at variance with earlier work that evidenced a small change in the mean decay rate of an ensemble of NV centers in a liquid-tuning experiment [4]. As two caveats, we note that first, in that previous work it was not verified if any such change occurred for each source individually, and second, that a shortcoming of our experiment for quantititave interpretation is that for dipoles located close to an interface (as is the case here), the decay rate enhancement significantly depends on the unknown dipole-moment orientation of the emitter with respect to the interface. While the fact that we do not know the dipole orientations for each NV center makes it impossible to conclude with certainty that an LDOS effect is absent, two hypotheses for absence of an LDOS effect could be proposed. First, that the quantum efficiency of 25 nm diamond nanocrystals is low, or second, that the very high index diamond shell around the NV centers intrinsically prevents the NV center from responding to (moderate) changes in the LDOS of the environment it is supposed to probe. We exclude the latter explanation on basis of a set of finite element (COMSOL) simulations, in which we calculate the decay rate of a point dipole randomly located in a diamond nanosphere, which in turn is placed at varying distances from a planar interface with materials of various dielectric constants. We find that in all cases, the decay rate of the source simply follows the theory of Urbach and Rikken [17] for a source without dielectric shell, multiplied by a pre-factor that is essentially a quasistatic local field correction factor due to the diamond shell and is independent of the varying LDOS.

To conclude, our observation that no NV center responds to LDOS changes together with our earlier correlation plots of brightness versus decay rate (figures 4.2 and 4.3) means that the quantum efficiencies of 25 nm diamond nanocrystals are likely low. A second important conclusion is that single NV centers of 25 nm size appear unsuitable to measure LDOS changes due to the slight jumps in lifetime, unless the entire measurement scheme (including reference measurements) takes less than a few hours.

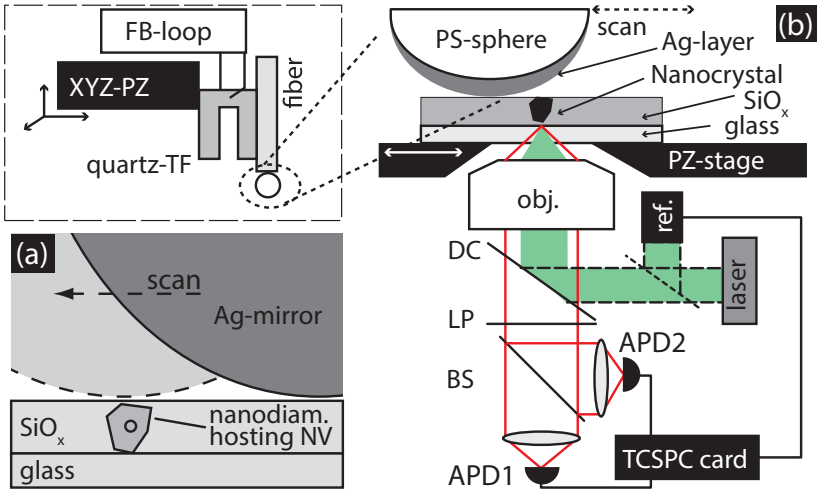

Figure 3.2: (a) Experimental principle: The distance between an emitter and a mirror is varied by laterally scanning a spherical mirror over the sample. (b) Sketch of experimental setup. The sample lies on a piezo stage with the micromirror located above. The mirror is attached to an optical fiber glued to a quartz tuning fork, which is positioned with an xyz-piezo scanner [see inset]. Below the sample a microscope objective focuses the pump laser on the emitter. Fluorescence is filtered by a dichroic beamsplitter (DC) and long-pass filter (LP) before it is guided to a Hanbury Brown-Twiss setup composed of a beamsplitter (BS) and two APDs.

3.3 The scanning-mirror method

In this section we report on the results of the nanomechanically varying LDOS method to assess if single NV centers are suited for LDOS measurements, and to calibrate emission rates. This method has the advantage that we can apply calibrated LDOS changes rapidly so that jumps in the intrinsic rate constants can be avoided that hamper experiments where macroscopic sample changes are required to modify LDOS, as in a liquid immersion experiment. The scheme is similar to a measurement procedure reported by Buchler et al [6], based on a Drexhage experiment [7, 12–15]. In a Drexhage experiment, a mirror is used to impose a large LDOS change, and rates are measured as a function of the emitter-mirror separation. While this method is usually implemented by creating a set of macroscopic samples where mirrors are coated with spacers of calibrated thicknesses [7, 13, 14] or by creating a single sloping wedge between a mirror and an ensemble of emitters [15], Buchler et al realized a nanomechanical version that can be applied to a single emitter. Buchler et al used a silver-coated curved fiber end as a mirror attached to a piezo-stage to precisely tune the mirror distance to an underlying single emitter on the sample [6]. Here, we use a similar method in a shear-force-feedback near-field microscope. However, instead of a vertical mirror displacement, we use a lateral displacement of the curved mirror while

staying in shear-force feedback to keep the mirror and sample substrate in near-contact. Our scheme of changing the distance between an emitter and a mirror is illustrated in Fig. 3.2(a). The interrogated source is fixed to a substrate and a large spherical mirror is laterally scanned across the sample surface while the mirror-sample distance is kept constant using shear-force feedback [18]. This procedure is implementable in most closed-loop scanning-probe microscopes, as opposed to calibrated retraction of the probe. In Fig. 3.2(a) two positions of the mirror with respect to an emitter are shown to illustrate the principle of changing the emitter-mirror distance by laterally moving the mirror over the sample. To fabricate the micromirror we glue polystyrene beads (diameter 45 µm, Polysciences Europe) to the cleaved end of an optical fiber with a small amount of super-glue. We subsequently evaporate a layer of 200 nm of Ag onto the sphere to obtain a spherical micromirror. The optical fiber is then glued to a quartz tuning fork, as sketched in Fig. 3.2(b, inset), which is mounted on a 3D piezo scanner, the z-axis of which is controlled through a standard shear-force feedback loop. In other words, the quartz fork is vibrated at a frequency just above its resonance using weak electric excitation, and the resultant phase response of the fork is used as input for a PID-loop that adjusts the z-piezo to approach the sample surface to within 5-15 nm. The scanning probe assembly is placed on top of the inverted confocal microscope described in chapter 2, allowing us to collect fluorescence intensity and fluorescence lifetime data as function of probe position. In particular this is achieved by fixing the sample in the confocal focus of the ps pulsed 532 nm laser, and scanning the probe sideways.

3.3.1 Nanomechanical tuning of LDOS on large nanodiamonds

We have applied the scanning-mirror LDOS changing technique to 100 nm nanodiamonds containing single NV centers, prepared as described in section 2.2.1, and subsequently embedded in a 200 nm thick layer of planarizing spin-on glass (FOX-14, Dow Corning). The spin-on glass immobilizes the nanocrystals, so that they are not moved during shear-force scanning. In order to vary the distance between the mirror and the emitter, we scan the mirror bead laterally on top of an identified NV center. For each position of the mirror bead, we collect the fluorescence emission of the NV center, positioned at the focus of the pump laser, through the confocal microscope setup described in section 2.2.2. By scanning the mirror bead, we obtain a confocal fluorescence intensity map as shown in figure 3.3(a). Here, each pixel represents the relative position of the mirror bead with respect to the NV center with the false color representing the collected fluorescence intensity. We clearly observe interference rings in the fluorescence intensity map. These rings mainly stem from the fact that the mirror imposes a standing-wave pattern on the 532 nm pump field, which subsequently results in a modulation of the fluorescence intensity.

For each pixel in the fluorescence intensity map, we stored absolute photon arrival times, as well as laser pulse arrival times, allowing us to extract the decay dynamics. We use a single-exponential fit to obtain the corresponding decay rate of the emitter for each mirror position, as plotted in figure 3.3(b). Here, the color scale represents the

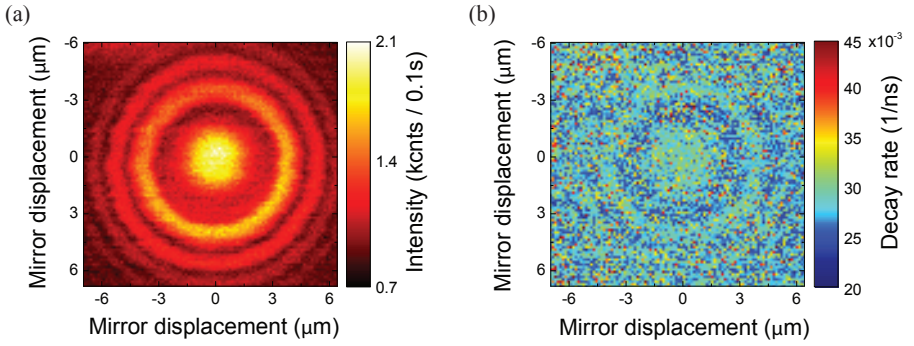

Figure 3.3: (a) Fluorescence intensity map of an NV center (NV center 1 in table 3.1) as a function of mirror lateral displacement (b) Corresponding decay rate map of the NV center as a function of mirror lateral displacement. Decay rates are extracted from a single-exponential fit to the time-trace data for each pixel.

fitted decay rate corresponding to a defined mirror position. Interestingly, we observe a radial modulation of the decay rates varying between about $0.02\,\mathrm{ns}^{-1}$ to $0.04\,\mathrm{ns}^{-1}$, which we attribute to the varying LDOS in front of the mirror. To quantify the variation as a function of the distance from emitter to mirror, we extracted the decay rates as a function of the lateral distance to the mirror central position. To this end, we bin pixels in concentric rings of equal lateral distance to the mirror center, and concatenate the photon-correlation time traces of all pixels in each bin to obtain a single fluorescence decay trace per radial distance. Using the spherical form factor of the bead, we convert lateral position of the mirror to normal distance of the mirror to emitter. The decay rate fitted to the fluorescence decay for each mirror-emitter separation is depicted in figure 3.4 (black dots). We observe a distinct oscillation of the rate around $0.028\,\mathrm{ns}^{-1}$, with a 15% amplitude. To our knowledge, this is the first report of a reversible change in the decay rate of a single NV center in a calibrated LDOS experiment.

Due to the large radius of the mirror compared to its distance to emitters, it is reasonable to consider the experimental configuration as a planar glass-air-mirror system in which we vary the air thickness. For this system, the LDOS is exactly known [14, 18] for any dipole orientation and position. The LDOS is calculated according to the formalism of Amos and Barnes [14], which essentially expresses the required imaginary part of the Green function at the source position as a Sommerfeld integral over all parallel wave vectors. In particular, the local density of states normalized to that in vacuum differs for the case of dipole orientation parallel and perpendicular to the interface, taking on the values

$$\rho_{\perp}(z) = \frac{3}{2}\mathrm{Im}\int_0^{\infty}[1 - r^p(\kappa_{||}, z)e^{-2ik_z h}]\frac{i\kappa_{||}^3 d\kappa_{||}}{\kappa_z}$$

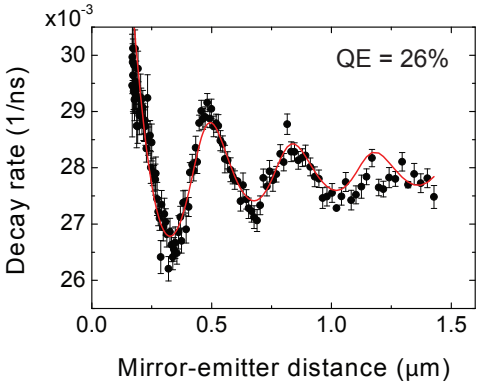

Figure 3.4: Dots: decay rate as a function of the emitter distance to mirror, extracted from the decay rate map shown in figure 3.3(b). Solid line: fitted LDOS on the measured rate oscillations with fit parameters γ_r, γ_{nr} and a set of dipole moment orientations. The shown QE is the most-likely value.

respectively

$$\rho_{||}(z) = \frac{3}{4}\mathrm{Im}\int_0^\infty \left\{[1+r^s(\kappa_{||},z)e^{-2ik_z h}]+ (1-\kappa_{||}^2)[1+r^p(\kappa_{||},z)e^{-2ik_z h}]\right\}\frac{i\kappa_{||}d\kappa_{||}}{\kappa_z}.$$

In this formulation, the emitter is understood to be buried at a depth h into the glass-air interface. The integration variable $\kappa_{||}$ represents the magnitude of the parallel wavevector normalized to the wave number k in glass. The perpendicular wave vector follows as $\kappa_z = k_z/k = \sqrt{1-\kappa_{||}^2}$. The mirror enters through the reflection coefficient r^s and r^p. These are the s- and p-reflection coefficient for waves impinging from the glass side on the composite system of the glass-air interface at $z = 0$, plus the metallic mirror at height z above the glass air interface. This composite amplitude reflection coefficient for a double interface is simply calculated from the Fresnel coefficients given tabulated optical constants and the separation z, according to the textbook derivation for a two-interface system

$$r = r_{12} - \frac{(t_{12})^2 r_{23} e^{2ik_{z,2}z}}{1 - r_{12}r_{23}e^{2ik_{z,2}z}}.$$

Here the subscript 12 is understood to refer to the glass-air interface, 23 to the air-mirror interface s and p superscripts are suppressed, and $k_{z,2}$ is understood to be the perpendicular wave vector in air, given the parallel wave vector $k\kappa_{||}$ in the integrand. An important realization about the integral is that it runs over both propagating, and

evanescent contributions. In particular, the contributions with $\kappa_{||} < 1$ are contributions corresponding to propagating waves in glass. Contributions with larger $\kappa_{||}$ contain evanescent waves, i.e., decay rate contributions due to the mirror system that do not end up in far field radiation. In part this consists of quenching by the mirror, and in part this consists of emission into surface plasmon polaritons. An important abstraction here is that the required Fresnel reflection constants are equally valid when evaluated at large parallel wavevector, i.e., for evanescent waves, and that they contribute a pole at every guided mode of the system. Given that the parallel and perpendicular dipole orientation are the principal axes for a planar geometry, the local density of states normalized tot that in vacuum for a dipole at an angle θ relative to the sample normal reads

$$\rho(z,\theta) = \cos^2\theta\rho_{\perp}(z) + \sin^2\theta\rho_{||}(z).$$

Figure 3.5 shows the calculated LDOS map of the planar glass-air-mirror system for a dipole buried in the semi-infinite glass slab and oriented parallel (a) or perpendicular (b) to the interface. The vertical axes in figure 3.5 represents the depth h at which the emitter is positioned inside the glass and the horizontal axis represents the glass-mirror distance z which is equal to the thickness of the sandwiched air layer. We set the emission wavelength of the dipole to 680 nm corresponding to the peak emission wavelength of the NV centers and assume dielectric constants of $\epsilon_{glass} = 1.4^2$ and $\epsilon_{Ag} = -21.04 + 0.8i$ for glass and silver mirror layers, respectively. We note that the LDOS oscillations are more pronounced for dipoles oriented parallel to the interface.

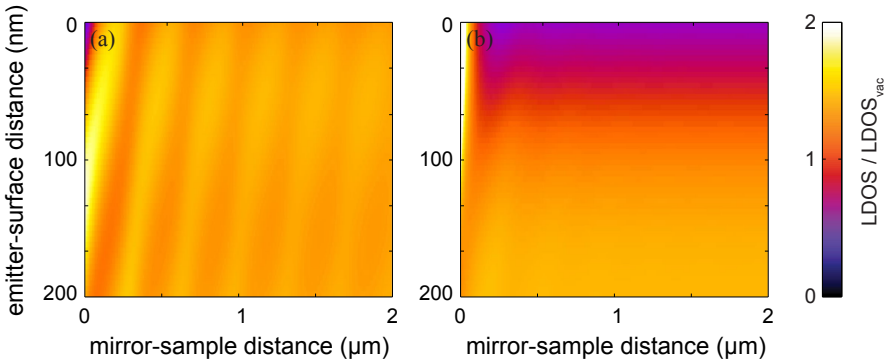

Figure 3.5: LDOS map of a planar glass-air-mirror as function of the distance between emitter and glass-air interface and as function of glass-mirror distance for (a) parallel, and, (b) perpendicular dipole moment orientation. The wavelength of the emission is set to 680 nm corresponding to the peak emission wavelength of the NV centers. LDOS values are normalized to the value in vacuum.

We fit the experimental decay rate data using the theoretical LDOS $\rho(z+d,\theta)$ according to $\gamma(z) = \gamma_{\mathrm{nr}} + \gamma_{\mathrm{r}}\rho(z+d,\theta)$, where γ_{nr} is the nonradiative, and, γ_{r} is the

radiative decay rate, and θ is the dipole orientation relative to the normal to the plane. A small offset d appears due to the unknown distance-of-closest approach in shear-force microscopy which is of the order of $d \approx 15\,\mathrm{nm}$. The source depth h into the glass we have set to 150 nm, corresponding to the expected average depth of the NV centers into the FOX spin-on glass layer. We use as fit function $\gamma = \gamma_{\mathrm{nr}} + \gamma_{\mathrm{r}}[\alpha \cdot \rho_{\parallel} + (1-\alpha)\cdot\rho_{\perp}]$, where $\rho_{\parallel,\perp}(z,d,\theta)$ is the calculated LDOS for dipoles parallel and, respectively, perpendicular to the surface and $\alpha = \cos^2\theta$ parametrizes dipole moment orientation θ. To be inferred from the fit to the data are α, the quantum efficiency ($0 \le QE \le 1$), and the total decay rate γ_{tot} in absence of the mirror. We sweep θ through its range and at each value of θ apply a maximum likelihood fitting routine to obtain the values of QE and γ_{tot}, as well as the residuals between the fitted curve and the measured dataset. By minimizing the residuals of the fit we obtain the set of most likely parameters. This gives a range of quantum efficiency values for which the fit is consistent with the data. Figure 3.6 shows the fitted values as a function of θ for the particular data set shown in figure 3.4. We find a most likely quantum efficiency of 26% and a dipole moment orientation within 20° along the sample plane. The corresponding fit to the experimental data is shown as the red solid line in figure. 3.4. According to figure 3.6 the range of quantum efficiencies consistent with the data for this NV center is bounded from below by 26%, and from above by 50%. To our knowledge this is the first experimental calibration of the quantum efficiency of a single NV center in a diamond nanocrystal.

Care must be taken that a correlation exists between the dipole orientation θ, and the apparent quantum efficiency $\gamma_{\mathrm{r}}/(\gamma_{\mathrm{nr}} + \gamma_{\mathrm{r}})$ returned by the fit routine, due to the fact that the LDOS for different dipole-moment orientations is similar in qualitative z-dependence, but different in oscillation contrast. In case the dipole moment orientation of the NV center is known, which could in principle be realized using Fourier microscopy [19], one can extract a more precise value for the quantum efficiency. The range of θ commensurate with the measurement uncertainty of the data in figure 3.4 is $\Delta\theta = \pm 45°$. Even within that range of $\theta \pm \Delta\theta$, the quantum efficiency remains bounded to $QE \le 50\%$. We therefore conclude that the quantum efficiency of the individual NV defect of Fig. 3.4 does not exceed 50% and is most likely as low as 26%. We note that in contrast to the 1D dipole moment assumed here, NV centers have been reported to posses two dipole moments in a plane normal to the symmetry axis of the NV center (along $\tilde{\theta}$) [20]. In this case the same fit function applies but with $\alpha = 1 - 1/2\cos^2\tilde{\theta}$, assuming all dipole orientations within the plane are equally sampled. This re-interpretation of α does not affect the determined rate and quantum efficiency. While we indeed fit $\alpha \ge 1/2$, both the 1D and 2D model are consistent with our data.

In order to investigate the typical quantum efficiencies of NV centers, we selected five random NV centers and examined them with the moving mirror experiment as explained above. Each nanodiamond was selected to be a single NV center containing nanocrystal according to the criteria we outlined in section 2.2.3, without further post-selection for inclusion in the Drexhage experiment. Table 3.1 summarizes the confidence intervals for the fitted values of the quantum efficiencies, given that we do not know the dipole orientation a priori. The total decay rate γ_{tot}, i.e. the sum

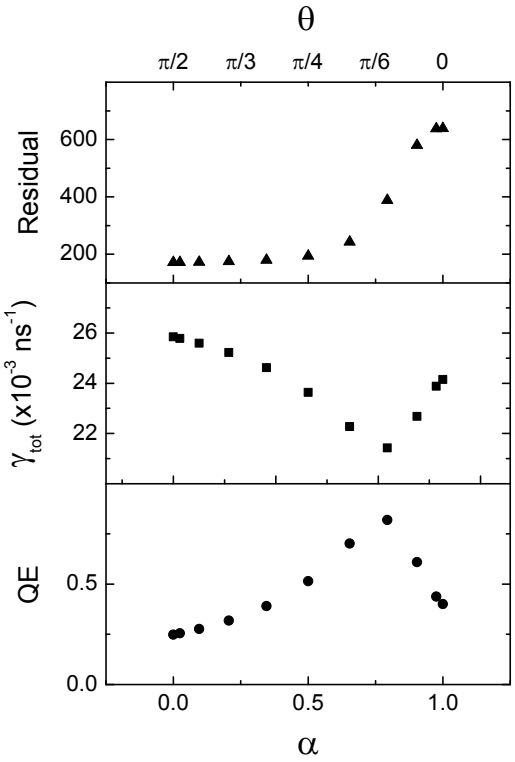

Figure 3.6: Fitted parameters QE and γ_{tot} as a function of α and θ.

of γ_{r} and γ_{nr} varies almost over a factor 2, and can be fitted accurately. In Table 3.1 we also report radiative and nonradiative decay rates. Values are reported as fitted to the data while fixing the dipole orientation at its most likely value, in which case the data can be fit with small error bars on γ_{r} and γ_{nr}. The wide range of quantum efficiencies consistent with the data of course imply that in a completely free fit γ_{r} and γ_{nr} both have a large error bar, though their sum γ_{tot} does not. We find that the different NV centers we probed, while having reasonably comparable brightness, in fact have widely different quantum efficiencies. For instance, NV center 4 (figure 3.7(a)) has an efficiency certainly below 14%, while NV center 5 (figure 3.7(b)) has a quantum efficiency certainly above 58%, in the range 58% to 90%. Furthermore, we note that the fits neither result in the conclusion of a fixed nonradiative rate at varying radiative rate, nor conversely in the conclusion that the radiative rate is a constant while the nonradiative rate varies. Instead, both the radiative and the nonradiative decay rates are distributed. Even with the wide error bars on quantum efficiencies, we establish that both distributions span at least around a factor two in range. Our measurements

NV center #	1	2	3	4	5
QE range	26% – 50%	23% – 45%	27% – 58%	9% – 14%	58% – 90%
γ_{tot} ($\mathrm{ns}^{-1} \times 10^{-3}$)	25.7±0.2	29.2±0.2	33.9±0.4	42.2±0.2	39.7±0.9
γ_{r} ($\mathrm{ns}^{-1} \times 10^{-3}$)	6.7±0.5	6.8±0.6	9±1	4.0±0.4	23±3
γ_{nr} ($\mathrm{ns}^{-1} \times 10^{-3}$)	19.0±0.5	22.5±0.6	25±1	38.2±0.5	17±3
Brightness (kADU/300 ms)	102	112	139	144	135

Table 3.1: Extracted quantum efficiencies, rates and brightnesses for five randomly chosen NV centers in 100 nm nanodiamonds. Quantum efficiencies are quoted as a range of values, taking into account that the dipole orientation is a free parameter. In this fit procedure, the proper fit parameters are the quantum efficiency and the total decay rate, which has small error bar. For completeness we also show the two derived quantities γ_{r} and γ_{nr}. These rates and their error bars are given as fitted when fixing the dipole orientation to its most likely value. Fitted brightnesses were converted to CCD response units to be comparable with figure 4.2 (1 ADU on our CCD camera corresponds to approximately 6 impinging photons).

hence show that the common tacit assumption of near-unit quantum efficiency and nearly identical emission characteristics barring those due to depolarization factors in the nanodiamonds should be discarded.

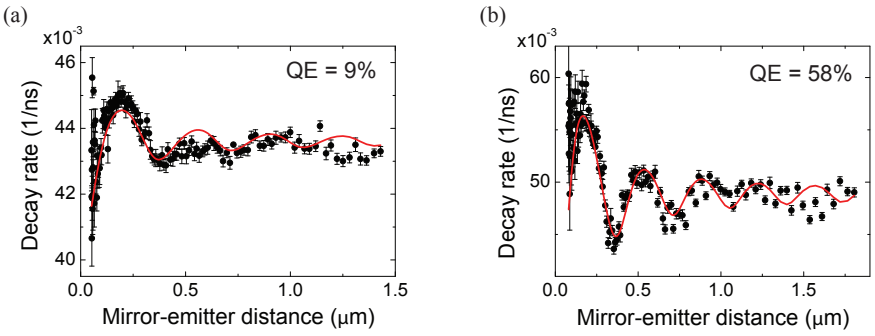

Figure 3.7: (a) and (b) Decay rate as a function of emitter-mirror distance for two other NV centers (number 4 and 5 in table 3.1, respectively) and the fitted rate from LDOS calculation.

3.4 Conclusions and outlook

In conclusion, we presented two techniques to quantify the quantum efficiency of single NV centers. Using liquid-tuning method on small nanodiamond NV centers, we find no evidence that small single NV centers are responsive LDOS probes when applying moderate LDOS variations, commensurate with the assumption of low quantum efficiency for NV centers in small nanocrystals. Furthermore, we presented a

technique in which LDOS variations are introduced by a nanomechanically moving mirror. Using this technique, for the first time we measured the quantum efficiency of single nanodiamond NV centers. Our measurements show that even NV centers in large nanocrystals show a wide range of quantum efficiencies when probed in a controlled LDOS experiment. For NV centers in 100 nm nanocrystals we find quantum efficiencies distributed between 10% and 90%. For the smaller nanodiamonds, the scanning mirror technique turned about to be inappropriate because the much weaker emission brightness of NV centers in nanodiamonds necessitated much higher pump powers, to a level at which our metallized microspheres melted. Accordingly, for the smaller NV centers we can only speculate about quantum efficiency. The fact that NV centers in small diamonds did not respond to LDOS changes, and that they are markedly dimmer leads us to believe that their efficiency is likely a factor of two smaller on average.

If we combine the findings of Chapter 2 and 3 together, we conclude that our quest to determine the suitability of nanodiamonds as photonic LDOS probes, or as building blocks for hybrid photonic systems has led to a disappointing conclusion. We have investigated the brightness, decay rate, and quantum efficiency of single NV centers in nanodiamonds of 25 nm, and of 100 nm median size. For both size ranges a wide distribution in brightnesses and rates is found, consistent with reports by earlier workers. We conclude that the wide distribution of rates is due to a distribution in radiative rates, nonradiative rates and quantum efficiencies. This conclusion contradicts earlier work, that interpreted the wide distribution of decay rates as mainly due to a photonic effect that causes a distribution in radiative decay rates via the LDOS. Instead, our measurements show that even NV centers in large nanocrystals show a wide range of quantum efficiencies when probed in a controlled LDOS experiment. For applications in nanophotonic experiments using single NV centers, a most problematic property is that quantum efficiency does not correlate with brightness, due to the fact that both the radiative and nonradiative rate are distributed. In other words, screening nanodiamonds to pick the best one to probe LDOS or for incorporation in a photonic device can not rely on a simple metric such as spectrum or brightness. Instead, we argue that future work in the hybrid assembly of nanodiamonds in plasmonics and photonic crystals to realize accelerated spontaneous emission decay always requires an experimental protocol in which nanodiamonds are first individually calibrated in terms of quantum efficiency. While we have shown a method for such calibration, this is a highly tedious procedure that is not easily implementable and requires dedicated near-field manipulation equipment.

In this work, we have not speculated on the origin of the apparent low quantum efficiency of single NV centers in nanodiamonds. We close with two remarks on the origin of the low apparent quantum efficiency. Firstly, we have treated the NV center as a quasi two-level system. Our experiments thus address the question what the apparent quantum efficiency is when attempting to use an NV center as a two-level LDOS probe. From the NV center spectrum it is clear that the spectrum is very wide with a large vibrational broadening spectrum. Moreover it is well known that the NV^- center is not a two level system. Instead, the NV^- has different spin sublevels,

and may experience spin-flip intersystem crossing between allowed spin transition manifolds. The rates for these transitions were recently characterized in detail for NV centers in bulk diamond in Ref. [21]. A further complication is that the NV^- defect may infrequently transition to an uncharged NV center that also luminesces, yet at different rate and efficiency. The many rates involved in these transitions can further vary between NV centers due to, e.g., variations in crystal strain. A full treatment of the response of NV centers to LDOS changes would hence have to treat the full rate equations in which radiative transition rates are, and intersystem crossing rates are not, affected by LDOS. An important step beyond our work will be to perform the measurements we have described here but employing it on the most controlled diamond system available (CVD grown diamond sheets by Element Six ,used in spintronic experiments) and applying the spin selective techniques reported by Robledo [21] to establish what the nonradiative and radiative rates are for each transition separately, instead of lumping rates into effective two-level parameters. While the LDOS changes we have applied using a mirror are broadband LDOS changes that modify radiative transitions roughly equally across the emission spectrum, LDOS changes that have strong spectral features could be used advantageously to enhance or suppress the importance of intersystem crossing. As further part of this proposed follow up work, we note that an independent means to obtain rates would be to fit a multi-level decay model to the temporal $g^{(2)}(\tau)$ photon-correlation. Fitting a pump intensity series of $g^{(2)}$ correlation functions measured in absence of the mirror, together with data on the concomitant saturation power and measured brightness at saturation could give more insight in the rates, complementary to our Drexhage data. Even more exciting could be to measure $g^{(2)}(\tau)$ as function of the NV-center mirror distance.

Having established that further work is required to separate the quantum efficiencies reported here into parameters per transition in a more complete level scheme, we turn to possible reasons for the below-unity values of quantum efficiency that we find. The lower brightness of the smaller NV centers, as well as their lack of response to LDOS changes suggest that the surface, i.e., surface contamination with carbon, or surface defects may play a role in providing quenching sites. Indeed, it has already been suggested for very small (5 nm) nanodiamonds that NV centers may suffer quenching due to graphite shells on the diamonds [22, 23]. While the nanodiamonds we used have been employed by several groups in spontaneous emission control experiments in untreated form, exactly as in our experiments, additional surface treatments such as by prolonged immersion in boiling sulphuric acid, or cleaning in Köningswasser have been proposed by several workers. Whether or not such treatments actually affect quantum efficiency is as yet unclear, as is whether quenching can be completely suppressed. We propose that the quantum efficiency calibration method that we demonstrated will be an indispensable tool to evaluate such cleaning methods, as well as to screen other color centers in diamond for advantageous fluorescence properties.

Appendix: calibration of nanomechanical tuning of LDOS on fluorescing beads and dye layers

In this appendix, for completeness we replicate a calibration study of our nanomechanical Drexhage measurement undertaken by M. Frimmer in our lab, and published in a joint publication in Ref. [16]. As calibration samples, we prepared homogeneous, 70 nm thick PMMA films doped with dye (Bodipy TR, D-6116, Invitrogen) by spincoating. The spin-coated solution was prepared by diluting 5 mg of dye in 1 ml of anisole, and subsequent 30-fold dilution of the dye solution in a 2% solution of 950 K PMMA in anisole. As second type of calibration sample we used clean cover slips with dye-doped polystyrene beads (diameter 100 nm, F8801, Invitrogen) dispersed at low concentration. We evaporated about 60 nm of SiO_2 on top of the sample for mechanical protection.

For the first type of calibration measurement, we use our inverted confocal fluorescence-lifetime imaging (FLIM) microscope to collect lifetime data from a single, randomly chosen, diffraction limited spot in the film while scanning the mirror in shear-force contact over the sample. For the second type of calibration measurement, we locate a single fluorescing bead in the focus and collect lifetime data while scanning the mirror. In all instances we used the picosecond pump laser (532 nm, 10 MHz), and the 100×, NA=1.4 objective also used for our diamond experiments. Figure 3.8(a) shows a fluorescence intensity map obtained from a single bead while scanning the mirror, while panel (b) shows the associated fluorescence lifetime image, obtained by fitting the time traces for each pixel to single exponential decay. The circular symmetry of Figs. 3.8(a,b) is expected due to the symmetry of our micromirror with respect to its touching point with the sample. Procedurally, we exploit this symmetry by determining the center of the circular patterns in Figs. 3.8(a,b) and concatenating TCSPC data of pixels with equal distance to the center of the pattern into a single decay trace. Given the known diameter of the micromirror to convert in-plane distances into a vertical mirror-emitter separation, while assuming the shear force distance between micromirror and sample to be negligible, we obtain the decay rate as a function of distance to the mirror , shown as the full diamonds in Fig. 3.8(c). We clearly observe characteristic decay-rate oscillations in front of the mirror [12]. Panel (c) also obtains typical traces obtained on the dye films.

For both the film case, and the bead case we have calculated the LDOS, including the layered system we used to immobilize the beads. We find excellent agreement, assuming a unit quantum efficiency for this dye, for separations between mirror and emitters above 200 nm. At smaller separations deviations occur, which we attribute to the fact that for both films and beads, ensemble averaging over the spectral, orientational and positional ensemble of molecules is challenging to accurately replicate in the modelling. Indeed, the optimal calibration technique would be to use single emitters of known and fixed dipole orientation, as well as known quantum efficiency.

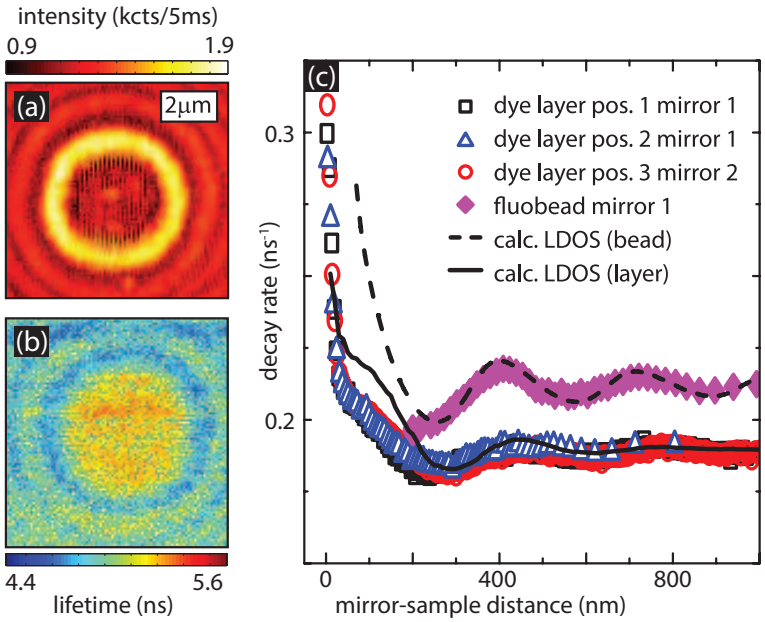

Figure 3.8: (a) Fluorescence-intensity map of dye-doped bead in laser focus as micromirror is scanned across it, showing ring-shaped intensity variations. Each pixel denotes a specific lateral position of the mirror. (b) Fluorescence-lifetime map of same measurement that yielded (a). (c) Decay rate versus mirror-sample distance, as obtained from (b) by combining pixels with identical distance to the center of the circular pattern. Full diamonds are data obtained from (b), measured on 100 nm fluorescing bead. Open symbols show results on continuous dye layers (different positions, and different micromirrors [see legend]). Solid and dashed lines are analytical calculations for dye layer and fluorescing bead, respectively. This figure is replicated from [16], presenting a calibration performed by M. Frimmer.

References

[1] S. Schietinger, M. Barth, T. Aichele, and O. Benson, *Plasmon-enhanced single photon emission from a nanoassembled metal-diamond hybrid structure at room temperature*, Nano Lett. **9**, 1694 (2009).

[2] R. Kolesov, B. Grotz, G. Balasubramanian, R. J. Stöhr, A. A. L. Nicolet, P. R. Hemmer, F. Jelezko, and J. Wrachtrup, *Wave–particle duality of single surface plasmon polaritons*, Nature Phys. **5**, 470 (2009).

[3] A. Huck, S. Kumar, A. Shakoor, and U. L. Andersen, *Controlled coupling of a single nitrogen-vacancy center to a silver nanowire*, Phys. Rev. Lett. **106**, 096801 (2011).

[4] P. V. Ruijgrok, R. Wüest, A. A. Rebane, A. Renn, and V. Sandoghdar, *Spontaneous emission of a nanoscopic emitter in a strongly scattering disordered medium*, Opt. Express **18**, 6360 (2010).

[5] F. A. Inam, T. Gaebel, C. Bradac, L. Stewart, M. J. Withford, J. M. Dawes, J. R. Rabeau, and M. J. Steel, *Modification of spontaneous emission from nanodiamond colour centres on a structured surface*, New J. Phys. **13**, 073012 (2011).

[6] B. Buchler, T. Kalkbrenner, C. Hettich, and V. Sandoghdar, *Measuring the quantum efficiency of the optical emission of single radiating dipoles using a scanning mirror*, Phys. Rev. Lett. **95**, 063003 (2005).

[7] M. Leistikow, J. Johansen, A. Kettelarij, P. Lodahl, and W. Vos, *Size-dependent oscillator strength and quantum efficiency of CdSe quantum dots controlled via the local density of states*, Phys. Rev. B **79**, 045301 (2009).

[8] A. I. Chizhik, A. M. Chizhik, D. Khoptyar, S. Bär, A. J. Meixner, and J. Enderlein, *Probing the radiative transition of single molecules with a tunable microresonator*, Nano Lett. **11**, 1700 (2011).

[9] E. Snoeks, A. Lagendijk, and A. Polman, *Measuring and modifying the spontaneous emission rate of erbium near an interface*, Phys. Rev. Lett. **74**, 2459 (1995).

[10] T. M. Hensen, de Dood, M. J. A., and A. Polman, *Luminescence quantum efficiency and local optical density of states in thin film ruby made by ion implantation*, J. Appl. Phys. **88**, 5142 (2000).

[11] R. Walters, J. Kalkman, A. Polman, H. Atwater, and M. d. Dood, *Photoluminescence quantum efficiency of dense silicon nanocrystal ensembles in SiO_2*, Phys. Rev. B **73**, 132302 (2006).

[12] K. H. Drexhage, *Influence of a dielectric interface on fluorescence decay time*, **1-2**, 693 (1970).

[13] M. L. Andersen, S. Stobbe, A. S. Sørensen, and P. Lodahl, *Strongly modified plasmon–matter interaction with mesoscopic quantum emitters*, Nature Phys. **7**, 215 (2011).

[14] R. M. Amos and W. L. Barnes, *Modification of the spontaneous emission rate of Eu^{3+} ions close to a thin metal mirror*, Phys. Rev. B **55**, 7249 (1997).

[15] A. Kwadrin and A. F. Koenderink, *Gray-tone lithography implementation of drexhage's method for calibrating radiative and nonradiative decay constants of fluorophores*, J. Phys. Chem. C **116**, 16666 (2012).

[16] M. Frimmer, A. Mohtashami, and A. F. Koenderink, *Nanomechanical method to gauge emission quantum yield applied to nitrogen-vacancy centers in nanodiamond*, Appl. Phys. Lett. **102**, 121105 (2013).

[17] H. Urbach and G. Rikken, *Spontaneous emission from a dielectric slab*, Phys. Rev. A **57**, 3913 (1998).

[18] L. Novotny and B. Hecht, *Principles of nano-optics*, Cambridge University Press, 2006.

[19] M. A. Lieb, J. M. Zavislan, and L. Novotny, *Single-molecule orientations determined by direct emission pattern imaging*, J. Opt. Soc. Am. B **21**, 1210 (2004).

[20] R. J. Epstein, F. M. Mendoza, Y. K. Kato, and D. D. Awschalom, *Anisotropic interactions of a single spin and dark-spin spectroscopy in diamond*, Nature Phys. **1**, 94 (2005).

[21] L. Robledo, H. Bernien, T. van der Sar, and R. Hanson, *Spin dynamics in the optical cycle of single nitrogen-vacancy centres in diamond*, New J. Phys. **13**, 025013 (2011).

[22] C. Bradac, T. Gaebel, N. Naidoo, M. J. Sellars, J. Twamley, L. J. Brown, A. S. Barnard, T. Plakhotnik, A. V. Zvyagin, and J. R. Rabeau, *Observation and control of blinking nitrogen-vacancy centres in discrete nanodiamonds*, Nat. Nanotechnol. **5**, 345 (2010).

[23] B. R. Smith, D. W. Inglis, B. Sandnes, J. R. Rabeau, A. V. Zvyagin, D. Gruber, C. J. Noble, R. Vogel, E. Osawa, and T. Plakhotnik, *Five-nanometer diamond with luminescent nitrogen-vacancy defect centers*, Small **5**, 1649 (2009).

4

Nanoscale excitation mapping of plasmonic patch antennas

We experimentally investigate the resonant modes of plasmonic patch antennas using angle-resolved cathodoluminescence imaging spectroscopy. Plasmonic modes residing in the patch antenna are locally excited using a scanning electron beam providing high resolution spectral and spatial maps of the modes of patch antennas corresponding to variations in the local density of optical states in the antennas. A semi-analytical model is used to qualitatively explain the experimentally observed modes. Furthermore, emission patterns, directionality and beam steering properties of patch antennas are studied in different patch sizes and at different wavelengths. Strong directionality and control over the output beam angle as a function of excitation position is observed. A distributed dipole model is used to explain the radiation pattern and beam width of the patch antenna radiation which shows a good agreement with the experiment.

4.1 Introduction

For technological applications in improving light sources, LEDs and fluorescence microscopy, as well as for breakthroughs in quantum optics, many efforts are devoted to optimizing light extraction from single emitters [1, 2]. Among strategies to realize ultrabright sources, researchers have pursued integration of active materials with

dielectric structures that include microcavities [3], Bragg stacks, photonic crystals [4, 5], as well as integration of sources with metallic nano-objects [6]. In particular, the field of 'plasmonics' promises to enhance the brightness and directivity of light sources through a set of effects. First, at Ag, Au and Al surfaces and particles, plasmon resonances feature strongly confined fields with very high per-photon field strength. On this basis one expects large local density of optical states (LDOS) enhancements that accelerate spontaneous emission decay of emitters into plasmon modes. Such acceleration of excited state decay promises very high fluorescent photon flux per emitter when emitters are pumped near saturation. As a second effect, plasmonics can aid outcoupling of light into advantageous directions. The most established methodology is to generate 'phased array antennas' like Yagi-Uda plasmon antennas [6–10], bull's eyes [11, 12] and plasmonic lattice antennas [13, 14], in which plasmon scatterers driven by the fluorophore act as secondary coherent sources so that a directional emission pattern can be obtained. A second, more recently proposed method is to use comparatively large scatterers in which a coherent superposition of multipoles can be excited that jointly show directional emission [15, 16]. Finally, a third approach that was proposed in the pursuit of ultrabright single photon sources is the use of socalled 'patch antennas' [17, 18]. Such patch antennas rely on patches of metal several wavelengths across in which a nearby emitter can excite planar guided modes that scatter out at the edges [19].

A particularly promising patch antenna that was recently introduced in Refs. [17, 18] is based on circular patches with a metal-insulator-metal (MIM) geometry. Belacel et al. [18] experimentally realized such patch antennas by making a thin dielectric film loaded with quantum dots on a thick gold surface. After pinpointing single quantum dots in the film, they could position circular gold patches of microns across centered on top of a single quantum dot, and study the fluorescence decay rate before and after deposition of the patch. This type of geometry is expected to show a large LDOS enhancement due to the fact that the MIM geometry supports a guided plasmon mode that is tightly confined, with a very strong field in the gap, normal to the metal surfaces. Indeed, measured Purcell factors up to 80 have been reported [18]. Furthermore theoretical analysis, corroborated by the measured data, indicate that such MIM patch antennas give directional emission in a narrow cone normal to the patch with an angular width of around 35°, provided the patch is centered on the source. This directional emission is expected to come about because the tightly confined guided MIM mode excited by the emitter propagates to the disk edge, where it couples out as radiation into the far field. Since the entire patch edge is a coherent radiator, emission is expected to be directed, as fluorescence back-aperture imaging indeed shows according to Ref. [18].

The physics of patch antennas is expected to contain a set of salient features that are difficult to completely unravel in fluorescence experiments such as in single emitter experiments, owing to the fact that one ideally would scan the point of excitation and the emission wavelength continuously while examining enhancements of the total emitted power, as well as directivity for different disk sizes. In this chapter we perform exactly such a study using angle-resolved cathodoluminescence imaging spectroscopy (ARCIS) [20, 21]. To highlight the expected complexity of this system, calculations of the Purcell factor indicate that one expects a very large set of resonant

modes with different radial and azimuthal quantum numbers that are simultaneously involved [17, 22, 23]. Cathodoluminescence imaging can be used not only to reveal such a complicated dependence of the local density of states on both frequency and excitation position, but also allows one to answer the question how such complex multimode systems can give robust directionality.

This chapter is structured as follows. In section 4.2 we present a simple analytical model for the mode structure and LDOS of circular MIM patch antennas. After introducing our experimental methods for fabricating patch antennas, and spectrally, spatially and wave vector resolved cathodoluminescence (section 4.3) we present measured spatial cathodoluminescence (CL) maps in section 4.4. Spatial maps indeed show a marked spatial and spectral structure in local density of states. Finally we turn to the angular characteristics of differently sized patch antennas at various wavelengths and excitation positions in section 4.5. Commensurate with semi-analytical modeling results described in section 4.6, we find that patch antennas are more directional as they grow in size, and that they show controllable beam steering as the excitation position is swept from the disk center to approximately halfway their radius.

4.2 Theoretical analysis and calculation

In this section we set up a simple analytical model outlining the expected mode structure and spatially dependent Purcell factor of patch antennas. Resonant modes of the patch antennas are analytically investigated using a Bessel-type standing-wave resonator model introduced by Filter *et al.* [22]. They considered circular resonators which support propagating surface plasmon polaritons (SPPs) confined within the disk area. Upon reflection from the antenna edges, SPPs form standing fields inside the antenna as a result of interference with the outward propagating SPPs and can be described by Bessel functions. Here we apply this model, to describe vertically stratified patch antennas that have an MIM geometry.

The metal-insulator-metal (MIM) geometry of the patch antennas supports two transverse-magnetic (TM) plasmonic modes with opposite symmetries. Figure 4.1c shows a numerical calculation of the real (solid curves) and imaginary (dotted curves) part of the dispersion relation of the two modes for an infinitely extended MIM structure with the same layer thicknesses as our patches. As input for this calculation we use tabulated optical data [24], inserted in a standard stratified system solver that solves for complex wave vector at real frequency [25]. Symmetric (blue curve) and anti-symmetric (red curve) modes are defined according to the symmetry of the magnetic field profile inside the structure as shown in figure 4.1 (a). For comparison, the dispersion relation of the gap material, i.e. silica (gray dotted line) and the light-line (black dotted line) of the surrounding air are also presented in the dispersion diagram. The anti-symmetric mode has a dispersion relation very close to the light-line indicating a mode-index close to air. However, the symmetric mode has a dispersion well beyond the light line which indicates that the mode is strongly confined to the metal. This strongly dispersive and strongly confined MIM mode has been well studied in scattering experiments by

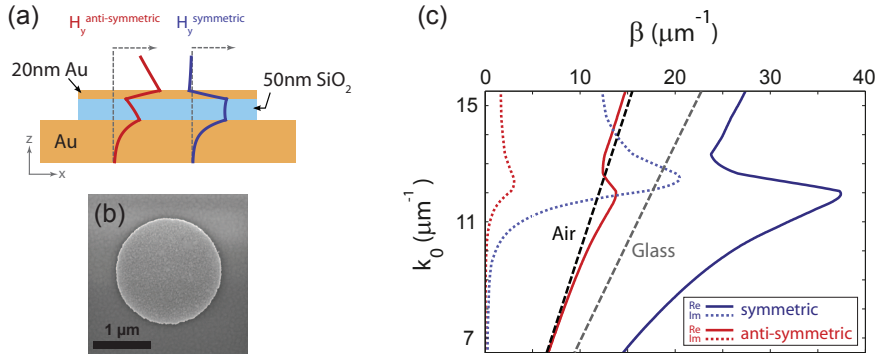

Figure 4.1: (a) Schematic of a patch antenna. The planarized MIM structure supports two transverse magnetic modes (H_y) with opposite symmetries. (b) SEM image of a fabricated patch antenna with a diameter of 1.8μm. (c) real (solid curves) and imaginary (dotted curves) parts of the dispersion relation of the planarized MIM structure of part (a) with two supported transverse magnetic modes. On the axes, k_0 and β represent free-space and MIM wavenumbers, respectively. Glass dispersion relation and light lines are also indicated for comparison.

Miyazaki et al. [26, 27], its dispersion has been studied in cathodoluminescence [28], and this mode has been identified as responsible for large Purcell enhancements [29, 30] for dipoles placed in the gap and oriented normal to the interfaces. On the basis of this high Purcell factor for polarizations matching the incident electron beam in our experiment, we expect to mainly excite the symmetric MIM mode in our CL experiment. Since the anti-symmetric mode is weakly confined and almost index-matched with air, we expect that it does not contribute strongly to the scattered field at the abrupt edges of the antenna. Therefore, in the following we restrict our analysis to the symmetric mode contribution, which is also the mode identified as relevant in spontaneous emission experiments on basis of Purcell factor calculations [18].

In order to estimate the total collected CL intensity, we set up a simple semi-analytical model for the local density of states in the patch antenna starting from the model of Filter et al. [22] which proceeds as follows. First we find the eigenfrequencies and mode profiles of eigenmodes. This step requires as Ansatz for each mode profile that it factorizes as

$$E_z^m(r,z) = a(z) J_m(k_{MIM} r) e^{im\varphi}$$

, where $a(z)$ is the MIM waveguide mode profile, m is the azimuthal quantum number, J_m is a Bessel function and k_{MIM} is the complex wave vector of the MIM mode at frequency ω. We note that in this Ansatz, one assumes that the infinite-system symmetric MIM mode dominates. This means not only that the infinite-system asymmetric MIM mode is neglected, but also that any contribution of modes that are bound to the patch edge, and have in-plane wave number different from k_{MIM}, are neglected. We expect this Ansatz to be best for excitation positions away from

the patch edge, and for sufficiently large patches. According to García de Abajo and Kociak [31] an impinging electron beam excites a structure not according to its LDOS at some height z, but rather according to a projected LDOS obtained by integrating along the electron beam trajectory. We note that *within* our Ansatz, the $z-$dependence and in-plane dependence will factorize, meaning that integrating over z will not result in different information unless one goes beyond our Ansatz.

To put our Ansatz we use separation of variables so that the eigenmodes can be written as

$$E_z^m(r,z) = a(z)J_m(k_{MIM}r)e^{im\varphi}. \tag{4.1}$$

Here $a(z)$ is the transverse mode profile obtained by solving for the infinitely extended MIM system, J_m is a Bessel function of the first kind, and $k_{MIM} = k_{MIM}^{'} + ik_{MIM}^{''}$ the complex wave number of the symmetric MIM mode, again found from the infinitely extended system. Next, to find a discrete set of eigenfrequencies one needs to define a boundary condition. For instance, requiring $E_z^m(r = \rho_{n,m}, z) = 0$ as boundary condition, would yield resonant disk radii $\rho_{n,m}$ as the roots of the Bessel function $k_{MIM}\rho_{n,m} = x_n(J_m)$. The mode numbers n and m correspond to radial and axial mode numbers, respectively. In fact, rather than taking as boundary condition $E_z^m(r = \rho_{n,m}, z) = 0$, an accumulated phase ϕ_m upon reflection of the SPPs from the antenna edges can be translated into a correction in the resonant radii calculation as:

$$2k_{MIM}^{'}R + \phi_m = 2x_n(J_m) \tag{4.2}$$

where $R = d/2$ is the physical radius of the disk. It has been shown that this formulation excellently describes the modes of simple metal disks, with a reflection phase ϕ that is disk size and frequency insensitive and can be calculated independently from simulation of reflection of the guided mode at a semi-infinite flat edge [22].

For a given disk size, this procedure yields eigenfrequencies $\omega_{n,m}$ through inversion of the dispersion relation for all available mode numbers. Expanded in terms of eigenmodes, the local density of modes probed by a z-oriented dipole for a lossless system reads

$$\mathbf{N}(\omega, r) = \sum_{n,m} |E_z^{n,m}(r)|^2 \delta(\omega^2 - \omega_{n,m}^2). \tag{4.3}$$

where the mode functions are understood to be normalized. In order to obtain a continuous LDOS spectrum, it is important to realize that each mode suffers a frequency broadening, which we assign according to the damping of the modes due to ohmic and radiation losses. In particular, we sum

$$\mathbf{N}(\omega, r) = \sum_{n,m} |E_z^{n,m}(r)|^2 \mathscr{L}(\omega; \omega_{n,m}, \gamma) \tag{4.4}$$

where $\mathscr{L}(\omega; \omega_{n,m}, \gamma)$ denotes a Lorentzian (normalized to constant integral) centered at $\omega_{n,m}$ and with full width at half maximum γ. It should be noted that in this procedure the only adjustable parameters are the reflection phase ϕ and the linewidth γ. The effect of changing the phase is to shift the entire spectrum of resonances in frequency. For our calculations, the accumulated phase $\phi_m = -1.7$ and the empirical resonance

linewidth [22] $\gamma/\omega = (2k''_{MIM}R)^2 + \gamma_0(1+{\omega_{norm}}^b)^{-1}$ with $\gamma_0 = 0.1$, $b = 1.7$ and normalized frequency $\omega_{norm} = \omega/(1000\,\mathrm{THz})$ are extracted from a COMSOL simulation (see below) by matching the resonance position and width of the fundamental mode.

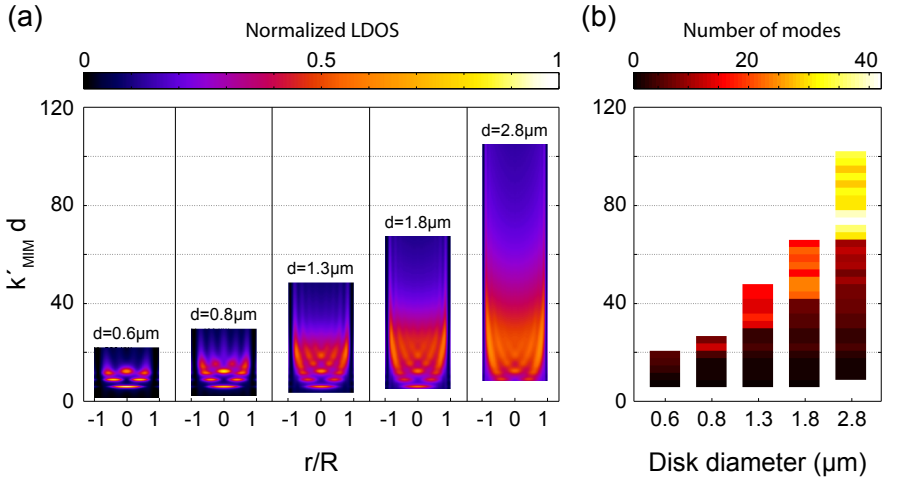

Figure 4.2: (a) Calculated spatial LDOS maps for five different disk sizes as a function of normalized wavenumber $k'_{MIM}d$ and distance to the center of the disk. (b) Histogram of the number of modes participating in the calculation of (a).

Figure 4.2(a) shows the calculated spatial LDOS maps of patch antennas for five different disk sizes. It should be noted that while each eigenmode has an azimuthal dependence ($e^{im\varphi}$ dependence), the LDOS does not. The wavelength on the vertical axis is converted to dimensionless wavenumber $k'_{MIM}(\lambda_0)d$ in order to facilitate direct comparison between different disk sizes. For each disk, the physical frequency range that we report on corresponds to wavelengths from 525 nm to 4000 nm. For each disk size, the LDOS shows resonances, and the resonant bands show clear radial oscillations. It would be tempting to explain these simply as a sequence of monotonically increasing radial quantum number. However, the reader should be warned that radial and angular quantum number coexist, meaning that at higher frequencies the LDOS is composed of many modes, including those with high radial quantum number n and low azimuthal quantum number m, and vice versa. For reference Figure 4.2(b) shows a histogram of the number of the modes at different normalized wavenumbers and disk sizes corresponding to calculation of the modes in figure 4.2(a). The number of modes contributing to LDOS within frequency bands of width γ is typically on the order of ten. The oscillations in LDOS vanish for higher wavenumbers due to larger ohmic damping at shorter wavelengths. Since the eigenfrequencies are only dependent on the fundamental quantity $k'_{MIM}(\lambda_0)d$ (i.e the ratio between two length scales, the MIM wavelength and the disk size), one expects eigenmodes of differently sized disk antennas to occur at the same normalized wavenumber. However, this scaling is not

perfect due to dispersion in the imaginary part of the MIM wave vector. The radial oscillation of the modes smear out for larger disk sizes due to the fact that larger disks support many modes which overlap and therefore cancel out the oscillations. Indeed for a very large disc one would expect the LDOS to converge to that of a semi-infinite MIM film, which would be featureless except for Friedel oscillations [32] right at the film edge.

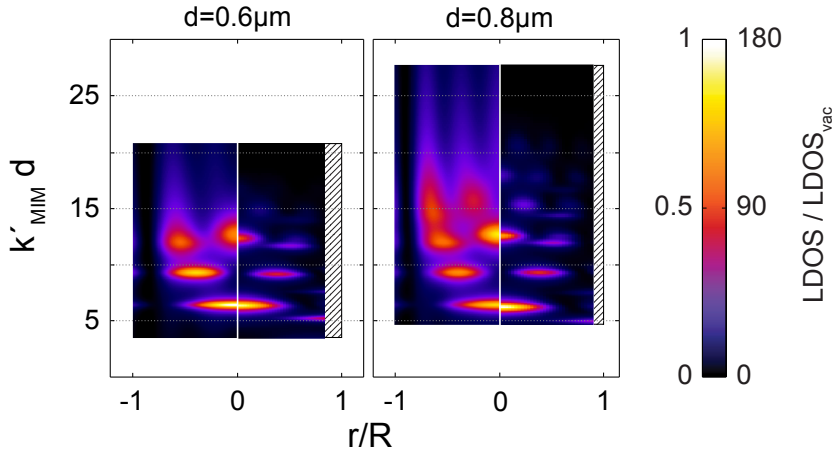

Figure 4.3: COMSOL simulated radiation power for two disk diameters of 0.6 μm and 0.8 μm as a function of normalized wavenumber and distance to the center of the disk. For each disk size, the right part shows the COMSOL simulation radiated power while the left part shows the corresponding calculated LDOS map of Figure 4.2a. The left and right colorbar numbers indicate normalized LDOS (arbitrary and real unit, respectively) and correspond to left and right parts of the graphs, respectively.

As further verification of this analytical model, we have also calculated the LDOS for patch antennas of 0.6 μm and 0.8 μm diameter using COMSOL. Specifically, we model a vertically oriented dipole source located as a small current carrying wire at midheight in the gap. We record the power it emits into the environment that subsequently is dissipated in the metal, as well as the power it emits that is radiated into the far field. We have used the optical constants for gold tabulated by Etchegoin [33] and performed a parametric sweep over 150 frequency points and 33 (31) dipole positions for 0.6 μm (0.8 μm) disk size (calculation time per point approximately 2 minutes on a 2.0 GHz Intel Xeon E5-2620). Figure 4.3 plots the result for the radiated power as function of normalized wavenumber and as function of dipole position. For each disk size, the left part of the plot shows the calculated LDOS map corresponding to Figure 4.2a and the right part shows the COMSOL simulated maps. We have adjusted the phase and the resonance width in our calculation according to the COMSOL simulation for a range of $k'_{MIM}d$ values between 5 to 10 corresponding

to the fundamental mode. We find good agreement between the analytical model and the full wave simulation. Indeed, the COMSOL simulation likewise predicts a set of resonances, of which the lowest is localized at the disk center, while for higher frequencies resonances have an increasing set of antinodes across the disk perimeter, and become increasingly close in frequency. As caveat for interpreting the width of features we note that, especially at higher frequencies, the resonant bands are actually composed of multiple modes centered at slightly different frequencies. The apparent damping is hence higher than the actual damping put into the model.

4.3 Experimental methods

4.3.1 Sample fabrication

Figure 4.1 (a) schematically shows the geometrical structure of patch antennas used in our experiment. The antennas are fabricated by first evaporating a 200 nm thick layer of gold on top of a glass substrate. This layer is optically thick. Next, a layer of positive-tone resist (ZEP520A) is spin-coated over the gold film and circular patches are written in the resist using electron beam lithography. After developing the resist, circular disks are formed by evaporating a 50 nm thick layer of silica (SiO_x where $x \approx 2$) followed by a 20 nm thick layer of gold at a rate of 0.5 nm/s and at an ambient pressure of 10^{-6} mbar. In order to enhance the adhesion of the gold layer to the silica, the sample is treated by an Argon plasma before the gold layer is deposited. Finally, the resist is removed in a 65°C hot bath of 1-Methyl-2-pyrrolidinone (NMP) lift-off solvent. Before performing the measurements, the sample is cleaned with a mild O_2 plasma descum to remove any organic residues. Figure 4.1 (b) shows a scanning electron micrograph of a fabricated patch antenna. Several patch antennas with disk diameters between 0.6 μm to 2.8 μm are fabricated on one sample.

4.3.2 Experimental set up

In order to investigate the resonant modes of the patch antennas we use angle-resolved cathodoluminescence imaging spectroscopy (ARCIS) [20, 21]. Figure 4.4 shows a schematic diagram of the ARCIS setup. A 30 keV electron beam is scanned over a selected patch antenna in steps of 10 nm at a beam current of 0.8 nA. As reviewed by Refs. [34–36], the high-energy electron beam as it approaches the metallic and dielectric interfaces of the antenna induces a vertical transient dipole moment which locally excites the optical modes of the patch antenna. A part of the excited electric field may directly radiate into the far-field, while another part funnels into the MIM mode and subsequently scatters out of the antenna edges into the far-field. The overall radiated CL is then collected by a parabolic mirror that has a total collection angle of 1.46π sr. The light is guided to a spectrometer with a Si CCD detector, or an imaging CCD detector for Fourier analysis from which the angular radiation pattern can be obtained [20].

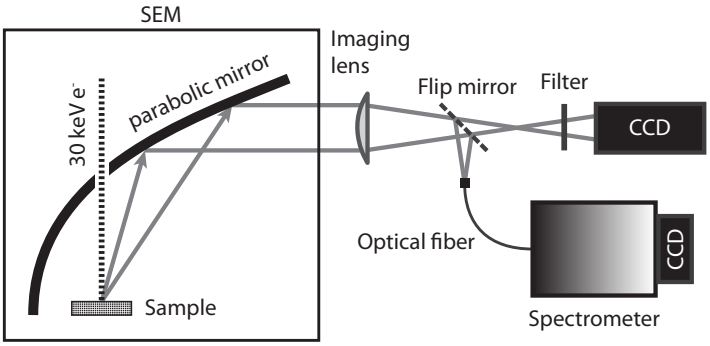

Figure 4.4: Schematic diagram of the ARCIS setup. A 30 keV electron beam is scanned over the sample and the CL emission is collected by the parabolic mirror. The collected light is either guided to a spectrometer through an optical fiber or is projected over an imaging CCD to record the angular radiation pattern.

4.4 Spatial cathodoluminescence maps

In this section, we first present the results of the experimental CL measurements on patch antennas with different diameters and then we compare them to the calculated LDOS maps of section 4.2. This comparison is motivated by the recently developed notion that the rate of excitation of the optical modes in plasmon structures by CL is proportional to the LDOS [21, 37], so that the radiated CL intensity is expected to be proportional to the radiative part of the local density of optical states in the antenna. Figure 4.5 shows spatial maps of CL intensity for a typical patch antenna with disk diameter of 1.8 μm at four different wavelengths integrated over a bandwidth of 10 nm. Here, each pixel corresponds to a position of the electron beam at which the CL intensity is plotted. Due to the high spatial resolution of the scanning electron beam, a very detailed spatial map of the collected CL intensity can be obtained. The spatial intensity maps exhibit concentric rings within the disk area reflecting the circular symmetry of the antenna. It should be noted that, since CL is an excitation spectroscopy technique, the profiles do not correspond to maps of (superpositions) of modes, but rather reflect the total power radiated out of the system due to the different superposition of modes excited for each excitation position on the patch antenna. In order to visualize the measured LDOS of the antennas more clearly, spatial CL intensity maps are azimuthally averaged at each wavelength (10 nm bandwidth) exploiting the radial symmetry of the patch antennas. Figure 4.6a shows azimuthally averaged CL intensity maps of five different patch antennas as a function of wavelength and distance to the center of the antenna. In order to directly compare the CL intensity maps of different disk sizes, wavelength values (λ_0) in Figure 4.6a are converted to dimensionless quantity $k'_{MIM}d$ using the calculated dispersion relation of the infinite MIM structure $k'_{MIM}(\lambda_0)$ (Figure 4.1c) and the disk diameter d.

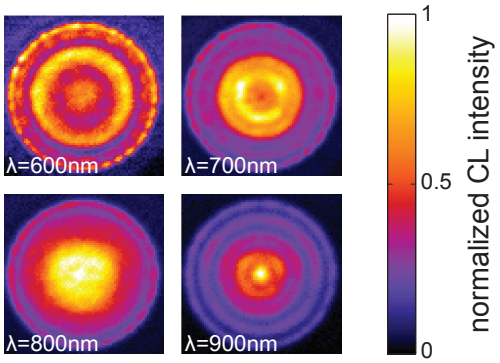

Figure 4.5: Spatial CL intensity maps of a typical patch antenna with disk diameter of 1.8 μm at four different wavelengths integrated over a bandwidth of 10 nm. CL intensity data are corrected for the background (typically around 100 cts/px/0.25 s) and the system response, and are normalized to unity at each wavelength. The maximum counts of the raw map data before correction are equal to 320, 590, 370, and 350 cts/px/0.25 s for wavelengths from 600 nm to 900 nm, respectively.

In order to examine the relation between the CL intensity and LDOS, we compare the CL maps of Figure 4.6 to the LDOS maps of Figure 4.2 that were calculated with the simple model of Filter et al. [22]. Experiment and calculation show qualitative similarities. These include the alternating occurrence of 1, 2 and 3 antinodes in radial LDOS dependence as one sweeps frequency, smearing of the radial oscillations at higher wavenumbers due to ohmic losses, and for large $k'_{MIM}d$ concentration of radial LDOS structures at the disk edges.

Despite the qualitative similarities, there is no one-to-one quantitative correspondence between the measured and calculated spatial mode maps. We identify several probable reasons for this discrepancy. First, we have used patch antennas in the size range corresponding to strong angular directivity, i.e., disks several microns across. Such large disks have a dense plethora of modes, meaning that it is very difficult to obtain a one-to-one alignment of mode structure between experiment and theory. Second, we approximated the CL process in our model as entirely due to the LDOS of symmetric MIM resonances, since this is the mode that presents the largest Purcell factor in the gap for vertically oriented dipoles. This simplification neglects that the infinite layered system also supports an asymmetric MIM mode that can also contribute to CL, as analyzed by Cai et al. and Barnard et al. [36, 38]. Also, the Ansatz of Filter et al. [22] ignores contributions at wave numbers different from k_{MIM} that could result from plasmons strongly localized at the patch edge. Especially at small patch size, neglecting such edge effects could deteriorate the comparison. Even if the simple model is accurate for LDOS (calculated with COMSOL), it need not be for CL, since in CL one needs to integrate contributions from along the electron beam path as worked

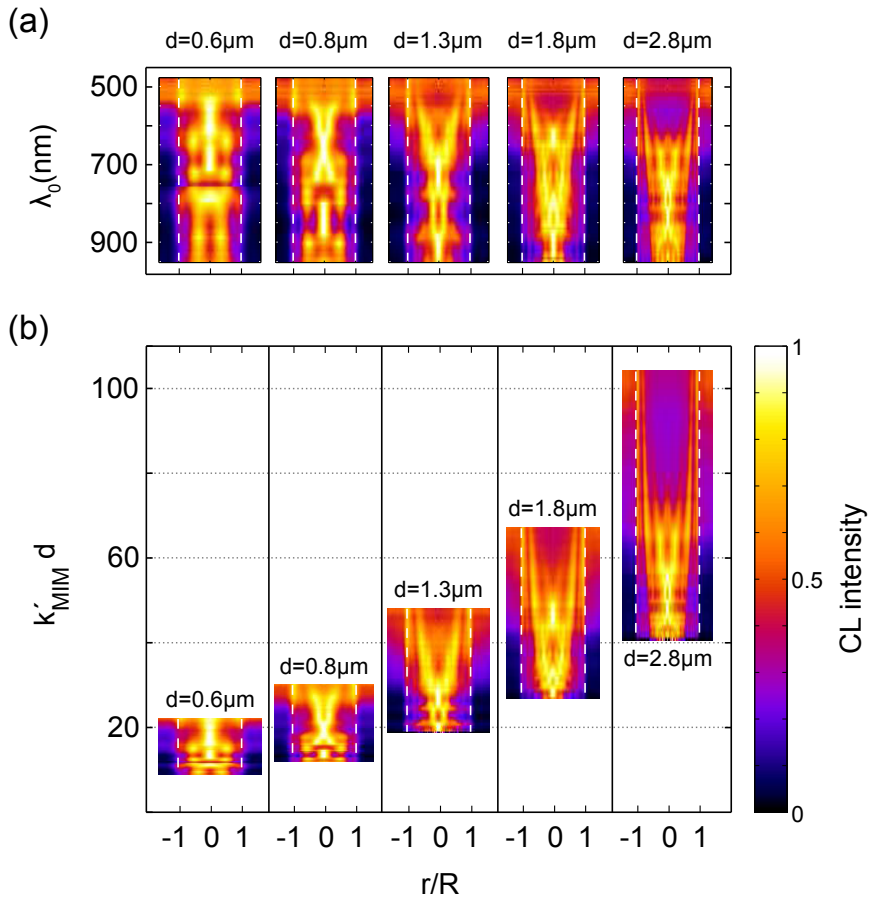

Figure 4.6: (a) Azimuthally averaged CL intensity maps as a function of wavelength and relative distance to the disk center for five disk sizes, 0.6 μm, 0.8 μm, 1.3 μm, 1.8 μm, 2.8 μm. (b) CL intensity maps with normalized wavenumber for different disk diameters corresponding to (a). CL intensity data are corrected for the background (typically around 100 cts/px/0.25 s) and the system response, and are normalized to unity at each disk size. The maximum counts of the raw map data before correction are equal to 1390, 1030, 990, 630, and 960 cts/px/0.25 s for increasing disk sizes, respectively.

out in the theory by García de Abajo and Kociak [31]. Fundamentally, it would be interesting to compare a full numerical evaluation of the theory by García de Abajo and Kociak [31] for CL with the the full numerical evaluation of the Purcell factor that we report here, to assess why the Purcell factor does, but CL does not, trace the simple model by Filter et al. [22]. Unfortunately, such a calculation appears prohibitively difficult, given that just mapping the Purcell factor in a single plane already requires

on the order of several days of computation. In experiment, incoherent background radiation such as fluorescence emission of the silica layer can also contribute to the collected CL intensity. Incoherent background radiation should not be expected to give a featureless background. Rather, also fluorescence generated incoherently in the patch spacer can result in a spatially dependent, and patch-size dependent brightness, since the brightness of incoherent, inefficient sources inside a photonic system will trace out its orientation-averaged radiative LDOS. Finally, inaccuracies in fabrication such as edge roughness evident in the SEM micrograph (Figure 4.1b) can influence the experimentally measured data.

4.5 Angular emission patterns

Metal-insulator-metal patch antennas were first proposed for their large directivity. Fluorescence experiments have examined the directivity for single quantum dots for select quantum dot positions and disk sizes [18]. Cathodoluminescence provides a unique opportunity to map the directivity in a well-normalized fashion both as function of disk size and as function of where the system is excited. Moreover, the well-defined polarization and coherence of the induced transition dipole facilitates the interpretation and modeling of the radiation pattern as will be discussed in this section.

Angular radiation patterns of the patch antennas are obtained by directly projecting the CL radiation collected by the parabolic mirror on to an imaging CCD where each pixel corresponds to a unique emission angle (Figure 4.4). A simple coordinate transformation [20] allows to convert raw CCD images into polar (θ, φ) diagrams. Figure 4.7a shows the measured angular radiation patterns of patch antennas for different disk diameters and detection wavelengths, in each case with e-beam excitation at the disk center. Here, the disk diameter increases from left to right and the detection wavelength increases from top to bottom. Due to the symmetry of the structure and the excitation, radiation patterns are expected to be symmetric around the axis normal to the sample ($\theta = 0°$, center in each polar diagram). However, for some measurements, asymmetry arises due to the finite number of e-beam positions (around 18 to 25 points along the disk diameter) which might not coincide exactly with the disk center. Overall, the radiation patterns show a strong dependence on the disk diameter and detection wavelength. Notably, the radiation patterns generally become more directional with decreasing wavelength and increasing disk size, commensurate with the notion that the diffraction pattern of a coherently emitting disk of size d has a radiation pattern spread over an angle d/λ. The most directional radiation patterns show beam widths of order 30°. Moreover, the shorter-wavelength/larger-disk regime is accompanied by the emergence of sidelobes at larger angle. In addition, we note that a doughnut-like structure for the central lobe is evident for some data sets which are similar to the emission pattern of vertical dipoles at interfaces.

A clear correlation between the appearance of a doughnut-like pattern and the size of the disk or the detection wavelength is not immediately apparent in our experimental data. We note that a doughnut-like symmetry would be expected quite rigorously

from symmetry in a fully coherent excitation experiment. Indeed, if one excites a cylindrically symmetric structure at its symmetry point with a z-oriented dipole, a decomposition of the emitted radiation into radial and azimuthal contributions must have zero azimuthal content. Any nonzero content would indicate a preferred handedness, or a preferred in-plane linear polarization which are both absent by symmetry. Since the emitted radiation must be radially polarized, one expects a null in the normal direction. Indeed, this notion is consistent with the null observed in previous CL experiments for transition radiation, excitation of small plasmon disks, and also with the radiation patterns calculated in Ref. [18] for patch antennas. Radiation in the center of the polar images hence points at either symmetry-breaking in the excitation and light out-coupling of the structure, or to the presence of incoherent in-plane polarized contributions to the CL signal, such as fluorescence generated in the silica spacer layer.

In an attempt to classify the reported radiation patterns and correlate the presence or absence of a central minimum to the degree to which an incoherent contribution is present in the sample, we have attempted to classify frequency/wavelength combination as being on or off resonance according to the measured excitability maps. We expect those patterns measured on resonance to show a clear minimum at the normal radiation angle as consistent with the coherent excitation and outcoupling of the MIM mode, while for patterns taken at an off resonance combination we expect a stronger incoherent component. While not all 19 frequency/diameter combinations plotted in Figure 4.7 can be uniquely assigned as being exactly on or off resonance, we could assign four combinations as clearly on, and seven as clearly off a resonance. Indeed, according to the CL maps of Figure 4.6, we can identify $\lambda = 900\,\mathrm{nm}$ at $d = 1.3\,\mu\mathrm{m}$ and $d = 1.8\,\mu\mathrm{m}$, as well as the combinations $d = 0.6\,\mu\mathrm{m}$ and $\lambda = 700\,\mathrm{nm}$ and $d = 1.8\,\mu\mathrm{m}$ and $\lambda = 600\,\mathrm{nm}$ as combinations for which the CL maps clearly show strong peak for excitations at the center of the disk. The corresponding radiation patterns of these four combinations are indicated by colored thick dotted squares surrounding the data in Figure 4.7a and the corresponding 2D cross-cuts are plotted in Figure 4.7b. Notably for these combinations, radiation patterns indeed clearly present a doughnut-like symmetry. On the other hand, we identified combinations for which CL maps of Figure 4.6 show clear minima at the center of the disk. These 'off-resonant' disk combinations are indicated by thin black dotted lines in Figure 4.7a. In contrast to the 'on-resonant' combinations, here the radiation patterns have peaks in the normal direction. Taking into account that for these combinations the mode feeding happens indirectly, this suggests that incoherent radiation processes are responsible for obscuring doughnut features from the radiation patterns. That the presence of the doughnut feature is sensitive to nonidealities in disk shape, disk-source alignment or incoherent background contributions while still showing overall directivity is commensurate with the fluorescence measurements by Belacel et al. [18] in which strong directivity but no central null in the radiation pattern of quantum dot clusters centered in the patch was found. In their work, they explained this by randomness in transition dipole orientation as well as positioning of the fluorophores.

As a measure of directivity of the patch antennas and in order to quantify the

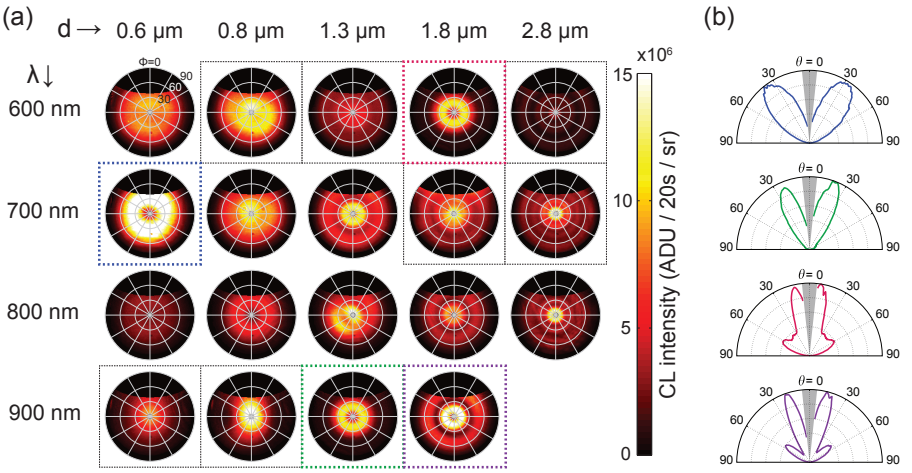

Figure 4.7: (a) Radiation patterns measured for different disk diameters (from left to right 0.6 μm, 0.8 μm, 1.3 μm, 1.8 μm, 2.8 μm) at different detection wavelengths (from top to bottom 600 nm, 700 nm, 800 nm, 900 nm) for e-beam excitation at the center of the disk. We have no measured data for 2.8 μm disk size at 900 nm. (b) 2D cross-cuts corresponding to patterns indicated by colored thick dotted boxes in (a).

radiated beam width of the patch antenna, we extracted the half width at half maximum (HWHM) values (ignoring the central null if present) from the 2D radiation patterns of Figure 4.7b and plotted sin(HWHM) as a function of the wavelength-normalized disk diameters (d/λ) in Figure 4.8. Here, measured values for different disk sizes are marked with different symbols and detection wavelengths are displayed by different colors. An overall decrease of the beam width is observed as the normalized disk size is increased which is in agreement with the expectation on basis of simple Fourier optics arguments whereby the beam divergence of radiation scales inversely with source size.

We find that radiation patterns of patch antennas strongly depend on the position of the excitation source. In order to explore the position dependence of the radiation pattern, we measured the radiation pattern for e-beam excitations along cuts through the patch antennas from the left edge to the center to the right edge for all disk diameters and detection wavelengths. Figure 4.9a shows the radiation pattern of a typical patch antenna ($d = 2.8$ μm, $\lambda = 700$ nm) for different e-beam excitation positions from the left edge to the center of the disk. The emission angle of the main lobe clearly tilts away from the normal direction as the excitation position is shifted away from the disk center, and varies from zenithal for central excitation to grazing, once the excitation reaches a point midway between center and edge excitation.

In order to better illustrate the beam steering of the patch antennas, for a selected set of disk diameters and detection wavelengths, we examined 2D cross-cuts (not shown) generated by averaging the radiation pattern over a 20 degrees azimuthal angles around $\phi = 90°$. We calculated the emission angle of the beam defined by the maximum

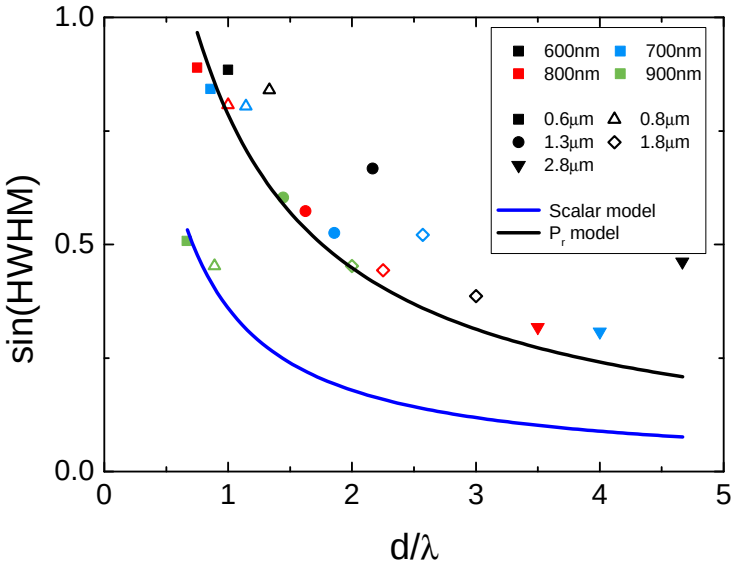

Figure 4.8: Beam width of the patch antennas defined as sin(HWHM) as a function of wavelength-normalized disk diameters. Symbols: measured beam width values. Lines: calculated beam width using scalar model (blue) and radially polarized dipole model (black).

lobe (θ_{max}) for disk sizes and wavelengths where beaming was pronounced at central excitation. We plot the results as a function of the excitation position r normalized to disk radius R in Figure 4.9b. The radiation angle depends linearly on the position of the e-beam excitation in a manner that is remarkably similar for all antenna and wavelength combinations. It should be noted that the plotted error bars do not indicate the error in determining θ_{max} but serve to indicate the width of the beam in θ. For each excitation position, wavelength, and disk size, we extracted the angular width of the beam by calculating the standard deviation of the radiation pattern around the main lobe. The results are depicted as error bars in Figure 4.9b and are also plotted separately in the inset of Figure 4.9b. The directionality of the beam is highest for excitation of the disk at the center and decreases for excitations away from the disk center. A qualitative explanation is that the radiation is due to excitation of MIM plasmons as a cylindrical wave emanating from the excitation point that scatter out into the far field at the disk edge. For central excitation the entire edge of the disk radiates coherently with equal amplitude. As the excitation approaches the edge of the disk, however, only a fraction of the edge close to the excitation point dominates the radiated signal. Thus, shifting towards the edge reduces the effective source size and hence directionality.

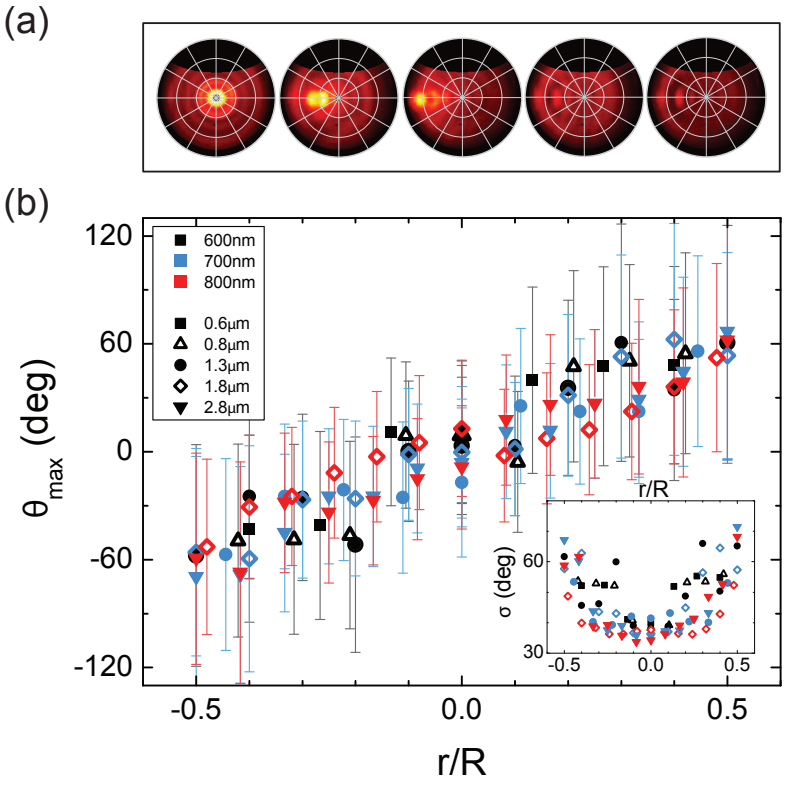

Figure 4.9: (a) Measured radiation pattern for different excitation positions for a typical patch antenna ($d = 2.8$ μm, $\lambda = 700$ nm). From left to right: e-beam excitation position at the center of the disk to the right edge of the disk. (b) Emission angle for a selected set of disk sizes and wavelengths as a function of normalized excitation distance from the disk center. Error bars indicate the angular width of the beam (standard deviation) with values plotted in the inset.

4.6 Simple model for angular emission patterns

In order to analytically calculate radiation patterns of the patch antennas, we used a model based on the interference of the scattered fields at the edge of the disks. In this model, we assume that the local excitation at $\mathbf{r}_0$ launches a cylindrical outgoing wave

$$\frac{e^{ik_{MIM}|\mathbf{r}-\mathbf{r}_0|}}{\sqrt{|\mathbf{r}-\mathbf{r}_0|}} \tag{4.5}$$

in the patch that scatterers out at the edge. In a simple analysis, the far field radiation pattern is the Fourier transform of the amplitude and phase pattern imprinted on the

disk edge. We will refer to this model as 'scalar' as it does not contain polarization effects. In full-wave COMSOL simulations we have observed that if one sets up a MIM mode in the disk, the E-field at the disk edge is mainly polarized in the radial direction (three to one ratio relative to vertical polarization). A first estimate of the radiation pattern with polarization effects included is hence to discretize the disk edge as radially oriented dipoles with amplitude and phase given according to Eq. (4.5). Figure 4.10a shows a set of measured radiation patterns ($d = 1.3\,\mu$m, $\lambda = 700$ nm) with Figure 4.10b and c showing the calculated radiation patterns for the radially polarized and scalar model. Reasonable correspondence is obtained in terms of the angle at which the central lobe occurs, its width, and the occurrence of side lobes at angles far from the main lobe. For comparison with experiment, calculated beam widths are plotted in Figure 4.8 for the scalar (blue line) and radially polarized dipole model (black line). A good agreement is observed with experiment for the radial model which is consistent with results from COMSOL simulations.

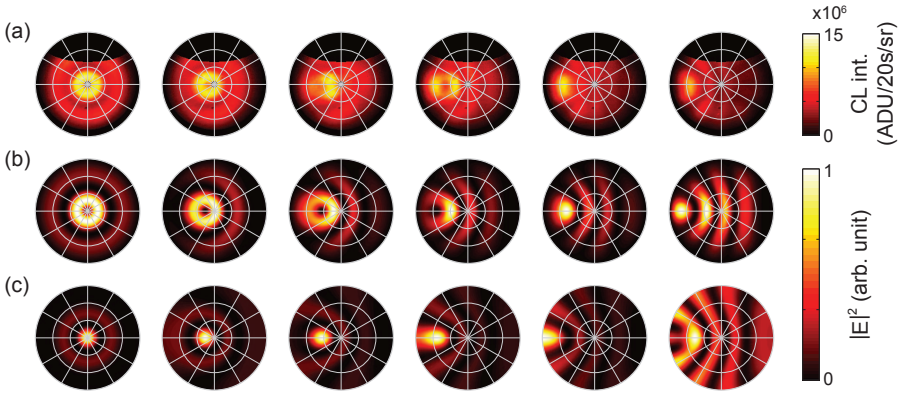

Figure 4.10: (a) Measured radiation pattern as a function of excitation position for a typical patch antenna ($d = 1.3\,\mu$m, $\lambda = 700$ nm). Calculated radiation patterns from (b) radially polarized dipole model and (c) scalar model. From left to right: e-beam excitation position at the center of the disk to the right mid-edge ($x = r/2$) of the disk.

At first sight it might seem surprising that such excellent correspondence for radiation patterns is obtained taking as model just the patch edge driven by the cylindrical outgoing wave of Eq. (4.5), without resorting at all to the complicated mode decomposition underlying the LDOS calculation. Explicit analysis shows that the mode decomposition, i.e., first projecting a local excitation at $\mathbf{r}_0$ into modes and then constructing radiation patterns by coherent superposition, likewise results in a good match to the observed radiation patterns. The physics resolving this seeming paradox is hidden in Figure 4.2b, which shows that especially large diameter disks support a large number of modes of various radial and azimuthal quantum numbers at any given frequency. The key physics is that the large number of modes supported by the disk is essentially a sufficiently complete set to build up the cylindrical wave assumed in

Eq. (4.5), similar to the notion in standard optics that increasingly big objects have increasingly complex mode structures yet ultimately can be described increasingly well by simple ray optics arguments.

4.7 Conclusion

To conclude, we have reported a comprehensive study of plasmonic patch antennas in which we have shown a strong excitation position dependence of the angle-integrated cathodoluminescence, as well as the dependence of directivity on antenna size, wavelength and driving position. As well, explained by an analytical model, patch antennas in the typical size regime for directional emission support a large number of overlapping modes of different angular and radial quantum numbers. For a dipole point source located in the MIM gap, the LDOS we find from full-wave simulations matches very well the analytical model based only on the symmetric MIM mode. We find that the CL maps, while qualitatively similar, quantitatively deviate, pointing at the fact that CL not solely excites the MIM mode. Angular radiation patterns measured for central excitation and on a resonance present strongly directional doughnut beams, exactly as expected from symmetry and as was predicted but not observed in previous reports [18]. Moreover, our observations show that even incoherently and indirectly excited luminescence couples out in a directional fashion, without the beam pattern minimum exactly in the normal direction. Finally, the beam directivity and beam steering as function of incident power is well explained without taking the mode structure into account at all, simply viewing the circular boundary as outcoupler for the cylindrical MIM wave launched by the CL excitation.

References

[1] L. Novotny and N. van Hulst, *Antennas for light*, Nat. Photon. **5**, 83 (2011).

[2] K. G. Lee, X. W. Chen, H. Eghlidi, P. Kukura, R. Lettow, A. Renn, V. Sandoghdar, and S. Götzinger, *A planar dielectric antenna for directional single-photon emission and near-unity collection efficiency*, Nat. Photon. **5**, 166 (2011).

[3] K. Vahala, *Optical microcavities*, volume 5 of *Advanced series in applied physics*, World Scientific, 2004.

[4] D. Englund, D. Fattal, E. Waks, G. Solomon, B. Zhang, T. Nakaoka, Y. Arakawa, Y. Yamamoto, and J. Vučković, *Controlling the spontaneous emission rate of single quantum dots in a two-dimensional photonic crystal*, Phys. Rev. Lett. **95**, 013904 (2005).

[5] S. Noda, M. Fujita, and T. Asano, *Spontaneous-emission control by photonic crystals and nanocavities*, Nat. Photon. **1**, 449 (2007).

[6] A. G. Curto, G. Volpe, T. H. Taminiau, M. P. Kreuzer, R. Quidant, and N. F. van Hulst, *Unidirectional emission of a quantum dot coupled to a nanoantenna*, Science **329**, 930 (2010).

[7] R. de Waele, A. F. Koenderink, and A. Polman, *Tunable nanoscale localization of energy on plasmon particle arrays*, Nano Lett. **7**, 2004 (2007).

[8] A. F. Koenderink, *Plasmon nanoparticle array waveguides for single photon and single plasmon sources*, Nano Lett. **9**, 4228 (2009).

[9] T. Kosako, Y. Kadoya, and H. F. Hofmann, *Directional control of light by a nano-optical yagi-uda antenna*, Nat. Photon. **4**, 312 (2010).

[10] F. Bernal Arango, A. Kwadrin, and A. F. Koenderink, *Plasmonic antennas hybridized with dielectric waveguides*, ACS Nano **6**, 10156 (2012).

[11] H. Aouani, O. Mahboub, E. Devaux, H. Rigneault, T. W. Ebbesen, and J. Wenger, *Plasmonic antennas for directional sorting of fluorescence emission*, Nano Lett. **11**, 2400 (2011).

[12] J.-M. Yi, A. Cuche, E. Devaux, C. Genet, and T. W. Ebbesen, *Beaming visible light with a plasmonic aperture antenna*, ACS Photonics **1**, 365 (2014).

[13] L. Langguth, D. Punj, J. Wenger, and A. F. Koenderink, *Plasmonic band structure controls single-molecule fluorescence*, ACS Nano **7**, 8840 (2013).

[14] S. R. K. Rodriguez, G. Lozano, M. A. Verschuuren, R. Gomes, K. Lambert, B. De Geyter, A. Hassinen, D. Van Thourhout, Z. Hens, and J. Gómez Rivas, *Quantum rod emission coupled to plasmonic lattice resonances: A collective directional source of polarized light*, Appl. Phys. Lett. **100**, 111103 (2012).

[15] B. Rolly, B. Stout, and N. Bonod, *Boosting the directivity of optical antennas with magnetic and electric dipolar resonant particles*, Opt. Express **20**, 20376 (2012).

[16] T. Coenen, F. Bernal Arango, A. F. Koenderink, and A. Polman, *Directional emission from a single plasmonic scatterer*, Nat. Commun. **5**, 3250 (2014).

[17] R. Esteban, T. V. Teperik, and J. J. Greffet, *Optical patch antennas for single photon emission using surface plasmon resonances*, Phys. Rev. Lett. **104**, 026802 (2010).

[18] C. Belacel, B. Habert, F. Bigourdan, F. Marquier, J.-P. Hugonin, S. Michaelis de Vasconcellos, X. Lafosse, L. Coolen, C. Schwob, C. Javaux, B. Dubertret, J.-J. Greffet, P. Senellart, and A. Maitre, *Controlling spontaneous emission with plasmonic optical patch antennas*, Nano Lett. **13**, 1516 (2013).

[19] D. T. Schoen, T. Coenen, F. J. García de Abajo, M. L. Brongersma, and A. Polman, *The planar parabolic optical antenna*, Nano Lett. **13**, 188 (2013).

[20] T. Coenen, E. J. R. Vesseur, and A. Polman, *Angle-resolved cathodoluminescence spectroscopy*, Appl. Phys. Lett. **99**, 143103 (2011).

[21] R. Sapienza, T. Coenen, J. Renger, M. Kuttge, N. F. van Hulst, and A. Polman, *Deep-subwavelength imaging of the modal dispersion of light*, Nature Mat. **11**, 781 (2012).

[22] R. Filter, J. Qi, C. Rockstuhl, and F. Lederer, *Circular optical nanoantennas: an analytical theory*, Phys. Rev. B **85**, 125429 (2012).

[23] F. Minkowski, F. Wang, A. Chakrabarty, and Q.-H. Wei, *Resonant cavity modes of circular plasmonic patch nanoantennas*, Appl. Phys. Lett. **104**, 021111 (2014).

[24] P. B. Johnson and R. W. Christy, *Optical constants of the noble metals*, Phys. Rev. B **6**, 4370 (1972).

[25] J. A. Dionne, E. Verhagen, A. Polman, and H. A. Atwater, *Are negative index materials achievable with surface plasmon waveguides? a case study of three plasmonic geometries*, Opt. Express **16**, 19001 (2008).

[26] H. T. Miyazaki and Y. Kurokawa, *Squeezing visible light waves into a 3-nm-thick and 55-nm-long plasmon cavity*, Phys. Rev. Lett. **96**, 097401 (2006).

[27] H. T. Miyazaki and Y. Kurokawa, *Controlled plasmon resonance in closed metal/insulator/metal nanocavities*, Appl. Phys. Lett. **89**, 211126 (2006).

[28] M. Kuttge, W. Cai, F. J. García de Abajo, and A. Polman, *Dispersion of metal-insulator-metal plasmon polaritons probed by cathodoluminescence imaging spectroscopy*, Phys. Rev. B **80**, 033409 (2009).

[29] E. M. Purcell, *Spontaneous emission probabilities at radio frequencies*, Phys. Rev. **69**, 681 (1946).

[30] M. Kuttge, F. J. García de Abajo, and A. Polman, *Ultrasmall mode volume plasmonic nanodisk resonators*, Nano Lett. **10**, 1537 (2010).

[31] F. J. García de Abajo and M. Kociak, *Probing the photonic local density of states with electron energy loss spectroscopy*, Phys. Rev. Lett. **100**, 106804 (2008).

[32] W. A. Harrison, *Solid state theory*, Dover Publications, New York, 1979.

[33] P. G. Etchegoin, E. C. Le Ru, and M. Meyer, *An analytic model for the optical properties of gold*, J. Chem. Phys. **125**, 164705 (2006).

[34] F. J. García de Abajo, *Optical excitations in electron microscopy*, Rev. Mod. Phys. **82**, 209 (2010).

[35] J. T. van Wijngaarden, E. Verhagen, A. Polman, C. E. Ross, H. J. Lezec, and H. A. Atwater, *Direct imaging of propagation and damping of near-resonance surface plasmon polaritons using cathodoluminescence spectroscopy*, Appl. Phys. Lett. **88**, 221111 (2006).

[36] W. Cai, R. Sainidou, J. Xu, A. Polman, and F. J. García de Abajo, *Efficient generation of propagating plasmons by electron beams*, Nano Lett. **9**, 1176 (2009).

[37] T. Coenen, E. J. R. Vesseur, and A. Polman, *Deep subwavelength spatial characterization of angular emission from single-crystal au plasmonic ridge nanoantennas*, ACS Nano **6**,

1742 (2012).

[38] E. S. Barnard, T. Coenen, E. J. R. Vesseur, A. Polman, and M. L. Brongersma, *Imaging the hidden modes of ultrathin plasmonic strip antennas by cathodoluminescence*, Nano Lett. **11**, 4265 (2011).

5

K-space polarimetry on fluorescent plasmonic antennas

We present a new method to completely map the polarization state of light emitted by, or scattered from, single nanostructures located in the focus of a high NA objective as function of any emission angle in the objective back focal plane. In particular, we use a so-called Fourier microscope that is based on back-focal plane imaging in combination with a simple polarimeter to measure Stokes-parameters for each point in the back-focal plane image. We apply k-space polarimetry to measure the polarization state of the light emitted into the far-field by fluorophores inside a so-called bull's eye antenna, meaning that they are located inside a nano-aperture in a gold film, that is surrounded by a set of concentric grooves. We show that, despite the fact that we deal with an orientationally random ensemble of emitters, the fluorescence shows a degree of polarization, that is imparted on it through interaction with surface plasmon polaritons that mediate the outcoupling. In particular, we can determine the full polarization ellipse for the fully polarized part of the emission, i.e., emission that appears in the far field only after having been redirected by the bull's eye structure. We also perform numerical simulations to model the radiation patterns of the plasmonic antennas, and present preliminary measurements on spiral antennas.

5.1 Introduction

Full control over the emission of fluorophores would entail control over the rate of emission, control over the angular distribution of emitted intensity, and control over the relative phase and amplitude of the different vector components of the emitter light. The first type of control requires manipulation of the local density of states (LDOS), studied in Chapters 3 and 4, and can be reached using a variety of narrowband strategies (notably microcavity Purcell enhancements) and broadband structures, notably including plasmonic nanoparticles and surfaces. The second type of control, i.e., control over angular distribution of emitted intensity relies on engineering a geometry such that part, or all, of the emission of a point-like emitter excites a wavelength-sized structure, that subsequently acts as a phased arrangement of secondary sources that are mutually coherent, and coherent with the source dipole. This was demonstrated already in 2000 for single molecules coupled to scanning probe tips [1], and later developed into phased-array engineering as in the radio frequency domain. This philosophy of phased-array engineering is especially evident in the famous Yagi-Uda plasmonic array antenna proposed in Refs. [2–4] and realized in Refs. [5, 6], but equally underlies the strong directivity obtained with diffractive plasmonic lattices [7–9], the directivity offered by plasmonic patch antennas [10] in Chapter 4, and the directivity of the plasmonic bull's eye antenna pioneered by Lezec et al. [11], and in context of fluorescence pursued strongly by the team of Wenger [12–17]. The third type of control, i.e., complete control over the polarization state of emitted light is a comparatively less explored field. With the advent of metasurfaces and metamaterials, it has become evident that carefully shaped structures can simultaneously, although not independently, control the electric and magnetic components of the near-field around an emitter [18]. Conversely, it has also been proposed that magnetoelectric scatterers, when excited locally by an electric dipole source, can generate handed far-field emission [19]. Thus a new emerging field in nanophotonics is to couple emitters to chiral and nonchiral plasmonics structures, with the desire to simultaneously control phasefront and polarization. This corresponds to engineering the orbital angular momentum [20] (encoded in distribution of phase) and spin angular momentum (encoded in polarization) of directional beams emitted by single point sources [21–25].

With the efforts to control the full wavevector-resolved polarization state of light emitted by nanoscale sources through nanophotonic structures, comes the need for experimental techniques to resolve their performance. In chapter 4, we presented results obtained using a technique suited for angle-resolved mapping of intensity using back-aperture imaging, in that case in the back-aperture of a parabolic collection mirror. This is a variant of a technique first developed in fluorescence microscopy, where a very accurate wavevector-resolved intensity map is realized by the so-called back-focal plane imaging, or Fourier imaging in a high NA microscope [26], which was later used in plasmonic scattering contexts by several workers for single-antenna fluorescence [5, 16, 17, 27] and scattering [28]. By imaging the back focal plane of an objective onto a silicon CCD chip, the entire wavevector content of light emitted or scattered by an object can be resolved with high angular resolution, typically of order

one degree, and over a very large solid angle, namely the entire objective NA, in a setup without any moving parts. Due to the aplanatic design constraint on microscope objectives, this type of back focal plane imaging provides a direct mapping of the in-plane wavevector $\mathbf{k}_{||}$. Here we extend this technique with a Stokes polarimeter to map the full polarization state of the light at any given emission angle. Our measurements on fluorophores in plasmonic bull's eye antennas highlight the capability of our method to map all polarization degrees of freedom for a very large set of emitted wavevectors, with sensitivity sufficient to even potentially reach to the single emitter level.

5.2 k-space polarimetry principles

For a transverse electromagnetic wave propagating along the z-axis, the polarization is defined according to the relation between the transverse components of the electric field, i.e. $E_x(r,t)$ and $E_y(r,t)$. When the light is fully polarized, this relation is well-defined and can be described by the Jones vector $\boldsymbol{J}$ as [29, 30]:

$$\boldsymbol{J} = \begin{pmatrix} E_x \\ E_y \end{pmatrix} = \begin{pmatrix} E_{0x}\, e^{i\phi_x} \\ E_{0y}\, e^{i\phi_y} \end{pmatrix}, \tag{5.1}$$

where, E_{0x} and E_{0y} are the amplitude, and ϕ_x and ϕ_y are the phase of the electric field in x and y directions, respectively. This Jones vector completely specifies the ellipticity, handedness, and orientation of the polarization ellipse. However, when the light is only partially polarized, meaning that the relation between the components of the electric field is no longer fully deterministic but shows fluctuations so rapid as to be unresolvable in measurement, the two-element Jones vector is no longer sufficient for describing the full polarization state of the light. We note that partial polarization is a statistical concept and arises due to incoherent superposition of different polarization states that each individually can be described by a Jones vector [29, 30]. In other words, one can describe partially polarized light, as random variations of the Jones vector whose degree of polarization is characterized by its coherency (covariance) matrix $\mathbf{c}$, defined as

$$\mathbf{c} = \langle \boldsymbol{J} \otimes \boldsymbol{J}^{\dagger} \rangle = \begin{pmatrix} \langle E_x E_x^* \rangle & \langle E_x E_y^* \rangle \\ \langle E_y E_x^* \rangle & \langle E_y E_y^* \rangle \end{pmatrix} = \begin{pmatrix} \langle |E_x|^2 \rangle & \langle E_x E_y^* \rangle \\ \langle E_y E_x^* \rangle & \langle |E_y|^2 \rangle \end{pmatrix}, \tag{5.2}$$

where $\boldsymbol{J}^{\dagger}$ is the Hermitian transpose of $\boldsymbol{J}$ and brackets denote temporal averaging. The coherency matrix contains full information on the polarization state of the light. However, from eq. 5.2 it is not immediately apparent what measurable physical quantities are needed for full description of the polarization state. In order to better visualize the coherency matrix, it is customary to decompose it into a set of Hermitian basis matrices as

$$\mathbf{c} = \frac{1}{2} \sum_{k=0}^{3} S_k \boldsymbol{\sigma}_k \tag{5.3}$$

where $\boldsymbol{\sigma}_0$ is the 2×2 unit matrix, $\boldsymbol{\sigma} = (\boldsymbol{\sigma}_1, \boldsymbol{\sigma}_2, \boldsymbol{\sigma}_3)$ are the Pauli matrices defined as

$$\boldsymbol{\sigma}_1 = \begin{pmatrix} 1 & 0 \\ 0 & -1 \end{pmatrix}, \quad \boldsymbol{\sigma}_2 = \begin{pmatrix} 0 & 1 \\ 1 & 0 \end{pmatrix}, \quad \boldsymbol{\sigma}_3 = \begin{pmatrix} 0 & -i \\ i & 0 \end{pmatrix},$$

and $\boldsymbol{S} = (S_0, S_1, S_2, S_3)$ is the Stokes polarization vector. We can rewrite the Stokes parameters in terms of the elements of the coherency matrix as

$$S_k = \mathrm{tr}(\boldsymbol{\sigma}_k \mathfrak{c}). \tag{5.4}$$

This gives the Stokes vector as

$$\boldsymbol{S} = \begin{pmatrix} S_0 \\ S_1 \\ S_2 \\ S_3 \end{pmatrix} = \begin{pmatrix} \langle |E_x|^2 \rangle + \langle |E_y|^2 \rangle \\ \langle |E_x|^2 \rangle - \langle |E_y|^2 \rangle \\ \langle E_x E_y^* \rangle + \langle E_y E_x^* \rangle \\ i(\langle E_x E_y^* \rangle - \langle E_y E_x^* \rangle) \end{pmatrix}. \tag{5.5}$$

We note that S_0 corresponds to the total intensity of the electric field. One can show that all the Stokes parameters presented in eq. 5.5 are directly related to measurable physical quantities, i.e. sums and differences of the electric field intensities. To show that, let us consider intensity measurements through a set of polarizers vectorially defined by

$$\begin{aligned} \mathbf{P}_H &= \begin{pmatrix} 1 \\ 0 \end{pmatrix}, & \mathbf{P}_V &= \begin{pmatrix} 0 \\ 1 \end{pmatrix}, \\ \mathbf{P}_+ &= \tfrac{1}{\sqrt{2}} \begin{pmatrix} 1 \\ 1 \end{pmatrix}, & \mathbf{P}_- &= \tfrac{1}{\sqrt{2}} \begin{pmatrix} 1 \\ -1 \end{pmatrix}, \\ \mathbf{P}_R &= \tfrac{1}{\sqrt{2}} \begin{pmatrix} 1 \\ i \end{pmatrix}, & \mathbf{P}_L &= \tfrac{1}{\sqrt{2}} \begin{pmatrix} 1 \\ -i \end{pmatrix}. \end{aligned} \tag{5.6}$$

Given the instantaneous Jones vector $\mathbf{J} = (E_x, E_y)$, the detected signal through a polarizer $\mathbf{P}$ on a detector that measures intensity averaged over a time longer than the typical fluctuation time of the field reads $\langle |P^* \cdot \mathbf{J}|^2 \rangle$. Thereby the detected intensities will correspond to:

$$\begin{aligned} I_H = \langle |E_x|^2 \rangle \quad \text{and} \quad I_V &= \langle |E_y|^2 \rangle \\ I_\pm = \langle |E_x \pm Ey|^2 \rangle &= \tfrac{1}{2}[\langle |E_x|^2 \rangle + \langle |E_y|^2 \rangle \pm \langle 2\mathrm{Re} E_x^* E_y \rangle] \\ I_{R,L} = \langle |E_x \pm iEy|^2 \rangle &= \tfrac{1}{2}[\langle |E_x|^2 \rangle + \langle |E_y|^2 \rangle \pm \langle 2\mathrm{Im} E_x^* E_y \rangle] \end{aligned} \tag{5.7}$$

Practically, these intensities I represent the detected intensity for specific polarizer settings denoted by the subscripts: H and V for horizontal and vertical linear polarizations, $+$ and $-$ for diagonal ($45°$) and anti-diagonal ($-45°$) linear polarizations, and R and L for right-handed and left-handed circular polarizations. Using the definitions of eq. 5.7, one can show that the Stokes parameters in eq. 5.5 can be written as sums and differences of the electric field intensities as:

$$\begin{aligned} S_0 &= I_H + I_V &\equiv\ & I_{0,0} + I_{90,90} \\ S_1 &= I_H - I_V &\equiv\ & I_{0,0} - I_{90,90} \\ S_2 &= I_+ - I_- &\equiv\ & I_{45,45} - I_{135,135} \\ S_3 &= I_R - I_L &\equiv\ & I_{0,45} - I_{0,135} \end{aligned} \tag{5.8}$$

We note that all the quantities required to construct Stokes parameters are measurable intensities in our experiments *per wavevector* in our Fourier microscope. In order to measure the above specific intensities, we construct a polarimeter using a quarter-wave plate (QWP) followed by a linear polarizer (LP) (section 5.3). By aligning the axes of each element in different combinations, we can realize any required polarization selection. This alignment combination is indicated in eq. 5.8 by the subscripts of the intensity $I_{\alpha,\beta}$, where α and β denote the rotation angle of the QWP and the LP with respect to the x-axis.

Finally, we note that the Stokes parameters allow to retrieve many useful derived quantities, such as the degree of polarization, the degree of linear polarization, and the degree of circular polarization. Also, for the purely polarized contribution to the total signal, the Stokes parameters allow to reconstruct the polarization ellipse parameters

$$\begin{aligned} \epsilon &= S_3 / \sqrt{S_1^2 + S_2^2} \\ \alpha &= 1/2 \arg(S_1 + iS_2). \end{aligned} \tag{5.9}$$

Here, $-1 \leq \epsilon \leq 1$ represents the ellipticity as the ratio of semiminor to semimajor axis and the helicity through the sign of ϵ, and $-\pi/2 < \alpha < \pi/2$ represents the orientation of the ellipse major axis relative to the x-axis. We note that this definition is equivalent to the common literature definition of α through use of arctan rather than arg, but that in contrast to $\arctan(S_2/S_1)$, the function $\arg(S_1 + iS_2)$ always returns angle in the correct quadrant.

5.3 Experimental setup

Figure 5.1(a) shows a schematic of the experimental setup, that is based on the set up of Sersic et al [28], yet modified to deal with fluorescence rather than scattering. The setup is composed of an imaging fluorescence microscope with an optional Fourier transforming lens on a flip mount that images the back focal plane of the objective on the CCD camera. As excitation light source, we used a broadband super-continuum laser (Fianium) from which the excitation wavelength is selected through an acousto-optical tunable filter (AOTF) followed by a cleaning bandpass filter (680±10 nm). The excitation laser is guided to the setup using a single mode optical fiber and is subsequently collimated through an achromatic lens. The input polarization of the light is set by a linear polarizer and a quarter-wave plate. Using an achromatic lens, the incoming laser light is weakly focused on the back of the sample and through the glass substrate. The fluorescence light is then collected by a 60× objective (NA=0.7, Nikon CFI Plan Fluor) from the other side of the sample and is guided through a telescope equipped with a pinhole in a real space image plane to spatially select the light coming solely from a region of interest on the sample. Given the $f_{\text{telescope}} = 50$ mm focal length lenses of the 1:1 telescope, the 300 μm pinhole corresponds to a selected area of about 20 μm across on the sample. In order to observe the fluorescence emission, the excitation laser light is filtered out using a 690 nm long-pass filter. A second

40 nm-width bandpass filter (700 nm or 750 nm) is used to select a desired part of the broad fluorescence spectrum. Finally, a polarimeter consisting of a quarter-wave plate and a linear polarizer is placed before the $f = 200$ mm tube lens and the silicon CCD camera (Photometrics CoolSnap EZ). The Fourier lens itself has a focal length of $f_{\text{Fourier}} = 200$ mm and is placed at a distance $f_{\text{Fourier}} + 4 f_{\text{telescope}}$ behind the back focal plane (just after the telescope), yielding a magnification of 1 for back focal plane imaging.

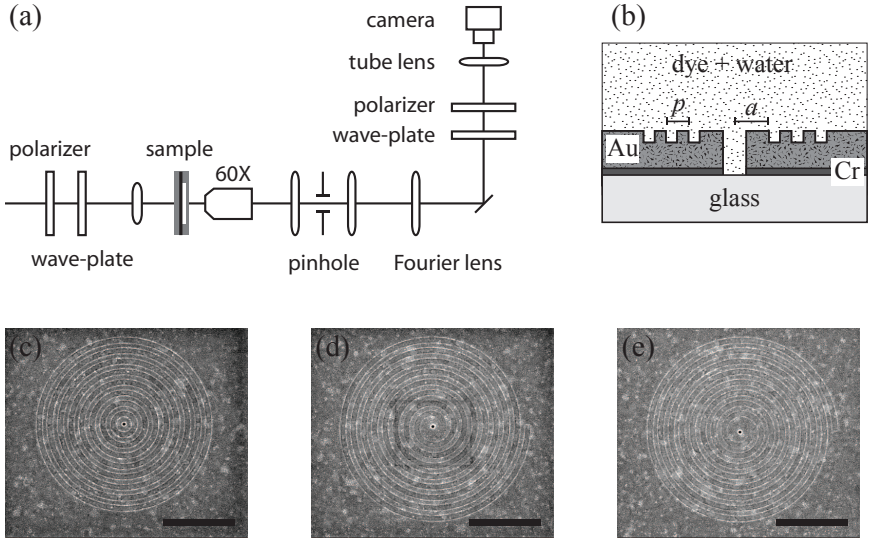

Figure 5.1: (a) Schematic of the fluorescence Fourier microscope setup equipped with polarimeter. (b) Schematic of the sample containing the plasmonic nano-antenna in the flow-cell. (c-e) Scanning electron micrographs of the fabricated (c) bull's eye, (d) left-handed spiral and (e) right-handed spiral plasmonic nano-antennas. The micrographs represent structures of pitch $p = 600$ nm. Scale bars represent 3μm. Nano-antennas with $p = 440$ nm are also fabricated (micrographs not presented here).

Our sample consists of plasmonic nano-antennas of different geometries. Figure 5.1(b) schematically shows the cross-sectional structure of our sample. To fabricate the sample, we evaporated a 5 nm thick layer of chromium followed by a 200 nm thick layer of gold on top of a glass coverslip. The thin chromium layer is used to improve the adhesion of the gold layer to the glass substrate. We fabricated the antenna structures by milling ~50 nm deep trenches into the gold layer. At the center of each antenna, we milled a 200 nm diameter hole that passes all the way to the glass substrate. We fabricated bull's eye, left-handed and right-handed spiral antennas (figure 5.1(c-e), respectively) at two different pitches: $p = 440$ nm and $p = 600$ nm. The distance from the center of the hole to the first pitch is a, which is chosen as a fraction of the pitch (specified below). The spiral structures are fabricated based on

the equation for Archimedean spirals, which are defined in polar coordinates (r, φ) as: $r = a + p(n + l\varphi/(2\pi))$. Here, a is the separation of the first groove from the center of the structure, p is the pitch, l is a fixed nonnegative integer specifying the total number of arms in a spiral, and the formula is evaluated for $n = 0, 1, \ldots, N-1$ to obtain N windings. We use $N = 8$ and $l = \pm 1$ to obtain single-armed spirals with 8 windings. For all the structures, the width of the trenches are half of the pitch. For the reference measurement, we also fabricated single holes of the same diameter as in the antennas, with no structures around. Finally, we built an open flow-cell on top of the structures using a few hundred micrometer thick polymer film spacer (Parafilm) sandwiched between the sample and another glass coverslip.

As fluorescence sources, we filled the flow cell with 'Alexa Fluor 700' dye molecules dissolved in water at a concentration of 10 μM. The dye has an emission peak at 723 nm with an emission full-width at half-maximum of about 50 nm. After filling the flow-cell with the dye solution, we illuminate the sample from behind and through the glass substrate. The incoming laser light (with power about 10 μW) excites the dye molecules residing mainly in the hole, as evidenced by FCS studies of dyes in nanoapertures [13, 14, 16, 27]. Part of the emitted photons from the fluorescent molecules couple to surface plasmon polaritons (SPPs) which propagate away from the central hole. Subsequently, the SPPs scatter out into the far-field at the edges of the corrugated antenna structure and can be detected by the CCD camera. The exposure time is about 40 s to 60 s depending on the structure, using approximately 10 μW of pump power.

5.4 Experimental results

We measured the k-space distribution of fluorescence emission of the antennas for two sets of structures with different pitches: $p = 440$ nm with $a = (3/4)p = 330$ nm and $p = 600$ nm with $a = p = 600$ nm, where a is the separation of the first groove from the center of the structure. Each set of structures consists of three different geometries: bull's eye (abbrev. BE), left-handed spiral (abbrev. LS) and right-handed spiral (abbrev. RS) antennas. We measured the emission pattern of all six structures at two emission wavelengths, 700 nm and 750 nm, selected by bandpass filters (section 5.3). As reference, we also measured the radiation pattern of single holes with no antenna structures. For convenience, hereafter, we refer to the structures with pitch $p = 440$ nm and $p = 600$ nm, by numeral symbols 1 and 2, respectively (e.g. BE1 as bull's eye with $p = 440$ nm). We focus on presenting data for the bull's eye structure first. For each structure, we measured the k-space distribution of the fluorescence emission at the six different configurations of the polarimeter needed to retrieve the Stokes parameters as described in section 5.1: I_H, I_V, I_+, I_-, I_R, I_L.

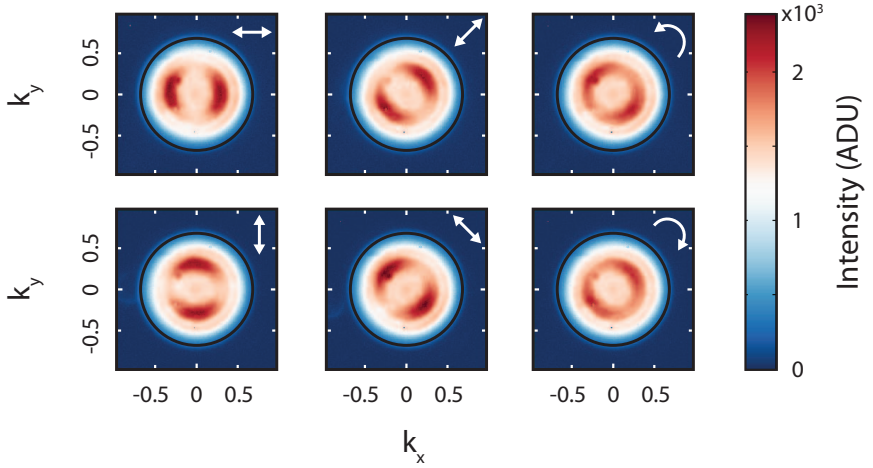

Figure 5.2: Measured k-space distribution of the fluorescence emission from BE2 at emission wavelength of 700 nm for six different polarimeter settings needed to retrieve the Stokes parameters . For this measurement circular input polarization for the pump laser is used.

5.4.1 K-space polarimetry measurements for bull's eye structure: intensity S_0

Figure 5.2 shows the results of a typical measurement for BE2 structure at 700 nm. Here, each measurement corresponds to a specific setting of the polarimeter which is labeled and depicted by an arrow in the inset of each plot. For all the measurements, we subtracted a background measured with the input laser light being blocked. Each radiation pattern appears as a disk in which the center corresponds to emission along the objective optical axis, and with outer rim corresponding to the objective NA of 0.7. The wavevector emerging from the object on the sample side in spherical coordinates as $\mathbf{k} = |k|(\cos\varphi\sin\theta, \sin\varphi\sin\theta, \cos\theta)$, after the objective is mapped to the back focal plane such that the azimuthal coordinate in the disk directly maps φ, while the radial distance from center to edge corresponds to going from optical axis to edge in direct proportion to $|\mathbf{k}_{||}|$, i.e., to $\sin\theta$. The scaling is exactly given by the objective focal length.

For these measurements we have set the excitation polarization of the incoming laser to circular. Given the cylindrically symmetric nature of sample plus excitation, this input polarization ensures that we create a cylindrically symmetric spatial distribution of pump field energy density. If one assumes that fluorophores retain no memory of their pump polarization, one thus expects that this experiment provides a cylindrically symmetric fluorescence output. We return to the role of input polarization in section 5.4.3. Importantly, through any given linear polarization setting, the radiation pattern is not cylindrically symmetric, but rather peaks in lobes along the polarization direction. This

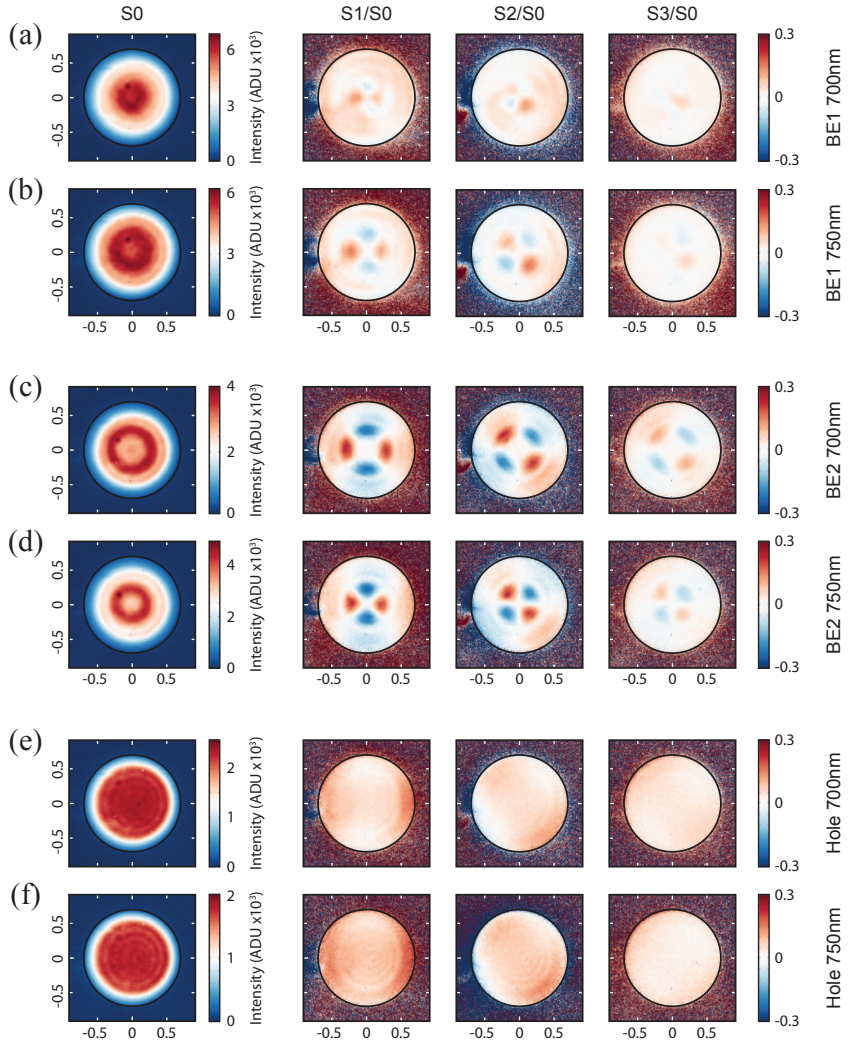

Figure 5.3: K-space distribution of retrieved Stokes parameters, S_0 and normalized S_1, S_2 and S_3, for emission patterns measured on BE1 (a-b), BE2 (c-d), and single hole apertures (e-f) at two emission wavelengths of 700 nm (a,c,e) and 750 nm (b,d,f).

is qualitatively commensurate with the fact that the ring of the emission at $\mathbf{k}_{||} = 0.2$ is expected to be due to fluorescence that was first captured as SPPs propagating in the gold, and subsequently radiated out at the grooves. Out-coupled SPPs are expected to have a p-polarized (polarization along $\mathbf{k}_{||}$) character. Commensurate with the circular symmetry of the BE and the cylindrically symmetric distribution of

emitters, this non-symmetric distribution simply rotates with the linear polarizer. When viewed through circular polarizers, the emission pattern is more strongly cylindrically symmetric although a small asymmetry remains that we discuss below. We note that these statements are not solely based on relative intensity distributions within measured images, but also on the absolute count rates shown. Since Stokes polarimetry hinges on subtracting measurements at different settings, direct comparability of polarization settings is important.

From the six k-space distribution measurements, we can now retrieve the corresponding Stokes parameters according to equation 5.8. Figure 5.3 shows the retrieved Stokes parameters for the BE1 (a-b) and BE2 (c-d) structures at 700 nm and 750 nm emission wavelengths. As reference, we also measured the emission pattern of a single hole aperture and retrieved the stokes parameters as presented in figure 5.3 (e-f). In this figure, the first column corresponds to the Stokes parameter S_0 which is, in principle, the summation of orthogonal polarization measurements, and therefore, represents the k-space-resolved total emission intensity. The next columns represent differential Stokes parameters S_1, S_2, and S_3 which are all normalized to the total intensity S_0. For both BE structures at both wavelengths, S_0 shows a circularly symmetric radiation pattern with a minimum at $\mathbf{k}_{||} = 0$. The circular symmetry of S_0 arises due to the cylindrical symmetry in the BE structure *and* absence of any symmetry breaking in the pump laser spatial energy density profile in the hole, assured through the circular input polarization.

The single hole aperture shows a homogenous emission pattern which does not change by varying the wavelength, as also reported in unpolarized Fourier microscopy by [16, 27]. Furthermore, the pattern shows little structure in the differential parameters $S_1/S_0, S_2/S_0$ and S_3/S_0. In other words, the fluorophores in the single hole essentially represent an isotropic and unpolarized source. A weak residual polarization at oblique angles may be imparted on the signal through the high-angle differences in Fresnel coefficients of interfaces, which enter when calculating the radiation pattern of emitters near interfaces. Compared to the single hole, BE structures show very directional emission patterns, in accordance with previous literature [16, 17]. This high directionality in emission, as well as in scattering studies, has been assigned to constructive or destructive far-field interferences between the emitted light directly from the aperture and the scattered light at the antenna edges that can be understood in a simple grating picture, or in real space terms, as coherent addition of radiation by concentric infinitely thin rings [16, 31]. If one considers the physics of a simple 1D grating of grooves on gold, one realizes that the grating pitch is comparable to the surface plasmon wavelength. Correspondingly, 2nd order Bragg scattering folds the SPP dispersion relation back onto the $\mathbf{k}_{||} = 0$ point. At perfect matching of the Bragg condition, the output beam would be exactly along the sample normal as observed by Aouani et al. [16]. Instead, we find rings of emission due to imperfect matching. We note that the two BE structures respond differently to changes in the wavelength. While for BE1, the main emission lobe diverges from the normal direction ($\mathbf{k}_{||} = 0$) at longer wavelength, for BE2 the emission lobe converges on the normal direction when increasing the wavelength. This can be explained by noting that neither of the two

bull's eyes is exactly matched to the Bragg condition, but rather that one operates above, and the other below it. This is manifested in figure 5.4 which shows the calculated dispersion relation of SPPs along the gold-water interface. In order to compare the Bragg condition of the bull's eye structures in a single diagram, we have separated the dispersion diagram of figure 5.4 in two parts. The left (negative) and the right (positive) parts of the diagram correspond to the first Brillouin zone of the inverse lattice of pitch 440 nm (BE1) and 600 nm (BE2), respectively. The emission wavelengths of 700 nm and 750 nm are also indicated,which correspond to $k_0 \approx 9.0 \cdot 10^{-3}\,\mathrm{nm}^{-1}$ and $k_0 \approx 8.4 \cdot 10^{-3}\,\mathrm{nm}^{-1}$, respectively. From figure 5.4, we observe that the 2nd order Bragg condition ($\mathbf{k}_{||} = 0$) happens above and below the the emission wavelengths for BE1 and BE2 structures. As the wavelength increases (wavenumber decreases), the BE1 structure (left part) diverges from the Bragg condition, while the BE2 structure (right part) converges to the Bragg condition. This is commensurate with diverging (converging) emission lobe of the BE1 (BE2) structure when increasing the wavelength, as shown in figure 5.3 (a-d).

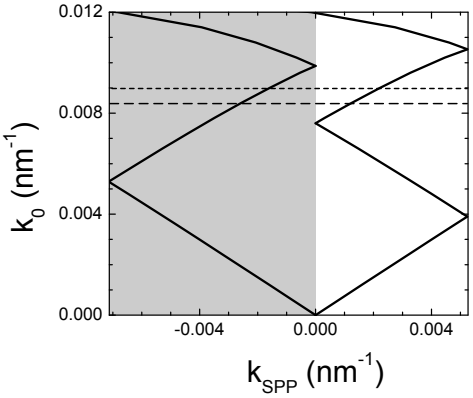

Figure 5.4: Calculated dispersion relation of SPPs at gold-water interface. The left and right parts of the diagram show the folded dispersion curve over the edge of the first Brillouin zone corresponding to $p = 440$ nm and $p = 600$ nm, respectively. The indicated wavenumbers at $k_0 \approx 8.4 \cdot 10^{-3}\,\mathrm{nm}^{-1}$ and $k_0 \approx 9.0 \cdot 10^{-3}\,\mathrm{nm}^{-1}$ correspond to wavelengths 750 nm and 700 nm, respectively.

5.4.2 K-space resolved Stokes parameters S_1, S_2 and S_3

We continue with the other three Stokes parameters S_1, S_2, and S_3, in figure 5.3. According to their definition (eq. 5.8) these Stokes parameters contain complete information about the polarization state of the emitted light. Looking at their corresponding columns in figure 5.3, we immediately find strong structure in the maps for all the BE structures, with comparable features for all wavelength/bull's eye combinations.

Specifically, we note that for emissions outside the main lobe of the antenna, Stokes parameters S_1, S_2, and S_3 show values close to zero, while they all show pronounced polarization features at the position of the main emission lobe of the antennas. The Stokes parameters S_1 and S_2 relating to linear polarization, both contain patterns that follow the orientation of the defining orthogonal polarizations of the Stokes parameters: S_1 exhibits horizontal-vertical symmetry, and S_2 exhibits $\pm 45^\circ$ symmetry in a clover-leaf pattern with leaves of opposing sign. The linear polarization contrast at off-angles evidences the p-polarized nature of the redirected fluorescence light from the antenna. In contrast, for the single hole aperture, Stokes maps do not display strong features.

The circular Stokes parameter S_3 shows a small handed component to the emitted light and features a horizontal-vertical symmetry. We note that within our experimental geometry we would have expected no circular polarization component. Since both the sample, the illumination wavevector and the illuminating spatial energy density set up in the hole are cylindrically symmetric, the only two possible explanations are (1) retention in fluorescence of the incident circular polarization, or (2) imperfect set up alignment. We attribute the observed handedness to a alignment/waveplate inaccuracy of the polarimeter or other misalignments in the setup. However, we note that the cylindrical symmetry of the bull's eye structure and spatial mode of the driving is not enough to exclude a handed response. In particular if one would perform a scattering experiment with linear polarization normally incident on the hole, at off-angles still one can observe handed light with a handedness allowed due to symmetry-breaking by viewing direction.

5.4.3 Effect of the pump polarization

As discussed earlier in section 5.4.1, in order to avoid any symmetry-breaking by the pump-field polarization, in our measurements we set the input laser polarization to circular. To illustrate the effect of the pump polarization on the emission symmetry of the antenna, in figure 5.5 (c) we show polarimetry measurement results of the BE2 structure at 750 nm, for which the input polarization is set linearly along the x-axis. We can directly compare the effect of the pump polarization, by comparing figure 5.5 (c) with 5.5 (b) in which the input polarization is circular. While the k-space resolved degree of (linear) polarization is symmetric in figure 5.5 (b), we find a strong asymmetry in the degree of (linear) polarization in figure 5.5 (c). This asymmetry is aligned principally with the orientation of the pump polarization. Particularly, the degree of (linear) polarization is maximum along the x-axis, while it has a minimum close to zero along the perpendicular y-axis which is indicative of the fact that at those angles the light is completely unpolarized.

We explain this symmetry-breaking by the following reasoning. First, we note that due to the small size and plasmonic nature of the antenna hole itself, the excitation field for the molecules should not be identified simply with the incident focus, but rather is dictated by the near field response of the hole at the pump wavelength. The pump field distribution in the hole is expected to be strongly spatially dependent, with a spatial dependence on the polarization of the incident light. As analogy to understand this

statement, we refer to the canonical physics of the inverse of a hole in a metal film, i.e., a metal particle, for which it is evident that field is highest at the metal interface, in two dipolar lobes along the incident polarization. Thus, when the pump field has a linear polarization, the resulting profile contains hot-spots mainly along the polarization axis of the pump light, while for circular input polarization, the resulting profile is rotationally symmetric. This spatial pump field inhomogeneity translates into an inhomogeneity in the density of the excited molecules. Since the coupling of emission of the molecules to SPPs depends on position in the hole with respect to the edge, a density asymmetry of excited fluorophores can translate into an effective radiation pattern asymmetry. This means that the polarization of the out-coupled light from the molecules to the antenna structure can be predetermined by the pump-field polarization *without* requiring that the molecules retain a direct memory of their excitation field polarization.

We note that in principle, fluorophores could also retain directly a memory of the direction of the linear pump light polarization in their emission [32]. Indeed, in the solid state where molecules are fixed in a matrix, one would expect that the emission efficiency for a molecule depends on the projection of its absorption dipole moment on the pump field, while it emits according to its emission dipole moment. Since these dipole moments are simply fixed to the molecular frame, ensemble fluorescence measurements will show a degree of polarization for polarized input light. This asymmetry is evident most when there is an orientational similarity between the excitation and emission dipole transitions, and when the molecules are rotationally immobile. In solution, molecules rotate on a time scales slightly faster than their lifetime, meaning that rotational diffusion can be measured in polarized spontaneous emission decay traces [32]. In our measurements, molecules are free to rotate in solution. We can not quite exclude this rotation memory effect in our measurements, since the fluorescent molecules that we used here have relatively short decay times of about 1 ns, which may be further accelerated by plasmonic Purcell effects. The rotational diffusion times of fluorescent molecules in water are typically in the order of a few 100 ps. This means that a small part of the molecules may emit light preferentially with the same polarization as the excitation light which could contribute slightly to the observed polarization asymmetry.

5.4.4 Stokes parameters converted to other useful figures of merit

As explained in section 5.2, an important fundamental advantage of Stokes parameters over Jones vectors is that Stokes vectors also capture the degree of polarized light. In a scattering experiment in which one sends coherent, fully polarized light on to a structure, scattered light will retain a degree of polarization that is equal to one. In our fluorescence experiment, however, emission is due to an ensemble of mutually incoherently fluorescing molecules that are only in part coupled to the structure, while others will contribute to an incoherent and unpolarized background. In order to further understand the polarization response of our antennas, we define three figures of merit based on the Stokes parameters: total degree of polarization DP, degree of linear

polarization DLP, and degree of circular polarization DCP, which are defined as:

$$\begin{aligned} DP &= \frac{\sqrt{S1^2 + S2^2 + S3^2}}{S0} \\ DLP &= \frac{\sqrt{S1^2 + S2^2}}{S0} \\ DCP &= \frac{S3}{S0} \end{aligned} \tag{5.10}$$

In figure 5.5, we plotted the three k-space-resolved degree of polarization quantities for BE1 (a) and BE2 (b) structures at 750 nm. Since the effect of varying the emission wavelength is reflected on the opening angle of the antenna emission lobes, for simplicity, here we only consider emission wavelength of 750 nm. For both structures

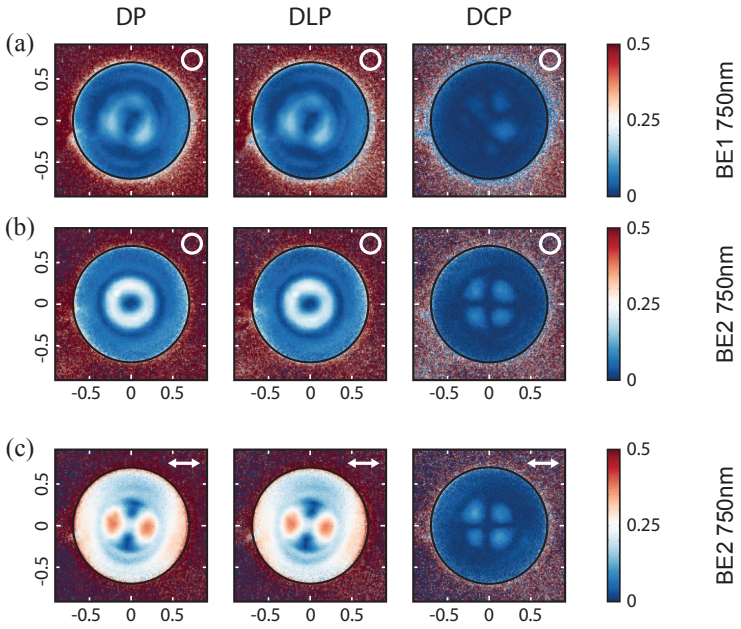

Figure 5.5: Total degree of polarization (DP), degree of linear polarization (DLP), and degree of circular polarization (DCP) for (a) BE1 and (b,c) BE2 structures at 750 nm. The input pump polarization in (a,b) is circular, and in (c) is linear along x-axis.

in figure 5.5, the maximum total degree of polarization (first column) is almost 0.25. This degree of polarization is on one hand limited by the fraction of molecules actually coupled to the plasmon resonance, and on the other hand by the degree to which the plasmon structure itself has a polarization preference. Comparing the total degree of polarization with the degree of linear polarization in figure 5.5, we find that the DP

and DLP values are quite comparable. This means that the bull's eye antenna mainly emits light with linear polarization. In fact, the groove structure, but not the hole itself, preferentially emits p-polarized light, as discussed earlier. We find similar conclusions for the emission wavelength of 700 nm and for BE1 structure, which are not presented here. Overall, our measurement suggests that Stokes polarimetry is a new route to determine the *fraction* of molecules in an ensemble close to a plasmonic structure that is actually coupled to the plasmonic resonance.

5.4.5 s-p polarization and ellipticity analysis for the bull's eye structure

The hypothesis that the polarized part of the emission must have been established through the grooves, and must hence be p-polarized, can in fact be directly tested on our data sets. For the polarized part of the light, the full field vector, up to an overall phase, can be reconstructed as

$$\begin{aligned} |E_x| &= \sqrt{I_{0,0} - S_0(1-DP)/2} \\ |E_y| &= \sqrt{I_{90,90} - S_0(1-DP)/2} \\ \delta &= \phi_y - \phi_x = \arg(S_2 + iS_3). \end{aligned} \tag{5.11}$$

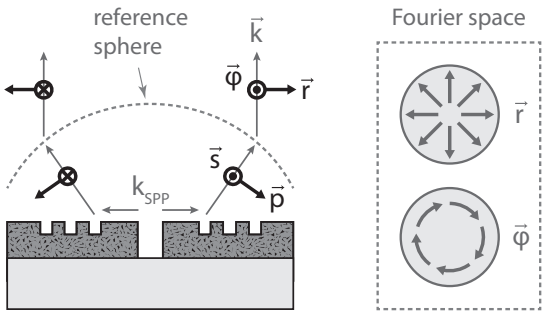

Figure 5.6: Schematic diagram of the p- and s- polarization of the scattered light in object space (spherical wave), which transforms into radial and azimuthal polarization components in the cylindrical beam that is found after the objective, that is, in our Fourier image. The 'reference sphere' represents the refraction by the objective lens as defined in the lens construction appropriate for aplanatic lenses [33].

After this reconstruction, the field can be projected onto any desired polarization analysis basis. For instance, for any point (ρ, φ) in the back-aperture image, the radial component (**E** projected on $(\cos\varphi, \sin\varphi)$) respectively azimuthal component (**E** projected on $(-\sin\varphi, \cos\varphi)$) can be reconstructed. Given that our objective is designed according to the Abbe sine condition for aplanatic lenses, these polarizations directly correspond to separation into the p- and s-polarized field, as referenced back to the

spherical wave emanating from the bull's eye in the object plane. This is schematically depicted in figure 5.6, which shows that any p-polarized, respectively s-polarized scattered light, as referenced to the spherical coordinates that describe the far field concentric with the scatterer, transform into radially, respectively azimuthally polarized light in the back focal plane, i.e., after refraction in the reference sphere that represents the objective [33].

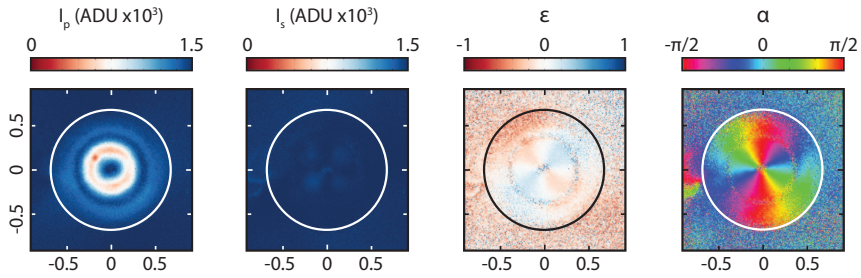

Figure 5.7: k-space distribution of the retrieved p- and s- polarization components of the intensity (I_p and I_s) and the shape parameters of the polarization ellipse (ϵ and α) of the emitted light from the bull's eye BE2 structure at the emission wavelength of 750 nm.

According to equations 5.11 and 5.9, we can retrieve the p and s intensity components, I_p and I_s, as well as the shape parameters of the polarization ellipse ϵ and α from the measured Stokes parameters. We plotted the k-space resolved I_p, I_s, ϵ and α of the emitted light from the bull's eye BE2 structure at 750 nm in figure 5.7. In agreement with our expectation, we observe that the major part of the emitted light from the bull's eye structure is p-polarized, with intensities peaking at 1500 CCD counts, while I_s is very small, with intensities below 50 counts. This is direct additional support for the involvement of surface plasmon polaritons in bull's eye emission control [11, 16, 31].

Rather than plotting s- and p-components, some workers are more accustomed to ellipticity, and polarization ellipse orientation. Throughout the ellipticity ϵ is close to zero within the emission lobes of the antenna. This means that the polarized component of the emitted light from the bull's eye antenna is mainly linearly polarized. This is expected since, assuming that the emitters are an isotropic random ensemble of sources that are spatially distributed in the hole in a cylindrically symmetric manner, no preferential handedness can be defined by symmetry. We assign the small visible ellipticity to the measurements inaccuracies as explained earlier for the k-space distribution of S3 parameter (section 5.4.1). In this basis for plotting, the p-polarized emission is visible through the fact that the orientation of the polarization ellipse α rotates monotonically from E_x to E_y which is commensurate with the symmetry of the bull's eye. The noise in ϵ and α appears where the intensity of the light is at its minimum.

5.4.6 K-space polarimetry measurements for spiral structure

We have also performed k-space polarimetry on left-handed and right-handed spiral structures. Such spirals were pursued by Gorodetski et al. [34] who claimed that such spirals add and subtract orbital angular momentum to externally incident beams. Figure 5.8 shows, as an example, the k-space resolved Stokes parameters measured on left-handed spiral LS2 (a) and right-handed spiral RS2 (b) structures at the emission wavelength of 750 nm. These two structures belong to the same family as the BE2 structure (figure 5.3 (d)), in particular sharing the same geometrical parameters $a = p = 600$ nm.

Comparing the spiral structures in figures 5.8 and the bull's eye structure in figure 5.3 (d), we find that the total emission intensity (S_0) of both spiral structures display an emission ring in k-space with the maximum at $\mathbf{k}_{||} = 0.2$ which is the same as for the emission of the BE2 structure. However, the normalized linear Stokes parameters S_1 and S_2 of the spirals, no longer show horizontal-vertical symmetry as in BE2 structure. We assign this to the symmetry-breaking nature of the spiral structures. The Stokes parameter S_3 of the spiral structures which contain information about the handedness of the emitted light, exhibit handed features which are different from the BE2 structure. Specifically, we note that by an up-down mirror transformation followed by a sign swap, one can reasonably map the S_3 parameter of the left-handed spiral onto the right-handed spiral, and vice versa. This is commensurate with the fact that LS2 and RS2 structures are up-down mirror symmetric partners of each other (see figure 5.1 (d) and (e)) and the sign swap switches the left- and right- handedness.

Similar to the s- and p- polarization analysis for the bull's eye structure in section 5.4.5, in figure 5.9 we present the retrieved k-space resolved radial and azimuthal intensities I_p, I_s along with the shape parameters of the polarization ellipse, ϵ and α for the emitted light from (a) LS2 and (b) RS2 structures at the emission wavelength of 750 nm. Similar to the bull's eye, here we observe that the major part of the emitted light from the spiral structures is also p-polarized, as in the case of the concentric bull's eye from which the spiral derives. However, for the spirals, the ratio of I_p to I_s is maximally about 3 to 1, rather than in excess of 10 to 1 which indicates that the spirals scatter significantly more light in s-polarization than the bull's eye structure. This is a direct consequence of the breaking of the cylindrical symmetry around the central aperture. The k-resolved ellipticity ϵ in spirals, indicate mainly linearly polarized light, although now the orientation of the polarization ellipse α exhibits non-monotonous angle changes for the lights emitted at different $\mathbf{k}_{||}$ directions. While in this initial study we do not have a full picture for the physics of spirals, it is clear that k-space polarimetry applied to both fluorescence as in this work, and to transmitted light, should greatly aid to unravel the current discussion on whether spirals mainly result in orbital angular momentum effects (phase gradients over the beam, without polarization effects) or chirality (handedness in polarization) [34].

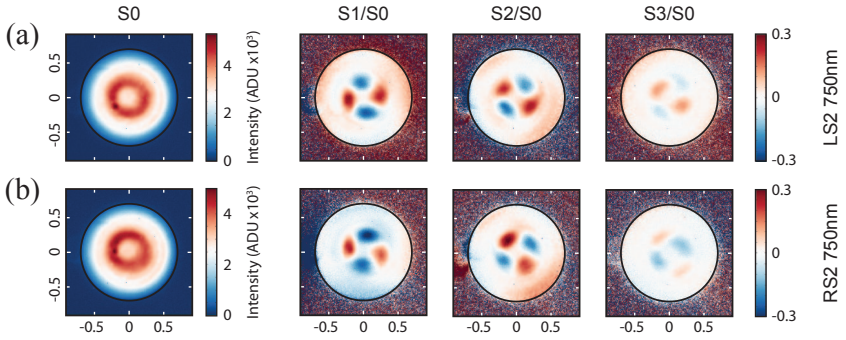

Figure 5.8: K-space distribution of retrieved Stokes parameters, S_0 and normalized S_1, S_2 and S_3, for emission patterns measured on (a) left-handed spiral LS2, and (b) right-handed spiral RS2 structures at the emission wavelength of 750 nm.

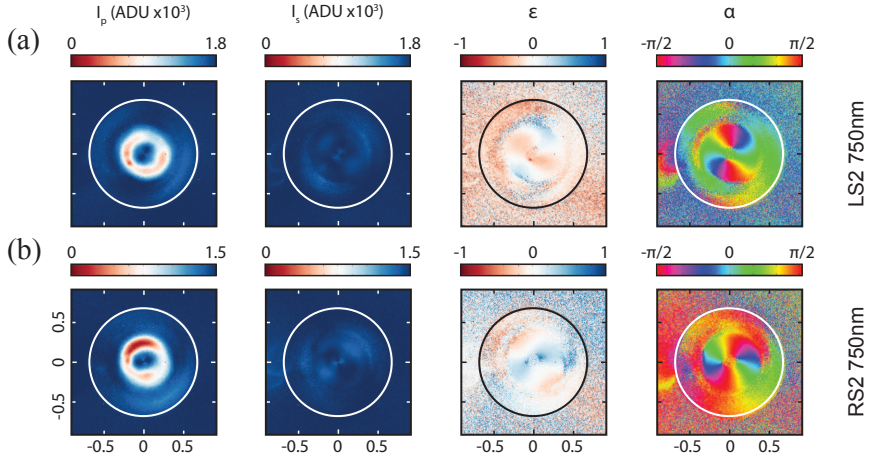

Figure 5.9: k-space distribution of the retrieved p- and s- polarization components of the intensity (I_p and I_s) and the shape parameters of the polarization ellipse (ϵ and α) of the emitted light from (a) left-handed spiral LS2, and (b) right-handed spiral RS2, structures at the emission wavelength of 750 nm.

5.5 Numerical and analytical calculations

In order to better understand the response behavior of our antennas, we finally report on numerical calculations.

5.5.1 COMSOL simulation on bull's eye structures

For our numerical calculations, we used the commercially available software COMSOL (version 4.3b). We modeled the bull's eye structure according to the geometrical parameters given in section 5.4, using optical constants of Etchegoin [35], and using a scattering boundary condition at the edges of the simulation domain. As for the emitter, we modeled an in-plane dipole source as a small (nm-sized) current carrying wire located in the middle of the hole. We note that the very large size of the entire structure, yet narrow features of the grooves, make this simulation computationally highly demanding, for which reason we used symmetry reduction of the computational domain, to be left with about $2 \cdot 10^6$ elements, or $> 10^7$ degrees of freedom. We then recorded the tangential E and H field components on a spherical cap (radius exceeding the spiral size by about a micron) located in the water above the structure and concentric with the hole as input for a near-to-far-field transformation to obtain predicted far fields at the back aperture of a light collecting element (objective) of NA=0.7. We note that this procedure is not rigorous: the Stratton-Chu near-to-far-field transform theorem that is used rigorously only holds for closed observation surfaces in homogeneous space [36]. When viewed as a truncated approximation to an angular spectrum integration to retrieve far field [33], it is evident that the truncation causes unphysical fringes in the final result, corresponding to diffraction by the artificial truncation bound of the Fourier integral. Unfortunately, there is no better solution available to our knowledge. Langguth et al. [27] benchmarked this procedure to have approximately 20% accuracy for emitting dipoles in a similar gold/water geometry. Given the calculated far field, we used the same set of formulas as in equations 5.5 and 5.8 to calculate the Stokes parameters. In order to simulate incoherent superposition of all in-plane dipole moments, before calculating the Stokes parameters, for each polarized detector signal we sum the corresponding intensity components (i.e., incoherent addition) of a set of dipole moments whose orientations are isotropic, as we believe is appropriate for experiments with circularly polarized pump light.

Figure 5.10 shows the results of the simulated Stokes parameters for the BE2 structure at two emission wavelengths of 700 nm (a) and 750 nm (b). Comparing the simulation results with experimental measurements of figure 5.3, we find similarities in gross features. These are (1) that the ring-shaped emission pattern in S_0 widens on red-shifting, (2) that the S1 and S2 pattern are 45 degree rotated versions of each other, with four nodal lines that separate lobes of alternating sign, and (3) that the degree of polarization is only partial. Also, in our simulation we did not find any circular component for the Stokes parameter S_3 beyond the computational errors, and therefore, we did not present it in figure 5.10. However, more detailed analysis shows significant differences, in particular including the multi-ring structure in S_0, an associated nodal circle in S1 and S2, and the occurrence of much stronger polarization at larger angle than in the data. We note that arriving at a truly comparable model is a formidable challenge: first, in any volume-discretization method, the near-to-far field transform approach fails for lack of sufficient lateral dimension of the integration surface. This

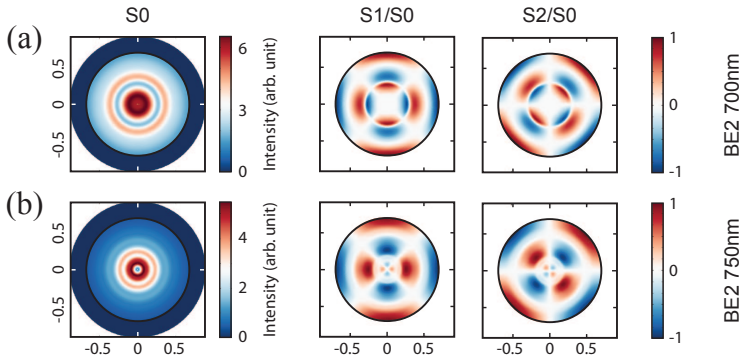

Figure 5.10: Simulated Stokes parameters of the BE2 structure at emission wavelengths of (a) 700 nm and (b) 750 nm. The values of the Stokes parameter S_3 is negligible and therefore is not presented here.

leads to unphysical ringing in the calculated result. Second, a frequency averaging, and a fluorophore position averaging over the entire hole is required. As symmetry-reduction arguments to reduce computation time fail for general dipole positions, this leads to unfeasible computation times.

5.6 Conclusion

To conclude we have presented a novel experimental technique for the study of plasmonic nanoantennas, namely Stokes polarimetry of wavevector images. While our work is simply a first exploratory study, taking bull's eye antennas as an example, it is evident that our technique has large potential. Mapping Stokes parameters allows new insight in the strength of antenna coupling to molecules by rigorously separating out the polarized and unpolarized part of emission. Moreover, the resulting polarized signal can be cast in any polarization analysis basis *after* performing six measurements with two simple elements. We have demonstrated this capability by showing that the fully polarized, i.e., plasmon-mediated, emission is p-polarized to a very large degree at all emission angles in the microscope back-aperture. Further we have shown that the polarization ellipse orientation can be a sensitive probe of the effect of structural handedness on emission. Since our powerful technique is very easily implemented, we envision an important role in studies of chiral plasmon antennas, metasurfaces, and nanostructures.

References

[1] H. Gersen, M. F. García-Parajó, L. Novotny, J. A. Veerman, L. Kuipers, and N. F. van Hulst, *Influencing the angular emission of a single molecule*, Phys. Rev. Lett. **85**, 5312 (2000).

[2] H. F. Hofmann, T. Kosako, and Y. Kadoya, *Design parameters for a nano-optical yagi-uda antenna*, New J. Phys. **9**, 217 (2007).

[3] J. Li, A. Salandrino, and N. Engheta, *Shaping light beams in the nanometer scale: A yagi-uda nanoantenna in the optical domain*, Phys. Rev. B **76**, 245403 (2007).

[4] A. F. Koenderink, *Plasmon nanoparticle array waveguides for single photon and single plasmon sources*, Nano Lett. **9**, 4228 (2009).

[5] A. G. Curto, G. Volpe, T. H. Taminiau, M. P. Kreuzer, R. Quidant, and N. F. van Hulst, *Unidirectional emission of a quantum dot coupled to a nanoantenna*, Science **329**, 930 (2010).

[6] T. Coenen, E. J. R. Vesseur, A. Polman, and A. F. Koenderink, *Directional emission from plasmonic yagi-uda antennas probed by angle-resolved cathodoluminescence spectroscopy*, Nano Lett. **11**, 3779 (2011).

[7] G. Vecchi, V. Giannini, and J. Gómez Rivas, *Shaping the fluorescent emission by lattice resonances in plasmonic crystals of nanoantennas*, Phys. Rev. Lett. **102**, 146807 (2009).

[8] S. R. K. Rodriguez, S. Murai, M. A. Verschuuren, and J. Gòmez Rivas, *Light-emitting waveguide-plasmon polaritons*, Phys. Rev. Lett. **109**, 166803 (2012).

[9] G. Lozano, D. J. Louwers, S. R. Rodriguez, S. Murai, O. T. Jansen, M. A. Verschuuren, and J. Gomez Rivas, *Plasmonics for solid-state lighting: enhanced excitation and directional emission of highly efficient light sources*, Light Sci. Appl. **2**, e66 (2013).

[10] C. Belacel, B. Habert, F. Bigourdan, F. Marquier, J.-P. Hugonin, S. Michaelis de Vasconcellos, X. Lafosse, L. Coolen, C. Schwob, C. Javaux, B. Dubertret, J.-J. Greffet, P. Senellart, and A. Maitre, *Controlling spontaneous emission with plasmonic optical patch antennas*, Nano Lett. **13**, 1516 (2013).

[11] H. J. Lezec, A. Degiron, E. Devaux, R. A. Linke, L. Martin-Moreno, F. J. Garcia-Vidal, and T. W. Ebbesen, *Beaming light from a subwavelength aperture*, Science **297**, 5582 (2002).

[12] J. Wenger, P.-F. Lenne, E. Popov, H. Rigneault, J. Dintinger, and T. Ebbesen, *Single molecule fluorescence in rectangular nano-apertures*, Opt. Express **13**, 7035 (2005).

[13] J. Wenger, B. Cluzel, J. Dintinger, N. Bonod, A.-L. Fehrembach, E. Popov, P.-F. Lenne, T. Ebbesen, and H. Rigneault, *Radiative and nonradiative photokinetics alteration inside a single metallic nanometric aperture*, J. Phys. Chem. C **111**, 11469 (2007).

[14] J. Wenger, D. Gérard, J. Dintinger, O. Mahboub, N. Bonod, E. Popov, T. W. Ebbesen, and H. Rigneault, *Emission and excitation contributions to enhanced single molecule fluorescence by gold nanometric apertures*, Opt. Express **16**, 3008 (2008).

[15] J. Wenger and H. Rigneault, *Photonic methods to enhance fluorescence correlation spectroscopy and single molecule fluorescence detection*, Int. J. Mol. Sci. **11**, 206 (2010).
[16] H. Aouani, O. Mahboub, N. Bonod, E. Devaux, E. Popov, H. Rigneault, T. W. Ebbesen, and J. Wenger, *Bright unidirectional fluorescence emission of molecules in a nanoaperture with plasmonic corrugations*, Nano Lett. **11**, 637 (2011).
[17] H. Aouani, O. Mahboub, E. Devaux, H. Rigneault, T. W. Ebbesen, and J. Wenger, *Plasmonic antennas for directional sorting of fluorescence emission*, Nano Lett. **11**, 2400 (2011).
[18] M. Schäferling, D. Dregely, M. Hentschel, and H. Giessen, *Tailoring enhanced optical chirality: Design principles for chiral plasmonic nanostructures*, Phys. Rev. X **2**, 031010 (2012).
[19] F. Bernal Arango and A. F. Koenderink, *Polarizability tensor retrieval for magnetic and plasmonic antenna design*, New. J. Phys. **15**, 073023 (2013).
[20] L. Allen, M. W. Beijersbergen, R. J. C. Spreeuw, and J. P. Woerdman, *Orbital angular momentum of light and the transformation of laguerre-gaussian laser modes*, Phys. Rev. A **45**, 8185 (1992).
[21] F. J. Rodríguez-Fortuño, G. Marino, P. Ginzburg, D. O'Connor, A. Martínez, G. A. Wurtz, and A. V. Zayats, *Near-field interference for the unidirectional excitation of electromagnetic guided modes*, Science **340**, 328 (2013).
[22] X. Yin, Z. Ye, J. Rho, Y. Wang, and X. Zhang, *Photonic spin hall effect at metasurfaces*, Science **339**, 1405 (2013).
[23] R. Mitsch, C. Sayrin, B. Albrecht, P. Schneeweiss, and A. Rauschenbeutel, *Directional nanophotonic atom–waveguide interface based on spin-orbit coupling of light*, Preprint arXiv:1406.0896 (2014).
[24] I. Söllner, S. Mahmoodian, A. Javadi, and P. Lodahl, *A chiral spin-photon interface for scalable on-chip quantum information processing*, Preprint arxiv:1406.4295 (2014).
[25] B. Le Feber, N. Rotenberg, and L. Kuipers, *A scalable interface between solid-state and flying qubits: observations of near-unity dipole helicity to photon pathway coupling*, Preprint arxiv: 1407:7741 (2014).
[26] M. A. Lieb, J. M. Zavislan, and L. Novotny, *Single-molecule orientations determined by direct emission pattern imaging*, J. Opt. Soc. Am. B **21**, 1210 (2004).
[27] L. Langguth, D. Punj, J. Wenger, and A. F. Koenderink, *Plasmonic band structure controls single molecule fluorescence*, ACS Nano **7**, 8840 (2013).
[28] I. Sersic, C. Tuambilangana, and A. F. Koenderink, *Fourier microscopy of single plasmonic scatterers*, New J. Phys. **13**, 083019 (2011).
[29] M. Born and E. Wolf, *Principles of Optics*, Cambridge University Press, 7 edition, 1999.
[30] J. D. Jackson, *Classical Electrodynamics*, Wiley, New York, 1999.
[31] O. Mahboub, S. C. Palacios, C. Genet, F. J. Garcia-Vidal, S. G. Rodrigo, L. Martin-Moreno, and T. W. Ebbesen, *Optimization of bull's eye structures for transmission enhancement*, Opt. Express **18**, 11292 (2010).
[32] J. R. Lakowicz, *Principles of fluorescence spectroscopy*, Springer, New York, 2006.
[33] L. Novotny and B. Hecht, *Principles of Nano-optics*, Cambridge University Press, Cambridge, 2006.
[34] Y. Gorodetski, A. Drezet, C. Genet, and T. W. Ebbesen, *Generating far-field orbital angular momenta from near-field optical chirality*, Phys. Rev. Lett. **110**, 203906 (2013).
[35] P. G. Etchegoin, E. C. Le Ru, and M. Meyer, *An analytic model for the optical properties of gold*, J. Chem. Phys. **125**, 164705 (2006).
[36] A. Taflove and S. C. Hagness, *Computational electrodynamics: the finite-difference time-domain method*, Artech House, Norwood, 3rd edition, 2005.

Summary

A main promise of the field of physics called "nanophotonics" that deals with nanotechnology to control light, is to provide control over the emission of light sources. Recent developments in the field of solid state lighting that resulted in bright and efficient LEDs, as an example, rely directly upon our understanding of how to control the emission of light. On the other hand, scientific advances in the fields of super-resolution microscopy, optical and quantum information processing, cryptography and secure communication, significantly rely on advances in controlling the emission of single photons, the detection of single photons, and increasing the light-matter interaction strength between emitters and single photons. In all these applications, the main question is how to control the emission of light in terms of the rate at which the source emits, the direction into which it radiates, and the polarization in which the source emits a photon. In this thesis we address how to choose an efficient single photon emitter, how to characterize a nanophotonic structure which controls the rate and direction of the emitted light, and how to fully characterize the polarization of the emitted light.

In chapter 2, we study the statistical properties of single nanodiamond NV centers. Specifically, we quantify the brightness and the decay rate of many individual NV centers in two sets of diamond nanocrystals with mean diameters of 25 nm and 100 nm. Our quantifications show that for both sets of nanodiamond diameters, the brightness and the decay rate of the NV centers are widely distributed, a finding that is in agreement with previous reports. The common opinion in the field so far has been based on the speculation that this distribution is entirely due to size dependent variations of the 'local density of optical states' in different diamond nanocrystal matrices, while assuming a near unity quantum efficiency for the NV centers. In contrast, based on the absence of strong correlation between the measured decay rate and brightness of the NV centers, we suggest that the wide distributions in decay rate and brightness are likely due to a distribution in the quantum efficiency of the NV centers. To support this, we calculate the local density of optical state variations according to the size distribution of our nanodiamonds and we find that it is not sufficient to describe our measured decay rate distributions and we argue that there should hence be a wide distribution in both

radiative and nonradiative decay rates and, therefore, also in the quantum efficiency of the nanodiamond NV centers.

Our findings in chapter 2, showing that the quantum efficiency of NV centers in nanodiamond does not correlate with their readily measurable quantities like spectrum and brightness is crucial to nanophotonics application where NV centers are used as efficient fluorescent emitters or probes of the photonic environment. This implies that one can not choose the best NV center only based on its brightness, spectrum or decay rate. Instead one needs to utilize experimental protocols to directly quantify the quantum efficiency of each individual nanodiamond NV center before applying it to the target nanophotonic assembly as an emitter or probe. We introduce such protocols in the next chapter.

In chapter 3, for the first time, we quantify the quantum efficiency of individual nanodiamond NV centers reversibly and nondestructively. To this end, we use two techniques to apply known variations in the local density of optical states to the photonic environment of the NV centers. In the first method, we vary the LDOS using liquids with different refractive indices which we apply to the 25 nm nanodiamonds. We find that the small nanodiamonds are insensitive to the moderate variations of the LDOS. In connection with the measured decay rate distribution of the NV centers in chapter 2, we conclude that the 25 nm nanodiamond NV centers have a distributed low quantum efficiency between 0% and 20%. In the other technique, we use a metal coated micro-mirror bead attached to the end of a near-field scanning tip to induce known LDOS variations. This is realized by nanomechanically changing the distance between the mirror and individual NV centers. Using this technique with 100 nm nanodiamonds, for the first time, we report the results of quantitative measurements of the quantum efficiency of single NV centers. We show that the quantum efficiency of nanodiamond NV centers can be far from unity and is indeed widely distributed between 10% and 90%. This is in agreement with our assumption in chapter 2 and in contrast to the common belief that considers a near unity quantum efficiency for all nanodiamond NV centers. This highlights the importance of utilizing a nondestructive and reversible quantum efficiency calibration method, as shown in this chapter, to screen nanodiamond NV centers as efficient emitters or probes.

While chapters 2 and 3 involve how to choose the best emitter, in chapter 4, we discuss how to control and characterize the emission properties of such an emitter when it is coupled to a nanophotonic structure. Specifically we study a new type of nanophotonic antenna known as plasmonic patch antenna which consists of a circular patch of metal that is separated from a metallic ground plate via a dielectric material of several 10 nm thickness. This antenna has already been shown to enhance the spontaneous emission of the emitters that are coupled to it while providing a very directional emission. In this chapter we use a technique called angle-resolved cathodoluminescence imaging spectroscopy (ARCIS) to characterize the spatial modes and emission properties of the plasmonic patch antennas. This technique is based on scanning an electron beam over the antenna structure to excite the plasmonic modes of the antenna. By collecting the induced and scattered light, we obtain high-resolution maps of the spatial and spectral mode structure, as well as the angular emission patterns

of the plasmonic patch antenna. To understand the observed modes, we use a semi-analytical model that is based on LDOS variations in the patch antenna. We find qualitative similarities between the experimental and the calculated maps. However a one-to-one quantitative agreement is not present which we assign to the complex nature of mode excitation by the electron beam. Furthermore, we present the results of the measured angular distribution of the antenna radiation and find that for resonant excitation of the antenna, the emission is highly directional with a doughnut-shaped beam profile. Although this beam profile has been predicted in previous reports, it has not been verified experimentally. Moreover, we observed directional beam steering in the patch antenna which we explained using a simple distributed dipole model, where, the scattering of the light (surface-plasmon-polaritons) at the antenna edges are modeled by a set of radiating dipoles. We find good agreement between the model and the experimental radiation patterns of the antenna at different excitation positions.

Finally, in chapter 5, we present a new microscopy technique to fully map the polarization state of the light scattered or emitted by a single nano-object for all the different directions in its angular radiation pattern. We realize this by using a Fourier microscope that images the back focal plane (k-space) of a high-NA objective, in combination with a Müller polarimeter, which consists of a polarizer and a quarter-wave plate. We apply our technique to the fluorescence of dye molecules residing in the central nanoaperture of so-called plasmonic bull's eye antennas, and also in spiral antennas which consist of concentric or spiral metallic grooves around the nanoaperture. Using our technique, we characterize the emission from the bull's eye and the spiral plasmonic antennas in terms of the total degree of polarization as well as the degree of circular and linear polarization. Moreover, we extract the orientation and eccentricity of the polarization ellipse for the polarized component of the emitted fluorescence light from our antennas. We show that the emission from both antennas display a significant degree of polarization, while the emission from a simple nanoaperture lacks any strong degree of polarization. We assign the observed degree of polarization to the fact that a part of the fluorescence emitted by the molecules is captured by surface plasmon polaritons, that subsequently radiate out in a directional manner. Since surface plasmon polaritons are p-polarized surface waves this indirect, plasmon-mediated, emission becomes polarized even though the ensemble of emitting dipoles itself is entirely random. Furthermore, we investigate the effect of the pump polarization and perform numerical simulations to model the polarization state of the emitted light from our bull's eye antenna.

Samenvatting

Nanofotonica is een discipline in de natuurkunde die zich bezig houdt met de voortplanting, het genereren, versterken, en detecteren van licht. Een belangrijke mogelijkheid die nanofotonica biedt is om het genereren van licht in nanoschaal lichtbronnen te manipuleren. Recente ontwikkelingen in het vakgebied van LED-verlichting met behulp van halfgeleiders, in plaats van lichtgeneratie met gloeilampen of in gassen, worden mogelijk gemaakt door ons begrip van hoe het proces van het uitstralen van licht werkt. Ook zijn wetenschappelijke vooruitgangen op het gebied van super-resolutie microscopie, optische informatieverwerking, en quantum informatica, te danken aan de mate waarin we het genereren van enkele fotonen door enkele atomen, quantum dots of moleculen kunnen beheersen, de mate waarin we enkele fotonen efficiënt kunnen detecteren, en het feit dat in speciale nanostructuren een hele sterke koppeling tussen enkele fotonen en enkele stralers mogelijk is. In al deze toepassingen is de centrale vraag hoe je het uitstralen van licht manipuleert in termen van drie parameters: hoe lang het duurt voor een bron zijn lichtdeeltje uitstraalt, waarheen het lichtdeeltje uitgestraald wordt, en met welke polarisatie. In dit proefschrift staat de vraag centraal hoe men de meest efficiënte bron kan kiezen, en hoe je nanofotonische structuren karakteriseert die ontworpen zijn om controle te geven over hoe lang het duurt voor licht uitgestraald wordt, over de richtingsverdeling, en de polarisatie. In hoofdstuk 2 bestuderen we de eigenschappen van stralende defecten in nanodeeltjes van diamant, namelijk van zogenaamde "nitrogen-vacancy"centers. Dit puntdefect wordt sinds 2000 bestudeerd, onder andere omdat het een enkel quantum systeem is dat als bron van enkele fotonen kan dienen bij kamertemperatuur, en zonder enige degradatie van zijn eigenschappen over de tijd. Wij bestuderen de statistische verdeling van eigenschappen van enkele NV centra in enkele nanodiamant deeltjes. We bestuderen zeer kleine diamantjes (25 nm doorsnee), en wat grotere (100 nm doorsnee). Onze metingen laten zien dat, ondanks het feit dat NV centra nominaal allemaal dezelfde structuur in de kristallijne diamantmatrix hebben, de eigenschappen zoals helderheid van fluorescentie, en de vervalsconstante (hoe lang het gemiddeld duurt voor het centrum straalt) buitengewoon wijd verdeeld zijn. Deze conclusie is ook eerder door andere wetenschappers getrokken, die als speculatieve verklaring aanvoerden dat de NV centers weliswaar elektronisch intrinsiek allemaal bijna hetzelfde zijn, maar dat de helderheid en het verval beïnvloed

worden door het feit dat de optische toestandsdichtheid in de wisselend gevormde, hoge brekingsindex nanodeeltjes zeer sterk wisselt. In tegenstelling daarop constateren wij dat er geen enkel consistent verband is tussen helderheid en vervalssnelheid , en dat er daarom waarschijnlijk een brede verdeling is in quantum efficiëntie. Om dit te testen berekenen we de lokale optische toestandsdichtheidsverdeling voor ons ensemble van nanodeeltjes. We vinden dat deze berekende verdeling bij lange na niet voldoende breed is om de metingen te verklaren, daarmee onze conclusie ondersteunend dat er een brede verdeling is in stralende vervalstijden, nietstralende vervalstijden, en quantum efficiëntie.

Onze bevindingen in hoofdstuk 2 laten zien dat de kwaliteit van NV centra als stralers helemaal niet te meten is door alleen spectra te verzamelen, of helderheid te meten, of vervalstijd. Omdat efficiëntie cruciaal is voor elke toepassing betekent dit dat er wel een protocol nodig is, maar er geen eenvoudig protocol bestaat, waarmee NV centers te selecteren zijn, en dat het daadwerkelijk meten van quantum efficiëntie niet te omzeilen is. Het meten van quantum efficiëntie, zeker van enkele bronnen is zeer lastig. Wij hebben experimentele protocollen om de efficiëntie van enkele fotonbronnen te meten toegepast op NV kleurencentra in hoofdstuk 3. Deze protocollen gebruiken methodes om de fotonische omgeving van de diamantjes reversibel en niet-destructief te wijzigen, zodat het inderdaad mogelijk is diamanten eerst te testen, en vervolgens na selectie in te bedden in een fotonische structuur. De eerste van de twee technieken die we toepassen bestaat er uit dat we toestandsdichtheid veranderen door nabij de nanodiamanten die net onder een oppervlak verscholen liggen de brekingsindex te veranderen met behulp van vloeistoffen. Deze methode hebben we toegepast op 25 nm nanodiamantjes. We vinden dat NV centra in deze kleine diamantjes helemaal niet reageren op de, helaas maar beperkte, toestandsdichtheidsvariaties die we hiermee kunnen genereren. Hieruit trekken we de voorzichtige conclusie dat zulke kleine nanodiamantjes lage quantum efficiënties, tussen 0% en 20% geven. De tweede techniek bestaat er uit dat we met behulp van nabije-veld microscopie technieken een spiegelend, iets bollend, oppervlak nabij enkele nanodiamantjes brengen. Dit stelt ons in staat om redelijk grote toestandsdichtheidsveranderingen waar heel nauwkeurige theorie voor bestaat aan te brengen. Dit doen we door de spiegel heen en weer, en daarmee effectief naderbij en verder af van de stralers te brengen. Met deze techniek kunnen we laten zien dat voor 100 nm nanodiamantjes de quantum efficiëntie van NV centers zeer breed verdeeld is, en alle waarden tussen 10% en 90% kan aannemen. Dit bevestigt de hypothese van hoofdstuk 2, en ontkracht de algemeen gemaakte aanname dat NV kleuren centra ongeveer 100% quantum efficiëntie moeten hebben. Het belang van ons werk is met name dat de enige manier om zeker te zijn dat uit een ensemble van nanodiamantjes een goede gekozen wordt er uit bestaat om (bijvoorbeeld met onze methode) daadwerkelijk per NV centrum quantum efficiëntie te meten.

Terwijl de hoofdstukken 2 en 3 zich bezig hielden met de keuze van de beste lichtbron, behandelen we in hoofdstuk 4 de karakterisatie van een nano-antenne waarmee de richtingsverdeling, en de snelheid van afstraling, van enkele bronnen gemanipuleerd kan worden. Meer specifiek bestuderen we een zogenaamde "plasmonische patch antenna"die bestaat uit een ronde schijf goud van enkele golflengtes diameter die vlak

nabij een uitgestrekt goud oppervlak gelegd wordt, slechts gescheiden door een dunne dielektrische laag van slechts enkele tientallen nanometer. Andere onderzoekers hebben al laten zien dat zulke antennes het verval van stralers kan versnellen, en tegelijk de fluorescentie van stralers bundelt. In eerdere studies was het echter niet mogelijk om volledig af te beelden wat de mode structuur van deze antenne is, waar de straler het beste geplaatst kan worden, noch om als functie van positie en golflengte van de straler te bepalen hoe de richtingskarakteristiek vormgegeve n wordt. Wij gebruiken een door collega's op AMOLF ontwikkelde techniek die "hoek-opgeloste cathodoluminescentie microscopie"heet, waarbij heel lokaal licht gegenereerd wordt door het systeem aan te slaan met een nauwe elektronenbundel in een elektronenmicroscoop. De snelle elektronen verliezen energie als ze nabij de structuur komen die deels omgezet wordt in licht, verdeeld over een heel breed spectrum. Door het zichtbare licht op te vangen met een parabolische spiegel is het mogelijk metingen te doen aan hoeveel licht van welke kleur in welke richting uitgestraald wordt, als functie van het punt van aanslaan van de antenne. De hoge resolutie afbeeldingen laten de spectrale en ruimtelijke mode structuur zien. Om deze modes te begrijpen bespreken we analytische en numerieke berekeningen van de toestandsdichtheid in de antenne. Omdat deze mode structuur zeer complex is, vinden we slechts kwalitatieve overeenstemming met het gemeten signaal. We analyseren ook hoekverdelingen van het uitgestraalde licht. Wanneer we de antenne ruimtelijk, en spectraal, precies aanslaan op resonantie, genereert de antenne nauwe "donut"bundels: ringvormige bundels. Zulke profielen waren al voorspeld door andere onderzoekers, maar metingen aan deze structuur lieten dit tot nu toe nooit zien. Bij niet-resonante condities verdwijnt het gat in de (nog steeds) nauwe bundel. Wanneer de elektronenbundel uit het midden van de antenne geplaatst wordt, verdraait de bundel, zoals eenvoudig uit te leggen is met een model gebaseerd op coherente afstraling van plasmonen in de patch antenne die verstrooien aan de rand.

Tot slot richten we ons in hoofdstuk 5 op een nieuwe micoscopie techniek om de graad en aard van polarisatie van licht die uitgestraald wordt door enkele nanoschaal objecten volledig te bepalen voor elke hoek in het stralingspatroon. We combineren een "Fourier-microscoop", waarbij het achterbrandvlak van een microscoopobjectief met een hoge NA afgebeeld wordt op een camera, met een zogenoemde polarimeter die bestaat uit een kwart-lambda plaatje en een lineair polarisatiefilter. Hiermee kun je de volledige Stokes parameters bepalen voor elke uittreehoek binnen de numerieke apertuur van het objectief. We passen onze techniek toe op fluorescentie gegenereerd door moleculen die ingebed zijn in een nanoschaal opening in een goud film, die omgeven is door concentrische cirkelvormige groeven (een zogenaamde bull's eye antenne), of door een spiraalvormige groef. Met onze techniek kunnen we de partiële graad van polarisatie meten, als ook de mate van lineaire polarisatie, de mate van circulaire polarisatie, en de volledige oriëntatie en excentriciteit van de polarisatie-ellips die het gepolariseerde deel van de straling beschrijft. We vinden dat alle antennes fluorescentie opleveren met een aanzienlijke graad van polarisatie, hoewel de moleculen zelf willekeurig georienteerd zijn en ook fluorescentie van moleculen in een enkel gat dat niet door groeven omgeven is geen enkele graad van polarisatie laat zien. We schrijven dit toe aan het feit dat fluorescentie van de moleculen deels ingevangen

wordt door oppervlakteplasmonen van de goud film, om vervolgens pas in tweede instantie af te stralen door strooiing van de plasmonen aan de groeven. Omdat dit proces coherent is levert afstraling aan de groeven via interferentie een vernauwde bundel aan fluorescentie op. Het p-gepolariseerde karakter van de oppervlakteplasmonen resulteert in een hoge mate van p-polarisatie van de via de groeven afgestraalde fluorescentie, zelfs ondanks de willekeurige dipoolorientatie van de eigenlijke bronnen, dat wil zeggen van de moleculen die plasmonen aanslaan. Tot slot hebben we ook de invloed van de polarisatie van het inkomende pomplicht onderzocht, en bespreken we numerieke simulaties die enkele eigenschappen van de polarisatie als functie van uittreehoek verklaren.

Acknowledgments

During the past four years, I have had the luck to experience a great scientific endeavor. I feel very much indebted and very thankful to my supervisor Femius Koenderink who is not only a great advisor but also an excellent teacher. Femius, I am very grateful to you for what I have learned from you, for the countless amount of support and help from you, and for your dedication, patience and understanding. I can not thank you enough. I would also like to thank all the past and present members of the Resonant Nanophotonics group. It was a great pleasure to work together with you and learn from you. Thank you Ivana, Leon, Christelle, Anouk, Bob, Freddy, Marie Anne, Marko, Per, Hinke, Bart, Hugo, Cocoa, Alessandro, Mengqi, and Floor. I have been very lucky to inherit a nice working setup and many analysis codes upon starting my PhD, for which I would like to specially thank Martin who has been always open and willing to share his knowledge. I enjoyed very much sharing my office with Felipe who was always a boost of energy and motivation during the stressful times for which I am very grateful. I would like to thank Lutz for all the inspiring discussions that we had and for his specific type of humor and fun he brought to the group. Andrej, thank you for being one of the only physicists with whom I could freely talk about music, art and culture for hours without feeling uncomfortable. Clara, you have been one of the kindest and most cheerful members of the group. I am specially grateful to you for our enjoyable collaboration which led to chapter 5 of this thesis.

The integrity and supportive nature of the research groups has made AMOLF the perfect place to do a PhD research. I have been always grateful for working in such interactive, educational, and friendly atmosphere. I would like to thank all the members of Center for Nanophotonics at AMOLF for their friendly support and help and for all the fruitful discussions and suggestions during the poster sessions and the colloquia. Specially, I would like to thank Toon Coenen for our collaboration which resulted in chapter 4 of this thesis. My research would have not been successful without the help of amazing infrastructure departments of AMOLF. I am very grateful to the AMOLF nanoCenter for the great support and maintenance.

When I first decided to step into the research path almost 10 years ago during my BSc. studies, I did not have any clear idea on how one should do it properly. It was Javad Zarbakhsh who generously offered me his knowledge and enlightened the path

for me and helped me step by step; I am beyond grateful to you Javad. I would also like to thank all my friends for their immeasurable support and encouragement during the past years. Specially I am grateful to my Iranian friends in Amsterdam for all the unforgettable moments we spent together. I never felt away from home with you; Thank you Vahid, Sara, Saba, Amin, Fatemeh, Hodjat, Marzieh, Behsa, Naser, Sareh, Shayan, Narges, Samin, Mehdi, Marzieh, Avid, Mahdi, Samira, Nora, Ali, Azadeh, Rojman, Mohammad, Mahsa, Seyed, Rokhsareh and Danial. I will certainly miss you the most when leaving Amsterdam. Alireza, thank you for being such a compassionate and great friend to me. I enjoyed a lot our lunch time chats about science, politics, morality, art, family and many more.

Finally I would like to thank my family who immensely supported me for my whole life. My gratitude towards my parents is beyond words. I feel extremely fortunate to have you and I am proud of you. I would also like to thank my brother and my sister-in-law, Ali and Shirin for their support and encouragement.

List of publications

This thesis is based on the following publications:

- *Suitability of nanodiamond nitrogen-vacancy centers for spontaneous emission control experiments*, A. Mohtashami and A. F. Koenderink, New J. Phys. **15**, 043017 (2013). **(Chapters 2 and 3)**
- *Nanomechanical method to gauge emission quantum yield applied to nitrogen-vacancy centers in nanodiamond*, M. Frimmer, A. Mohtashami, and A. F. Koenderink, Appl. Phys. Lett. **102**, 121105 (2013). **(Chapter 3)**
- *Nanoscale excitation mapping of plasmonic patch antennas*, A. Mohtashami, T. Coenen, A. Antoncecchi, A. Polman, and A. F. Koenderink, ACS Photonics, DOI: 10.1021/ph500225j (2014). **(Chapter 4)**
- *Full polarization mapping of wave-vector resolved fluorescent emission from single nano-antennas*, A. Mohtashami, C. I. Osorio, and A. F. Koenderink, in preparation. **(Chapter 5)**
- *K-space polarimetry on bull's eyes antennas*, C. I. Osorio, A. Mohtashami, and A. F. Koenderink, in preparation. **(Chapter 5)**

Other publications by the author:

- *Advanced impedance matching in photonic crystal waveguides*, A. Mohtashami, J. Zarbakhsh, and K. Hingerl, Opt. Quant. Electron. **39**, 387–394 (2007).
- *Geometrical freedom for constructing variable size photonic bandgap structures*, J. Zarbakhsh, A. Mohtashami, and K. Hingerl, Opt. Quant. Electron. **39**, 395–405 (2007).

- *Method of calculating local dispersion in arbitrary photonic crystal waveguides*, B. Dastmalchi, A. Mohtashami, K. Hingerl, and J. Zarbakhsh, Opt. Lett. **32**, 2915–2917 (2007).

- *Phonon-assisted transitions from quantum dot excitons to cavity photons*, U. Hohenester, A. Laucht, M. Kaniber, N. Hauke, A. Neumann, A. Mohtashami, M. Seliger, M. Bichler, and J. J. Finley, Phys. Rev. B **80** 201311 (2009).

- *Temporal monitoring of nonresonant feeding of semiconductor nanocavity modes by quantum dot multiexciton transitions*, A. Laucht, M. Kaniber, A. Mohtashami, N. Hauke, M. Bichler, and J. J. Finley, Phys. Rev. B **81** 241302 (2010).

- *Local dispersion of guiding modes in photonic crystal waveguide interfaces and hetero-structures*, B. Dastmalchi, R. Kheradmand, A. Hamidipour, A. Mohtashami, K. Hingerl, and J. Zarbakhsh, Prog. Electromagn. Res. B **26** 39–52 (2010).

- *Nonresonant feeding of photonic crystal nanocavity modes by quantum dots*, A. Laucht, N. Hauke, A. Neumann, T. Günthner, F. Hofbauer, A. Mohtashami, K. Müller, G. Böhm, M. Bichler, M. C. Amann, M. Kaniber, and J. J. Finley, J. Appl. Phys. **109** 102404 (2011).

- *Nanoscale lithographic positioning of fluorescing quantum dot nanocrystals on planar samples*, F. T. Rabouw, M. Frimmer, A. Mohtashami, and A. F. Koenderink, Opt. Mater. **35** 1342–1347 (2013).

- *Optimization of quality factor in photonic crystal cavities through finite difference time domain and multipole expansion technique*, A. Mazaheri, A. Hamidipour, R. Jannesary, S. Zamiri, A. Mohtashami, and J. Zarbakhsh, J. Nonlinear Opt. Phys. Mater. **22** 1350040 (2013).